TRANSPORT IN GRAPHENE TUNNEL JUNCTIONS

A Thesis
Presented to
The Academic Faculty

by

Christopher E. Malec

In Partial Fulfillment
of the Requirements for the Degree
Doctor of Philosophy in the
School of Physics

Georgia Institute of Technology
August 2011

TRANSPORT IN GRAPHENE TUNNEL JUNCTIONS

Approved by:

Professor Dragomir Davidovic,
Committee Chair
Department of Physics
Georgia Institute of Technology

Professor Dragomir Davidovic,
Advisor
Department of Physics
Georgia Institute of Technology

Professor Dragomir Davidovic
Department of Physics
Georgia Institute of Technology

Professor Phillip First
Department of Physics
Georgia Institute of Technology

Professor Paul Goldbart
Department of Physics
Georgia Institute of Technology

Professor Zhigang Jiang
Department of Physics
Georgia Institute of Technology

Professor Alan Doolittle
Department of Electrical and
Computer Engineering
Georgia Institute of Technology

Date Approved: 13 June 2011

To my parents James and Linda,

my brother Nick,

and my wife Sara,

who believed in me, and are always there

ACKNOWLEDGEMENTS

I acknowledge my advisor, Prof. Dragomir Davidovic, for advice, support, and an example of just how much work it takes to get things right. I would have reinvented the wheel thousands of times over without his guidance, as it stands, I think I kept the count under twenty. Even if not directly, I have probably been affected by every professor here since they at some point choose the colloquium speakers, write a qualifier problem, or decide what other students I'm going to have to put up with in the coming years, so I thank all of them for taking their tasks seriously. Directly, I found Prof. Kennedy's Quantum and Prof. Zangwill's Electricity & Magnetism courses not only useful to help me pass the qualifier, but truly helpful to me in how to attack problems and explain them to others. Prof. Berger, Conrad, deHeer, First, and Jiang have been very helpful in graphene related advice, and I appreciate Prof. Jiang taking an hour from his day to give me some exfoliation pointers.

Thanks to my fellow students who provided social, academic, and technical support. Thanks to Drs. Felipe Birk, Xiya Liu, and Liyuan Zhang for their help within the lab, and particularly to Dr. Yaguang Wei for setting a good example on my first project. Throughout the rest of the department Britt Torrance and Drs. Joanna Hass, Kevin Kubista, Lee Miller, and Greg Rutter for keeping me abreast of all the ways that STM experiments were beating me to the punch; John Hankinson, Yike Hu, Ming Ruan, and Dr. Mike Sprinkle for helping with the AFM, Raman microscope, Plasma etch, and other helpful pieces of equipment in Prof. deHeer's lab, as well as the wealth of graphene knowledge rapidly accumulating within Georgia Tech; Jeremy Hicks and Farhana Zaman for giving me the engineer's perspective; Dr. Salvador Barraza-Lopez for his generous use of time to show me both the power and limits of

computation to solve my problems, and of course for solving some of my problems; and Daniel Borrero, Danny Caballero, Deborah Ortiz, and Alex Wiener, and Drs. Ed Greco and Seungjoo Nah for keeping coffee hour alive, because 2:30-3:30pm is a terrible time of the day to be awake without a caffeine boost.

I'd like to acknowledge the staff who holds the show together: Kevin Carter, Scott Centers, Keith Garner, Judy Melton, Diego Remolina, and Victoria Speights to name a few. There have been many turnovers since I've started and there will be more in the years to come, but whoever is in the offices, our orders get placed, our bills get paid, our building gets cleaned, the pipes keep cold water flowing, our electronics get fixed, our mail gets delivered, and a million other important things. They also typically don't read this kind of thing, so this is a short reminder to those who do to treat them right, your life would be a lot harder without them.

Finally, my wife deserves some kind of medal for putting up with the unpredictable hours of an experimentalist's life. Our time in Atlanta has been longer than either of us expected, but together we were able to handle the heat.

TABLE OF CONTENTS

LIST OF TABLES

LIST OF FIGURES

SUMMARY

It has been predicted that gold, aluminum, and copper do not fundamentally change the graphene band structure when they are in close proximity to graphene, but merely increase the doping. My data confirms this prediction, as well as explores other consequences of the metal/graphene interface. First, I present a technique to fabricate thin oxide barriers between graphene and aluminum and copper to create tunnel junctions and directly probe graphene in close proximity to a metal. I map the differential conductance of the junctions versus tunnel probe and back gate voltage, and observe mesoscopic fluctuations in the conductance that are directly related to the graphene density of states. I develop a simple theory of tunneling into graphene to extract experimental numbers, such as the doping level of the graphene, and take into account the electrostatic gating of graphene by the tunneling probe. Next, results of measurements in magnetic fields will also be discussed, including evidence for incompressible states in the Quantum Hall regime wherein an electron is forced to tunnel between a localized state and an extended state that is connected to the lead. The physics of this system is similar to that encountered in Single Electron Transistors, and some work in this area will be reviewed. Finally, another possible method of understanding the interface between a metal and graphene through transport is presented. By depositing disconnected gold islands on graphene, I am able to measure resonances in the bias dependent differential resistance, that I connect to interactions between the graphene and gold islands.

CHAPTER I

INTRODUCTION AND BACKGROUND

In this thesis, I will look at the physics of tunneling as a way to infer fundamental properties of solids. Primarily the focus will be on tunneling in relation to the new material graphene. Previously unrecognized complications caused by the graphene system in relation to tunneling are considered. Non-tunneling transport will be introduced, and in all cases, the quantities measured will be made clear by a combination of equilibrium and non-equilibrium physics. In this chapter, I will present some background information on graphene and transport theory that is used in the experimental sections of the thesis.

1.1 Quantum transport in solids

Equilibrium quantum statistical mechanics tells us that the distribution of electrons in the available single particle energy states in a solid will follow a Fermi function [3]

$$f(E_{\mathbf{k}}) = \frac{1}{1 + exp((E_{\mathbf{k}} - \mu)/kT)}, \tag{1}$$

where μ is known as the chemical potential or the Fermi level. This consequence of the Pauli exclusion principle lies at the heart of interpreting a large number of transport experiments. At low temperatures, electrons can scatter out of states that are occupied below the Fermi level and scatter into unoccupied states above the Fermi level. Exceptional changes to the equilibrium form of the Fermi function can cause exceptional changes to the measured transport.

An example that leads to surprising results will come up later in this thesis when a large electric current flows across the sample,

distorting the equilibrium Fermi function. When external fields and temperature gradients are applied, the distribution of electrons may vary in real space, momentum space, and time. The non-equilibrium Fermi function $g(r, k, t)$ is defined at the point $\mathbf{r}$, wave vector $\mathbf{k}$, and time t and when integrated over the phase space contains the same number of electrons as in the equilibrium case so that in equilibrium $g(\mathbf{r}, \mathbf{k}, t) = f(\mathbf{r}, \mathbf{k})$. [4]

There have been many efforts to quantify knowledge of external fields and the microscopic quantities of a solid into knowledge of the conductivity of a solid. The Boltzmann equation is a semiclassical theory that makes use of the non-equilibrium function discussed above and assumes that it does not differ greatly from the equilibrium form. [4] The Landauer formalism has been successful for phase coherent conductors where inelastic scattering is rare and has been applied to many mesoscopic problems. [5] The Kubo formalism relates the statistical fluctuations of electron fluxes in a solid to its conductivity. [6] The fact that there is no single theory for electron transport hints at the complexity of the problem and suggests an embrace of those cases in which simple ideas and theories have application.

Quantum tunneling through a classically forbidden barrier may be a less intuitive mode of electron transport, but it is in at least some ways much simpler than more conventional ohmic transport. Since the two solids are separated by a thin insulator so that transport across the barrier is a relatively rare event, the electrochemical potentials are well defined on each side, and can be assumed to follow an equilibrium distribution function, while the voltage drop occurs across the insulator. Also, since the transport is determined by equilibrium states available on either side of the junction, the energy resolution of such experiments is limited by the thermal energy kT.

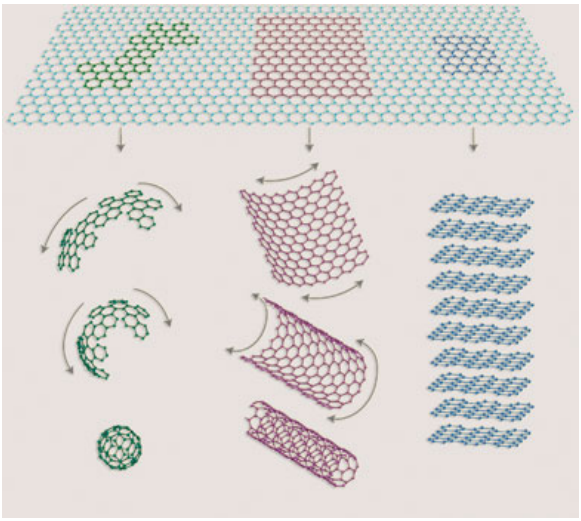

Figure 1.1: Graphene is a honeycomb lattice that can be thought of as a prototypical material for carbon nanostructures. Reprinted by permission from Macmillan Publishers Ltd: Nature Materials Ref. [1] © 2007

1.2 Graphene and its band structure - tight binding model

Since graphene is the material under study in this thesis, it is appropriate to review its basic electrical properties. Graphene is a single hexagonal lattice of carbon atoms as shown in Fig. 1.1 and has recently come into the spotlight due to the successful implementation of field effect transistors (FETs) and observation of the half integer Quantum Hall Effect (QHE). Wallace [7] first calculated the band structure of graphene within the tight binding model as a stepping stone to calculating the band structure of graphite.

The tight binding model assumes that the Bloch wave function is well approximated by a linear combination of atomic wave functions. [4] Since the sp_3 carbon carbon bond is extremely strong, it was suspected that the bands are formed by the $2p_z$ orbitals. So the tight binding approximation takes zero on site energy, and a nearest neighbor interaction with a single band.

In the language of second quantization, these simplifications take on a very compact form, and I will write them down here as they make it very simple to see how to

populate and diagonalize the appropriate matrix in order to simulate the energy levels of disordered samples. The operators c_i and $c_i^\dagger$ represent the creation or anihlation of an electron in a $2p_z$ state at site i, then the Hamiltonian reads [8]

$$H = \sum_i^N \epsilon_i c_i^\dagger c_i + \sum_{i,j}^{n.n.} t_{ij} c_i^\dagger c_j \tag{2}$$

where ϵ_i is the energy to create an electron in a $2p_z$ orbital at site i, and t_{ij} is the coupling energy between nearest neighbor $2p_z$ states. In graphene, $\epsilon_i = \epsilon = 0$ and $t_{ij} = t = -3.033eV$. If atomic scale disorder is introduced, then ϵ_i will take on finite random values to reflect the differences in the number of electrons at different sites, but they must sum to zero since no electrons are added to the system. An impurity potential will also be reflected on the diagonal of the Hamiltonian, but the ϵ_i terms will be correlated to one another according to the positions of the impurities. The effect of a magnetic field can be added by including the Pierel's phase $t_{ij} \rightarrow t_{ij} e^{i\phi_{ij}}$ such that $\phi_{ij} = \frac{e}{\hbar} \int d\mathbf{l} \cdot \mathbf{A}$. [9] Since a magnetic field breaks spatial symmetry, a larger number of unit cells has to be calculated in order to accurately determine the energy levels.

This Hamiltonian produces a linear band structure with centered around the K points of the hexagonal Brillouin zones, so that $E(\kappa) = \hbar v_F \kappa$ where $v_F = 3ta_0/2\hbar$ and a_0 is the carbon-carbon bond distance, [10] and consequently, the density of states is also linear since $g(k)dk = (4/(2\pi)^2)2\pi k dk \rightarrow g(E)dE = 2EdE/(\pi(\hbar v_F)^2)$.

1.3 The semi-classical picture of electron dynamics in graphene

Since the current is merely the velocity of charge carriers times their density and graphene has one band that can contributes to transport at low energies, the current can then be expressed as [4]

$$\mathbf{j} = e g_s g_v \int \frac{d\mathbf{k}}{(2\pi)^2} \mathbf{v}(\mathbf{k}) g(\mathbf{k}). \tag{3}$$

Within the relaxation time approximation the nonequilibrium distribution function $g(\mathbf{k})$ can be expressed as $g^0(\mathbf{k}) - e\mathbf{E}\cdot\mathbf{v}(\mathbf{k})\tau(E(\mathbf{k})\left(-\frac{\partial f}{\partial E}\right)$. At zero temperature, $-\frac{\partial f}{\partial E} = \frac{v_F}{\hbar}\frac{\partial f}{\partial \mathbf{k}}$, and taking advantage of the constant Fermi speed in graphene, the conductivity is [11]

$$\sigma = e^2 g_s g_v \int \frac{d\mathbf{k}}{(2\pi)^2}\tau(E)\frac{v_F^2}{2\hbar}\delta(\mathbf{k}-\mathbf{k_F}) = \frac{e^2 g_s g_v k_F \tau(E_F) v_F^2}{4\pi\hbar} = \frac{e^2 g_s g_v \tau(E_F) E_F}{h 2\hbar}. \quad (4)$$

Thus the main issue of conduction in graphene is actually the determination of the energy dependence of the relaxation time. Since graphene is not a simple metal, it cannot be assumed that the relaxation time is independent of energy. τ is determined from the Boltzmann equation and has been carried out by several groups. [11, 12] The determination is that the relaxation time in impure graphene scales with the square root of the carrier density to give the observed linear dependence in the conductivity. Subtleties in this relationship can reveal aspects of scattering in graphene. [13, 14, 15]

The semi-classical equations of motion in a magnetic field are given by

$$\dot{r} = \mathbf{v} = \tfrac{1}{\hbar}\tfrac{\partial E(\mathbf{k})}{\partial \mathbf{k}}; \quad (5)$$

$$\hbar\dot{\mathbf{k}} = e\mathbf{v}\times\mathbf{B}. \quad (6)$$

So that given the graphene band structure $E(\mathbf{k}) = \hbar v_F\sqrt{(k_x^2+k_y^2)} = \hbar v_F \kappa = E(\kappa)$, it follows that

$$\hbar\dot{\mathbf{k}} = \frac{e v_F}{\kappa}(k_x\hat{\mathbf{x}} + k_y\hat{\mathbf{y}})\times B\hat{\mathbf{z}} = \frac{eB\hbar v_F^2}{E(\kappa)}(k_y\hat{\mathbf{x}} - k_x\hat{\mathbf{y}}). \quad (7)$$

Defining the cyclotron frequency to be $\omega_c = eBv_F^2/E(\kappa)$ (implying the law that $m^* v_F^2 = E(\kappa)$), these equations lead to circular orbits where the components of momentum are described by:

$$\dot{k}_x = \omega_c k_y, \quad (8)$$

$$\dot{k}_y = -\omega_c k_x. \quad (9)$$

The orbital energy of a particle is given by $\frac{1}{2}\mathbf{L}\omega_c = 2n\hbar\omega_c$. Since the orbital angular momentum must be quantized in integer multiples of $4\hbar$, accounting for spin and valley degeneracy, the energies of the Landau levels are

$$2i\hbar\omega_c = E \rightarrow 2i\hbar eB\hbar v_F^2 = E^2 \rightarrow E = \pm v_F\sqrt{2e\hbar B|i|}. \tag{10}$$

This equation should be contrasted to the orbital energy of a parabolic band that is linear with magnetic field and Landau index. Another important feature of the magnetic levels is that there exists a level of zero energy. The semiclassical derivation presented here does not give a clear reason for there to exist a zero energy Landau level while a 2DEG does not have a zero energy level. The zero energy state must therefore be a consequence of the electron phase that is not incorporated in the semi-classical model.

1.4 The quantum mechanics of tunneling

Though first appearing to explain matters of nuclear physics, [16] tunneling has long held an important place in electron transport. Giaever originally used an extremely simple method to generate tunnel barriers between two aluminum electrodes, [17] and received a portion of the Nobel prize for observing the superconducting gap in such structures.

The simplest formulation of tunneling is to investigate the stationary states of a time-independent barrier in the limit where the barrier height is larger than the particle energy. In this case, the stationary wave functions can be solved inside and outside the barrier, then impose boundary conditions at the barrier edges. The full tunneling problem can be dynamic, as the Hamiltonian can be made time dependent to reflect the motion of the electron across the barrier. One case relevant for this thesis is single electron tunneling, where a central island isolated from two bulk electrodes has such a small number of electrons that one electron traveling to or from the island

has a large effect on the system. Single electron tunneling will be dealt with in a different section.

The simplified problem demonstrates several important points. First, the usual geometry used for a physical tunneling device is one-dimensional, and therefore the components of wave vector parallel to the barrier are conserved. Second, energy is conserved when the potential is time independent. Third, the perpendicular wavevector is not conserved, since $k_\perp = \sqrt{2mE}/\hbar$ outside the barrier and $k_\perp = \sqrt{2m(E-U)}/\hbar$ inside the barrier. And finally, the transmission of a wave from one side of the barrier to the other decays exponentially with both the width of the barrier and the potential energy height. [18]

So the electrical current, in an energy conserving system, is the electronic charge multiplied by the probability current through the junction integrated over all possible energy conserving transitions. Currently, this problem is entirely formulated in terms of abstract energy potentials, the success of the technique in the solid state comes from the fact that these potentials can be realized using parameters in real solids. The free electron potentials on either side of the barrier can be created by metals, and the potential energy barrier can be realized as the band gap of a semiconductor or insulator that can be on the order of several eV. The zero potential of the system is then set by the metals' work function.

It is not necessary for both sides of the tunnel junction to be a free electron metal, though if at least one electrode is a metal or a superconductor, the interpretation of tunneling data is greatly simplified, as the distribution function is at least approximately known.

1.5 Calculation of the tunneling current

For this calculation the Fermi surface should be well known and described approximately by the bulk values, and therefore the left electrode is assumed to be a free

electron metal. Normally, a potential V on the left hand electrode is meant to lower the right hand Fermi level by eV, but allowing the Fermi level to float is more convenient in my experiments, so I define the zero of energy as the bottom of the band (the Dirac point in graphene) in the right electrode when there is no bias across the junction.

To calculate the tunneling current across a barrier, I follow the derivation in [18] and assume the motion of a wave packet with group velocity v_x that carries charge from one side of the barrier to another. The probability of transmission for a given energy, D(E), contains the information of the time-independent problem. In the steady state, the current is the sum of contributions of left moving and right moving wave packets.

$$J_{LR} = \frac{2e}{(2\pi)^3} \int d^2k_t dk_x v_x f(\mu_F + eV)(1 - f(\mu_F))D(E). \tag{11}$$

$$J_{RL} = \frac{2e}{(2\pi)^3} \int d^2k_t dk_x v_x f(\mu_F)(1 - f(\mu_F + eV))D(E). \tag{12}$$

$$J = J_{LR} - J_{RL} = \frac{2e}{(2\pi)^3} \int d^2k_t dk_x v_x (f(\mu_F + eV) - f(\mu_F))D(E). \tag{13}$$

The group velocity is represented by v_x, so $\frac{1}{\hbar}\frac{\partial E}{\partial k_x}dk_x = v_x k_x = \frac{1}{\hbar}dE_x$. As stated earlier, tranverse momentum and total energy are conserved separately. Conservation of transverse momentum allows us to write $d^2k_t = 2\pi k_t dk_t = (2\pi)^2 g(E_t)dE_t$, where $g(E_t)$ is a two dimensional density of states, so that now the integral reads

$$J = \frac{e}{\hbar\pi} \int g(E_t)dE_t dE_x (f(\mu_f + eV) - f(\mu_f))D(E)dE. \tag{14}$$

A further simplification can be made in the case of a two dimensional material on the right side of the tunnel barrier. [18] In this case, motion in the x direction is quantized, thus the integral over dE_x becomes a delta function at various band edges E_{nx}. So at zero temperature

$$J = \frac{e}{\hbar\pi} \int_{\mu_F}^{\mu_F + eV} \sum_n g(E - E_{nx})D(E, E_{nx}). \tag{15}$$

In the case of graphene, with its large Fermi velocity at low carrier densities and exceptional thinness, the quantization in the x direction should produce a spacing of several volts. Thus E_{nx} may be neglected from the calculation. In addition the transmission coefficient is set to a constant value. Though this is not necessarily the case in a non-ideal barrier, the assumption should not have a large effect on elastic tunneling. In most experiments, I try to use barriers that are much larger than the voltages applied to the electrodes. Significant variations in the transmission coefficient are often associated with inelastic tunneling events, [19] that is treated separately in the main text. Since the left hand metallic probe has the ability to significantly shift the Fermi level of the graphene through the electric field effect, the Fermi level cannot be assumed a constant function of V when taking the derivative of J, so that

$$\frac{dJ}{dV} = \frac{e^2 D}{\hbar\pi}\left(g(eV+\mu_F)(1+\frac{\partial\mu_F}{\partial eV}) - g(\mu_F)\frac{\partial\mu_F}{\partial eV}\right). \tag{16}$$

This is a formula for the tunneling conductance between a normal metal and a low-carrier density 2D semi-metal such as graphene. Notice that if the carrier density is large, and the Fermi level of the right hand electrode is not shifted by a change in potential on the left hand side, the usual result that the tunnel conductance is proportional to the density of states (DOS) of the system under study at an energy eV below the Fermi level is recovered.

1.6 The electro-chemical potential and the quantum capacitance

Typically in our laboratory, a condensed matter system is at constant volume, low pressure, and low temperature. The electrons in that system, at liquid helium temperatures, are in thermal equilibrium with the lattice. Further, in the case of an electronic device, the system is attached to macroscopic metal leads that place the system in contact with a reservoir of charged particles, such that the system under

study may push out or draw up electrons to or from the leads to minimize its free energy. The usual expression for the Helmholtz free energy at constant volume and temperature: $dF = (\mu + e\phi)dN$. [3]

Since the number of particles in the system are free to vary, μ_{e-ch} is defined as the electro-chemical potential so that [3]

$$dF = (\mu_F + e\phi)dN = \mu_{e-ch}dN. \tag{17}$$

In equilibrium, μ_{e-ch} is the quantity that must be conserved in an electronic device. Since currents are driven by charge carriers that travel from higher to lower energies, the electro-chemical potential is also the quantity that is actually measured by ammeters and voltmeters. In other words, when a voltmeter reads zero, then the two leads are at the same electrochemical potential, and no current flows through an ammeter.

This is all very relevant to the functioning of the Field Effect Transistor (FET) that has played a key role in graphene research. [20] The principle of an FET is to substitute a semiconductor for a metal as one side of a parallel plate capacitor. When a potential is applied to a metallic gate electrode, a charge appears on the semiconducting channel region such that $C(V_g - \phi) = -Q$ where ϕ and Q are the potential and charge of the channel. A change in the amount of charge causes a shift in both ϕ and μ_F that in turn changes the number of states available for transport, allowing the conductivity of the channel to be controlled by the gate.

If the channel is held at ground by the source and drain electrode such that $\mu_F + e\phi = \mu_{e-ch} = 0$, then the shift in the Fermi level is determined by solving the equation

$$C(V_g + \frac{\mu_F}{e}) = -e\int_0^{\mu_F} g(E)dE. \tag{18}$$

In metals, the carrier density is extremely high, for example, Cu has 8.47×10^{22} carriers/cm^3. A 12nm thin film would then have a carrier density per unit area of 1.02×10^{17} carriers/cm^2, and even if Cu were the same thickness as graphene ($\sim$

3.4 Å), 2.88×10^{15} carriers/cm^2. To reach such carrier densities in graphene require extraordinary amounts of chemical doping [21] or electrolytic gates. [22] This means that the Fermi level of a metal cannot easily be shifted by a capacitively coupled gate. Graphene, by contrast, typically has a carrier density less than 10^{13} carriers/cm^2, and the conductivity can be varied by a factor of ten or more.

As semiconductors become two dimensional, another important concept is the quantum capacitance. In Ref. [23] Luryi used a minimization argument applied to an FET geometry to derive a fictional capacitance $C_Q = dQ/d\phi = e^2 g(\mu)$ in series with the geometric capacitance of the gate electrode, that takes the usual form $\epsilon A/d$ that in turn shows that a 2DEG does not perfectly screen an electric field. In a metal, where the density of states is large, C_Q is also large, and since it adds in series, becomes insignificant in calculations. When C_Q is small it can become the dominant capacitance. As an example, graphene at a carrier density of 10^{10}cm^{-2} has a quantum capacitance of 276 nF/cm^{-2} while the commonly used 300nm SiO_2 back gate has a geometric capacitance of about 12 nF/cm^{-2}, for an effective capacitance of $C_{eff} = C_Q C/(C_Q + C) = 11.6$ nF/cm^{-2}. A more technologically relevant 10nm Al_2O_3 top gate [24] would ideally have a geometric capacitance of 787 nF/cm^2, leading to a $C_{eff} = 204$ nF/cm^{-2}.

1.7 Single electron tunneling

In a system where a microscopic conductor is isolated from other electrodes such that only a tunnel resistance or gate capacitance is in communication with a central island the energy to place a single electron on the central island is measurably large, and in this case the phenomenon of Coulomb blockade, or single electron tunneling, becomes important. In this problem, the fact that the electrostatic energy changes by a large amount with the addition of a single electron means a simple equation with a constant Fermi level on the center electrode is not possible. Fortunately, this is a problem that

has been extensively studied over the past two decades, has resulted in an orthodox theory of single electron transport, [25] and was first observed by Zeller and Giaever in arrays of small superconductors sandwiched between oxide layers. [26]

The calculation of current in a Coulomb blockaded system requires two parts. The first part is defining the electrostatics of the problem so that the Fermi levels in the leads and the island may be connected to the bias voltage, the gate voltage, and the discrete energy levels located in the central island. The second part is based on Fermi's Golden Rule

$$\Gamma_{\alpha\to\beta} = \frac{2\pi}{\hbar}\langle\alpha|H'|\beta\rangle^2\rho \tag{19}$$

where $\Gamma_{\alpha\to\beta}$ is the probability per unit time (or *rate*) of a transition from the a single state $\langle\alpha|$ to a set of states $|\beta\rangle$, H' is a perturbation (possibly time dependent) to the system, and ρ is the density of states in $|\beta\rangle$. Through this result of time dependent perturbation theory, a simple method of rate equations can be justified to calculate the steady state current through the system.

This level of analysis is not reached in the data presented here, and it is necessary to extract detailed information from I-V curves where discrete energy levels are present. Therefore, I will focus on the first part of the problem, identifying the potentials of the conductors involved in this system that will be used to gain information about the localized states of graphene at high magnetic fields.

In the following calculations the right lead is grounded so that $\phi_r = 0$. Given voltages on the left and gate electrodes, the charge on the island is $Q = -C_l(\phi_l - \phi) - C_g(\phi_g - \phi) - C_r(\phi_r - \phi) = C_\Sigma\phi - C_lV - C_gV_g = Ne + Q_0$, where N is an integer and Q_0 is a background charge that is a property of the electrostatic environment of the island and is always a fraction of the electron charge. Since the Fermi level in the metallic leads is constant, the electrochemical potential of lead k is $\mu_k = e\phi_k$. If one of the leads is graphene, this particular point may be different. The electrochemical potential of the island is $\mu_{e-ch}(N) = \mu_F(N) + e\phi(N)$, where $\mu_F(N)$

depends on the energy levels of the island. For this calculation, I will assume that there is only one degenerate energy level so that $\mu_F(N) = \mu_F(N-1) = \mu_F(N+1) = 0$, which is realistic in the case of a Landau level.

From this the slopes of Coulomb diamonds, often seen in gated single electron devices, can be calculated. There are four ways that the onset of conduction can occur in the Coulomb blockade regime. The first is that the potential difference between the left (right) lead and the island is large enough that the electrochemical potential is level with the $\mu_F(N+1)$, and then an electron tunnels off of the left (right) lead, and onto the right (left) lead. Alternatively, the initial step could be that the left (right) lead is at a potential low enough that an electron can tunnel off the island, and the island's electrochemical potential can become $\mu_{e-ch}(N-1)$, with an electron tunneling onto the island from the right (left) lead soon afterwards. A graphical summary of this can be seen in Fig. 1.2.

So, for tunneling onto or off of the left lead, the onset of current flow occurs when

$$\mu_l = eV \geq \frac{e}{C_\Sigma}((N+1)e + Q_0 + C_l V + C_g V_g) \quad or \tag{20}$$

$$\mu_l = eV \leq \frac{e}{C_\Sigma}((N-1)e + Q_0 + C_l V + C_g V_g) \tag{21}$$

$$\tag{22}$$

so that both these events represent lines with slope $dV_g/dV = 1 + C_r/C_g$, and spacing $e/(C_r + C_g)$. Likewise, tunneling onto or off of the right hand lead first produces

$$\mu_r = 0 \geq \frac{e}{C_\Sigma}((N+1)e + Q_0 + C_l V + C_g V_g) \quad or \tag{23}$$

$$\mu_r = 0 \leq \frac{e}{C_\Sigma}((N-1)e + Q_0 + C_l V + C_g V_g) \tag{24}$$

$$\tag{25}$$

so that both these events represent lines with slope $dV_g/dV = -C_l/C_g$, and spacing $e/(C_l + C_g)$.

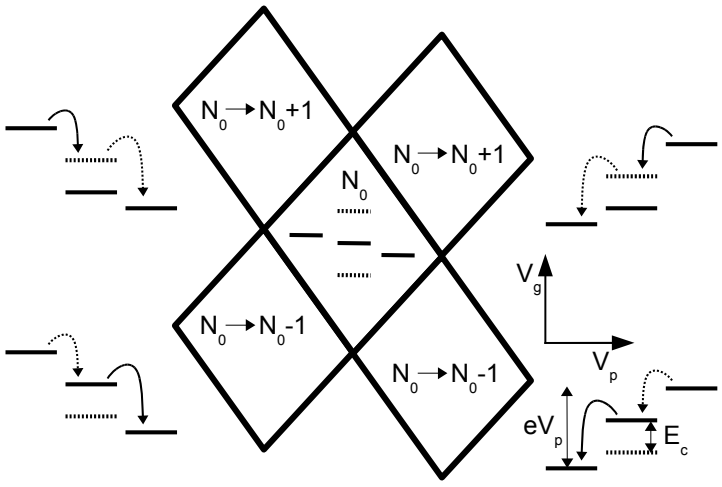

Figure 1.2: A depiction of the four different tunneling events that define the four sides of a Coulomb diamond. The solid lines represent the first tunneling event, while the dotted lines represent the second.

These equations show that the upward sloping sides of the diamond carry information about the capacitance of the right hand lead, and involve the initial tunneling step occurring at the left lead. Meanwhile, the negative sloping sides of the diamond carry information about the capacitance of the left hand lead and involve the initial tunneling event occurring at the right hand lead.

CHAPTER II

EXPERIMENTAL TECHNIQUES

2.1 E-beam lithography

2.1.1 Imaging

The Scanning Electron Microscope (SEM), pictured in Fig. 2.1.1, operates in a very similar way to an optical microscope, except that instead of a sample being illuminated by a diffuse light source and focused to create an image, an electron beam is focused onto the sample, and scanned to create an image. A beam of electrons is focused by magnetic lenses to a point on a surface, and the reflected beam is detected. To image, electrons are boiled off a tungsten (or other metal) filament, then accelerated to 30kV, and sent through two apertures, several lenses, and finally to the sample, where some of the electrons are reflected and detected by a scintillator. As with any microscopy there are certain trade offs in terms of sharpness of image, brightness of image, field of view, and depth of field. A short summary of the relationships between these quantities follows.

- **Accelerating voltage** - This is the voltage that accelerates the electrons from the tungsten filament towards the sample chamber. This gives the electrons their kinetic energy, and hence their wavelength. The imaging possible with an electron microscope is not limited by the deBroglie length of the electrons, so the effect of the accelerating voltage is to increase the number of specularly reflected electrons. Higher accelerating voltage means higher resolution, but at the cost of possible damage to the sample. An average metal will not be damaged by a short exposure to a 30kV beam, so it is usually best to use the highest accelerating voltage possible.

- **Working distance** - The working distance is the same as the focal length. A consequence of an SEM is that the electron optics are easily adjustable so that the working distance and the distance to the sample stage can be adjusted independently. The closer the working distance the higher the resolution, however; depth of field and field of view are compromised. 10mm is a typical working distance for fine lithography, up to 20mm can be used if only larger features are necessary to write.

- **Spot size or beam current** - The amount of current that passes through the sample is known as the beam current and is related to the geometric size of the beam on the sample (spot size). The beam current can be directly measured by focusing the beam into a small aperture located on the sample stage, this Faraday cup captures almost all the electrons and sends the current through ground where it is measured. The higher the spot size the brighter the image will be, and the shorter the time it will take to write patterns; however the image will be progressively blurry as the spot size exceeds the dimensions of the sample.

- **Objective lense aperture** - There are two apertures in the SEM used to collimate the beam. One is static and located near the point of the tungsten filament, and the other is the objective lense aperture that can be moved and swapped. There are three choices for the aperture size, and the larger the aperture, the brighter the image, at the cost of a less collumnar beam, which leads to a less sharp image. Typically, I use the very smallest aperture size.

- **Filment spacer** - There is a small ring that determines how close to the first aperture the filament sits, and there are actually several choices for this ring. A small ring (denoted by a fewer number of marks on the side) will result in a brighter image and a shorter filament life. I have found that spacer IV is a

good compromise, and it is most likely unecessary to make a change to this parameter.

There are also several adjustments that the user can make to improve the image of the microscope, in this there are no real trade-offs, there is merely a procedure to bring about the optimal functioning of the microscope.

- **Filament saturation** - The current that is sent through the tungsten filament to boil off electrons is typically on the order of 50-60 mA. The curve of electron flux generated vs current saturates at a certain current. After this point no appreciable further electron flux is generated, but the extra current will degrade the lifetime of the filament. Thus it is important to adjust the filament current for maximum beam current, but stop when the beam current goes up only linearly with filament current. It should be noted that the filament actually has two maximums, the one at lower current is not a global maximum and will start to again increase rapidly when filament current is increased further.

- **Gun alignment** - The filament must be aimed at the first aperture in order to maximize the illumination of the sample. This is accomplished by adjusting the gun that minutely positions the filament in both x, y, x-tilt, and y-tilt. Maximize the beam current in all four parameters by continually cycling through them. With both this and the last step, it is easier to adjust with a large beam current, such as 1nA. The alignment may optionally be done later at the current that writing will take place, in my experience there will be little change.

- **Focus** - Obviously, without focusing, hours of painstaking work is for naught. There are two ways to focus: by adjusting the plane of the sample to intersect the focal point, or by moving the focal point to intersect the plane of the sample. When the 'fine' focus is used on the SEM, the working distance is adjusted, and since changing the working distance adjusts the magnetic fields that can change

other parameters in the microscope, the best technique is to do course alignment by moving the sample stage.

- **Objective lense wobbler** - In this step, the OL aperture is brought into line with the aperture nearer the filament. The microscope software will focus and defocus the image, if the two apertures are aligned the image will remain stationary. If they are unaligned, the image will move back and forth. Adjust the x and y OL knobs until the image motion is brought to a minimum. If the procedure can be done at ∼40,000x magnification, then the OL alignment should cause no problems.

- **Stigmator correction** - If the electron beam hits the image as an ellipse rather than a circle, this problem is known as astigmatism. The result is an image skewed from its proper shape. Astigmatism can be seen by focusing at ∼100,000x magnification by focusing and unfocusing, watching for features to skew rather than blur. It is easiest to see this in small features that are approximately circular to begin with.

2.1.2 Writing

In many ways writing is actually more difficult than imaging, as the parameters are less forgiving. To write the smallest features possible for a given microscope requires the right resist, thickness, bake time, and careful attention to the entire procedure above. In Electron Beam Lithography (EBL), a beam of electrons is focused onto a polymer resist. The effect of the beam is to break up polymers that have been previously cross-linked by baking. Thus a pattern can be written on the sample, and the exposed region will dissolve in a chemical solvent, known as a developer. Once developed, a metal can be deposited onto the substrate, and the remaining polymer removed with acetone. Baking temperature, time, resist, affect the level

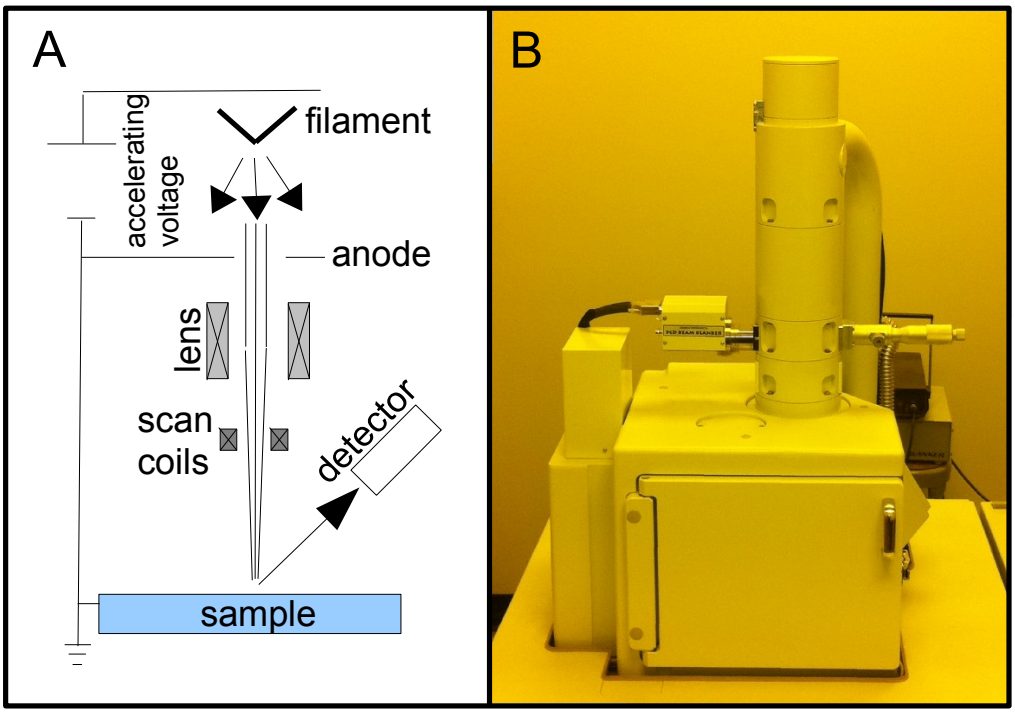

Figure 2.1: A: Schematic of an electron microscope. Electrons are boiled off of a tungsten filament and accelerated through apertures and lenses on their way to illuminate the sample. B: The JEOL 5910 at the Georgia Tech Physics Department. The extra part not featured in the diagram is a beam blanker attached on the left side that allows the beam to be switched off and on during patterning. Many hours have been spent in the comforting yellow glow of this room.

of crosslinking of polymers. Longer times and higher temperatures lead to longer crosslinking, until the polymers are overheated and begin to decompose and ash. A single layer of PMMA resist can work for the lift-off of most metals, but only if it is significantly thicker (∼5x) than the metal being deposited. A bi-layer resist using MMA/PMMA can be used to fix lift-off problems, as the undercut in the resulting resist profiles allows for the excess material to cleanly break from the material on the substrate.

- **Select e-beam resist** - There are several resists available for e-beam lithography. PMMA is very popular, and is usually what is used in our lab. The chemical resolution of most resists falls below the 50nm spot size of the SEM, so this is usually not a concern. Also, the thinner the resist, the higher the possible resolution, but the resist must be thick enough to avoid lift-off problems.

- **Create pattern** - Fortunately, excellent software packages have been written that allow patterns to be easily generated by simple drawing programs. Essentially, each pattern is a grid of dots. The spacing between each dot and the time of exposure is chosen by the user, and the electron beam is turned on and off with a beam blanker to facilitate the precise placement and timing of the dots.

- **Adjust beam blanker** - The beam blanker itself is a metallic plate that can have a large voltage applied to it, deflecting the electron beam momentarily away from the sample. Though usually not necessary, the position and the voltage on the beam blanker can be adjusted for optimal speed of operation.

- **Dose test** - A resist has a critical dose necessary to develop. Finding this critical dose is a necessary step when first making a new pattern. An array of the desired pattern can be made and a variety of doses can be tried. For a given

resist, feature size, and beam current, the dose should typically stay roughly the same.

- **Develop pattern** - Patterns, once exposed can be developed, I usually use a mixture of MIBK and isopropyl alcohol. The dilution and development time affect the extent of etched resist. The longer the pattern is developed, the more resist is etched, until no resist that has received the critical dose remains. Once a development time has been found, I do not change it. It is much easier to adjust the dosing time to the development than adjust both at once. The proper development of most structures can and should be checked with an optical microscope.

- **Metalize and image** - To evaluate new patterns, a high contrast metal (such as gold) can be evaporated onto the developed pattern. The pattern may be accurately imaged without lifting off the metal in acetone, as any problems can be identified at this point without compounding them with lift-off issues.

2.1.3 Alignment

When making a complex device, it is often best to come up with a clever way to fabricate the entirety of the device in a single lithography/evaporation step. Many times this is not possible, notably for exfoliated graphene where the flake must first be exfoliated, and then electronic leads added later. The alignment of subsequent patterns in e-beam lithography is mostly a matter of geometry. One or several alignment markers (preferably made from the high SEM contrast metal gold) are placed nearby the graphene flake to be lithographed. The SEM is then used to image these markers without exposing the flake to the e-beam. By aligning the imaged pattern with the intended pattern, a transformation matrix can be calculated to write a pattern correctly on top of the desired flake. There are several errors possible in this procedure and when designing alignment the goal is not to reach the highest accuracy

possible with each alignment, but to achieve an accuracy that consistently aligns well enough for a particular experiment, as the more complex the alignment, the more time consuming. A list of errors and their remedies follows:

- **Positioning** - This is typically one of the largest errors, and if this and rotation are corrected, most patterns will be fine. Only one alignment mark is required to correct for position, an error that results from the inaccuracy of the microscope stage. The best way to minimize the error of positioning, and thus insure a quick and efficient alignment, is to create large alignment marks that can be easily seen in the lower magnifications of the microscope. Then create several smaller markers that can be found given the location of the large marks. One should also note that the size of the alignment mark must not be significantly larger than the desired accuracy of alignment.

- **Rotation/tilt** - If two markers are independently aligned, a rotation matrix for the pattern may be calculated, and if three are independently aligned then rotation and tilt may be calculated. This process takes time, however, and will eventually cause larger errors with the finest alignments. Tilt is generally not a problem as long as the sample is visibly flat on the stage, there is less than one degree of tilt. Rotation brings into play the fact that there are three axes involved in e-beam lithography: the stage axis; the sample axis; and the beam axis. The stage axis can be aligned to the sample axis by moving along a straight line on the sample, a cleaved edge or a series of markers, and rotating the stage until the image neither falls nor rises on the screen. The beam axis can then be aligned by using the beam rotation to bring the image square with the corners of the computer screen. In this way all stage motions and beam motions will be aligned according to the same axes. It should be noted that large scan rotation angles can cause distortions in the pattern due to the angle being mapped to a

finite number of pixels on screen. As long as scan rotation is kept under a few degrees, the distortion should not cause large errors in patterning.

- **Scaling** - What the SEM displays as 1μm may not actually be exactly 1μm, and a careful calibration using a standard is the only way to make sure that it is. What is typically more effective is to make sure that images are calibrated against the SEM, preferably at the same magnifications that will actually be used in writing. Thus, if one wants to align to a feature at 1000x magnification, the image used to make the alignment patterns should be taken at 1000x magnification in the SEM. With graphene, optical images must often be scaled to create e-beam patterns. In this case, the same image in the SEM and optical microscope can be compared to create a scaling factor between the two.

- **Magnification/beam current shift** - When the magnification or beam current of the microscope is changed, there is an accompanying shift in the beam position, and an offset must be input. This shift is fairly reproducible, but only within $\sim$10%. Thus alignment should only be done at the same magnification as writing, if high accuracy alignment is required for subsequent layers, then a new alignment must be made.

- **Drift** - Diligent effort on the above will always eventually be defeated by beam drift. Over the course of one minute the beam can drift be as much as 100nm, though it is often times not this bad. The way to deal with drift is to align the patten as fast as possible, and make sure that all of the most critical features are written first, within about 10 seconds of beginning writing. So if sub-100nm alignment is required, a self-aligned process would be preferable, or if enough samples can be made, random chance could help align structures on this scale.

2.2 Vacuum deposition

The deposition technique used most in our lab is thermal evaporation. In this technique a metal is brought to its melting point and then evaporated in a high vacuum environment. Many materials require specific handling in order to evaporate them, many of a material's quirks can be summed up by the Clausius-Clapeyron equation:

$$\frac{dP}{dT} = \frac{L}{T\Delta V}. \tag{26}$$

This curve describes the slope of the boundary separating the liquid and gaseous phase on a pressure and temperature curve. L is the latent heat of the material, and ΔV is the change in volume of the phase transition. If the pressure in the evaporation chamber is very low, say $\sim 10^{-7}$torr, then the pressure in the chamber is the same as the vapor pressure of the metal being evaporated. From the Clausius-Clapeyron equation,

$$P - P_0 = exp\left(\frac{L(T - T_0)}{\Delta V}\right). \tag{27}$$

This suggests several procedures. First, since evaporation boats can be raised to 1000°C or more, over-baking the resist can be a concern. Since vapor pressure will rise exponentially with temperature, it is better to evaporate at a higher rate for a short time than a lower rate for a long time. Next nearly all gases have approximately the same volume, where as the density of the liquid can vary quite a bit. Thus dense materials like gold can achieve lower evaporation rates than less dense materials like aluminum. Many metals have similar values for the heat of vaporization.

The choice of evaporation boat can be critical to a successful evaporation. The two main important properties of a boat are chemical reactivity and thermal conductivity. Tungsten boats and wires are popular, but aluminum will react with these, so molybdenum boats coated in alumina must be used. These boats must also be used for ferromagnets. The alumina coating lowers the chemical reactivity, but also

the thermal conductivity, therefore expect to use more power to melt and evaporate the same material. Tungsten may be used for the noble metals. Finally, chromium sublimes rather than melts, so good thermal contact with a boat would be impossible, therefore tungsten rods that have been electroplated with chromium are available from suppliers so that the chromium may be sublimed.

There are some dielectrics that may be directly evaporated, however; our lab usually prefers to grow alumina either thermally or reactively. Alumina is thermally grown by evaporating a thin layer (<10nm), and then introducing pure oxygen into the chamber. In a fairly short amount of time the thin, self-limiting layer of alumina will grow on the deposited metal's surface. Alumina may also be deposited by evaporating aluminum in the presence of a small amount of oxygen. In this case, alumina forms continuously on the target substrate.

It is also desirable to manipulate the sample *in situ*, such as rotating the sample for use with a shadow evaporation technique or heating and cooling a substrate to affect film quality or anneal a sample. Various feedthroughs are available from vendors of high vacuum equipment to transmit rotary motion, linear motion, electrical signals, power, etc. Radiative heat can easily be supplied to the sample through the use of electrical filaments and power feedthroughs. Temperatures of nearly 1000°C can be achieved this way, though much more than 450°C is not recommended if kapton is used for an insulating material.

The effect of substrate temperature can have a great impact on evaporated films. The general trend is that lower temperatures lead to more homogeneous films with smaller crystal sizes, and higher temperatures lead to films with very large crystal sizes.

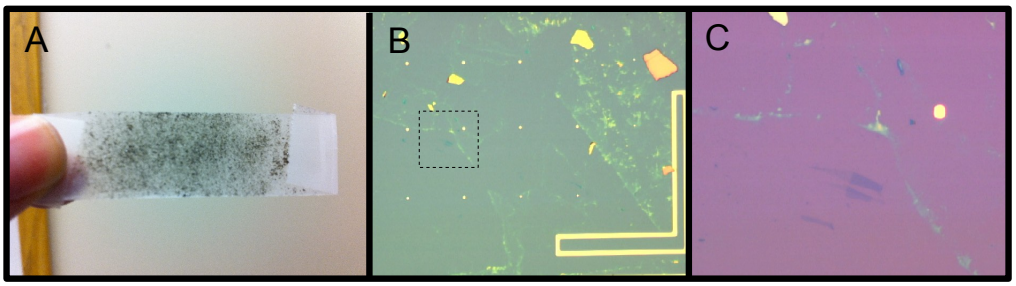

Figure 2.2: A: A piece of scotch tape with graphite flakes, that has served its purpose. B: A wide view of the exfoliated graphite flakes on an alignment grid. C: A close-up view of a small piece of graphene along with several thicker pieces.

2.3 Peeling graphene

The process of peeling graphene is fairly simple and can be done with only a brief amount of training. This explains in part why graphene has become so popular in the last few years, high mobility 2DEG samples can be obtained without the incredible effort necessary to obtain GaAs/AlGaAs samples.

I prefer to write alignment patterns before exfoliating graphene, both to reduce the number of steps, and to make the search for graphene easier. Cr/Au alignment grids are written on ∼3.5 cm square pieces of highly doped Si, with a 300nm layer of SiO_2. The Si chips are cleaned for 30 minutes in a UV cleaner less than 1mm from the lamp, then graphite covered scotch tape is applied. The preparation of the scotch tape is important, but it is difficult to define exactly. There must be sufficient graphite coverage on the tape to produce a fair chance of exfoliating a piece of graphene, but the graphite must be thinned so that what sticks to the chip is close to single layer. A good test is to hold the tape sideways and see if the thickness of the graphite can be seen with the eye. If there is a large amount of flakes sticking up, keep thinning; if it is close to flat, start exfoliating. The same piece of tape should be used to produce possible samples until they stop working, as evidenced by a drastically smaller number of flakes sticking.

Fig. 2.2-A shows a finished piece of scotch tape, ready for exfoliation. The tape should be placed on the SiO_2 and the air bubbles forced out. A gentle hand should be used to rub the tape in all directions for about 10 minutes. I prefer to hold the far end of a cotton swab so as to diminish the force that actually reaches the tape. The tape should be removed as slowly as possible, I have had reasonable success with removing tape from a 1cm chip over the course of 1 minute.

Graphene is searched for using the optical microscope and making use of the alignment grid to keep track of position. Graphene is just barely visible in the optical image, and once several pieces have been identified, most peelers can differentiate between single layer and bilayer by sight. Naturally, the scientific community doesn't accept "it looks rather transparent" as an acceptable identification of single layer graphene. Therefore Raman microscopy is used to confirm samples. [27] Optical techniques [28], and observation of the half integer QHE are also used to identify single layer graphene, but the Raman signature is a fast, simple, reliable test that can be performed before laborious device manufacture.

2.4 Cryogenic measurement

Cryogenic measurement has been a major force in condensed matter physics ever since Onnes liquified helium. It is now known that the average material at room temperature is simply bubbling with excitations: phonons, magnons, plasmons, etc. In order to quiet the thermal activation of these excitations, so that they may be studied and understood, requires lowering the temperature considerably. Room temperature corresponds to a energy of 26meV, 4.3K to 370μeV, 1K to 87μeV and 10mK to 87neV. What matters is not the number of degrees between two temperatures, but their ratio. Liquid helium is nearly a factor of 100 colder than room temperature, while 10mK is nearly a factor of 400 colder than liquid helium. The distance between 4K and 1K is like room temperature and liquid nitrogen. I try to remember these

things when I'm working so hard to get a couple degrees colder, it's worth it.

2.4.1 Techniques to 1K

Cooling samples to 4K leaves the experimenter with options. In any case a dipstick between 1 and 2 meters long is usually made from a stainless steel tube. Wires are strung inside this tube to carry electrical signals. The materials used should typically be stainless steel for structural pieces and phosphor bronze for electrical lines. These materials have low thermal conductivity, preventing heat losses from the dewar. The next decision is if the sample should be in intimate contact with the liquid helium or if the sample should be in vacuum. If temperature studies are to be done, a vacuum is a better choice as the thermal link between the sample and bath can be controlled by allowing a dilute concentration of exchange gas into the chamber. If no temperature control is to be done, then straight into the liquid provides the best heat sinking for the sample, and is generally the simplest thing to do. For 4K experiments with only small magnetic fields, the dipstick may be lowered directly into the storage dewar.

To perform a 1K experiment, it is necessary to thermally isolate the sample from the bath. Therefore, the sample must be placed in vacuum. Typically a needle valve is used to allow a small amount of liquid from the bath into the sample space. A vacuum pump is then used to speed the evaporation of the helium and lower the temperature. By adjusting the needle valve, the inflowing liquid helium will balance that lost by evaporation and a continuous cycle can be maintained. At about 1K, liquid helium becomes a superfluid, its vapor pressure drops to zero, and no more evaporative cooling can take place. At this point other techniques must be used to lower the temperature further.

2.4.2 10 mK: The dilution refrigerator

The operating principle of the dilution refrigerator hinges on an insolubility of ^{3}He in ^{4}He at low temperatures. Essentially, since ^{4}He is a boson and ^{3}He is a fermion,

the system can lower its energy by putting more ^{4}He into the lowest energy orbitals despite the decrease in entropy that a phase separation causes. The stability of a given ^{3}He/^{4}He ratio with temperature is given by a lambda curve. At zero temperature a solution of about 6% ^{3}He is the most that the system can support.

Once a phase boundary is created between a 'dilute' ^{3}He phase that sits on the bottom of the mixing chamber, and a 'condensed' ^{3}He phase that floats on top the still uses a small amount of heat to raise the temperature of some of the liquid drawn up from the mixing chamber to .7K and preferentially evaporate ^{3}He. ^{3}He migrates across the phase boundary, a process that costs energy and thus draws heat away from the system. The heat for this process comes from the sample that the experimenter has heat sunk to the center of the mixing chamber. An illustration of these parts appear in Fig. 2.3.

In this way temperatures of 10mK can be achieved. The ultimate limit of the dilution refrigerator is the necessity for the still heater to keep a constant circulation of mixture. The temperature of the still must remain the same, even as the mixing chamber temperature becomes lower, thus the cooling power decreases with decreasing temperature. Colder temperatures can be achieved for a short amount of time by single shotting the fridge. In this procedure the circulation loop is shut off, and ^{3}He is not returned to the mixing chamber after it evaporates. The time period of the lower temperature is usually less than an hour, and so this is usually used to figure out how much ^{3}He is in the mixture, so that more may be added if a small amount is lost. ^{3}He is a very rare isotope, created mostly in nuclear reactors, and sometimes cannot be had for love or money; so it should be conserved as much as possible.

Below is a procedural outline of running the fridge. The manual is rather opaque if you do not already know how to run the fridge. This is intended to give the novice a conceptual understanding, so that the arcane rituals contained in Oxford's documents will have proper context.

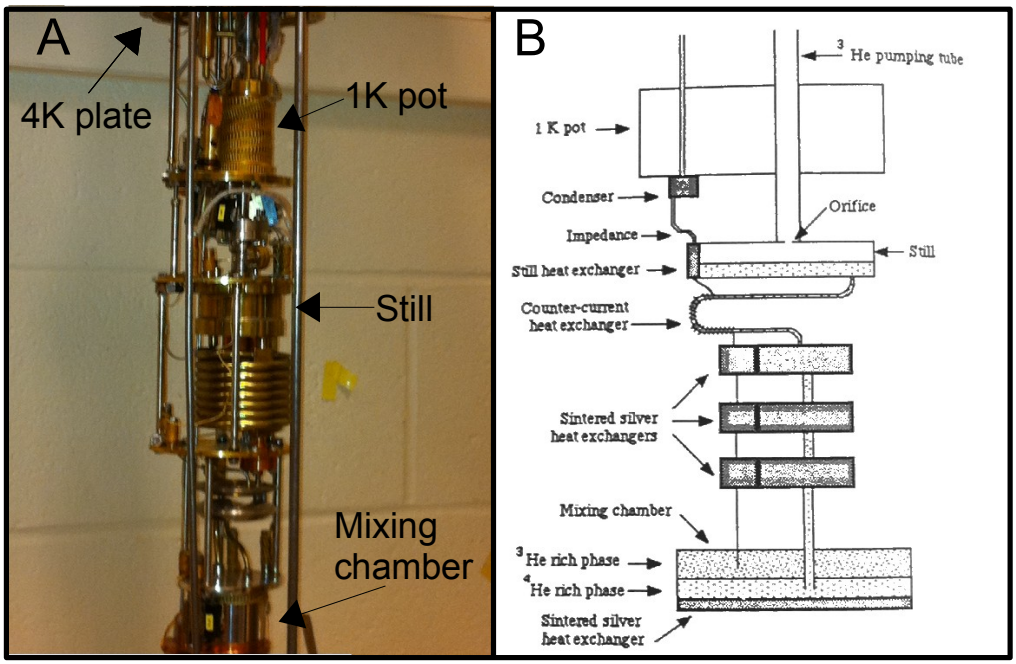

Figure 2.3: A: The dilution refrigerator in S102, the top of the image includes the 4K plate and the 1K pot, and the mixing chamber that reaches 10mK is at the bottom. B: A schematic of a dilution refrigerator, taken from Ref. [2]

- **Prepare insert** - All vacuum spaces should be pumped out and leak tested. This includes the 1K pot, the still and condenser lines, and the inner vacuum chamber (IVC). The 1K pot is non-critical, and can sustain very small leaks without damage to operation. The still and condenser lines are critical since mixture moves through them. No leaks can be tolerated as this is a way to lose precious mixture. The lines should be pumped out at the same time using a vacuum tee, as the ports are connected by a very thin flow impedance that will limit the pumping speed.

  Before pumping out the IVC, put the radiation shield around the mixing chamber and still. Cover all exposed regions with aluminum tape. Bake out the sorb pump (strip of activated charcoal and copper mesh) with a heat gun for about a minute, this will insure efficient operation of the sorb when it is required while cooling to 4K. At this point an indium seal is made to enclose the IVC, this is an ultra-high vacuum seal and should be done correctly. Put a very thin layer of vacuum grease on a strip of indium. Cut the indium to so that it makes a tight circle around the step edge and doubly overlaps by about the length between screw holes. Once the bolts are finger tight, tighten pairs of bolts that lie across from each other, like a drum head, making several rotations around the bolt circle. Pump out and leak test. Again, there should be no leaks for proper operation.

  Now add 5cm^3 of exchange gas. There is a quick way and a right way to do this, and one should probably do it the right way. There should be a valve and a tee on top of the inlet valve to the IVC. There is a brass dead space to insert between the IVC inlet valve and the valve that is attached to it. One end of the tee is attached to a turbo-pump, the other end is attached to a hose leading to the helium canister. with the first valve open, allow the helium to flow until it reaches 1 or 2 psi. Then close the outlet valve of the canister and turn on

the pump. Once the assembly is at vacuum turn on the helium canister flow for a couple seconds to flush the line. Wait until the pump recovers, and do this once or twice more. Now close the pump, and fill the assembly to 1 or 2 psi again. Close the first valve, and open the valve to the IVC. $5cm^3$ of helium have now been inserted into the IVC, and this will be efficiently pumped by the sorb when the chamber reaches 4K.

- **Precool cryostat to 77K** - The outer vacuum chamber (OVC) does not always need to be pumped out, however; at high temperatures the walls of the cryostat are somewhat permeable to helium gas. If the cryostat has been cooled down and warmed up several times, and a leak detector shows an unacceptable level of helium in the OVC, it should be pumped out overnight. Once the OVC is insured to be under vacuum, seal the cryostat and use the auxilliary pump (^{4}He pump) to pump out the cryostat through the main bath port. When the cryostat is under vacuum, flush the main bath space with helium gas from a canister until the bath is at atmospheric pressure. Pump and flush once more. Turn on the liquid nitrogen flow and wait for the air to be blown out of the tube, the initial sound will be periodic, and when the stream becomes continuous, then nitrogen is flowing through the tube and the transfer stick may be placed in the cryostat. Continue transferring nitrogen until the cryostat is full; then remove the stick and allow the system to sit overnight.

- **Blow out nitrogen** - Though the use of liquid nitrogen saves a lot of helium in later cooling, it would solidify if it were allowed to remain in the cryostat. The cryostat is sealed and pressure applied with ultra pure helium gas to push the nitrogen back into a vented nitrogen dewar. This process can take two hours. When the cryostat can be quickly and efficiently pumped to less than 20mBar, then the blow out is complete. The transfer line will typically unfreeze long

after sufficient liquid is gone, and a lot of helium gas can be wasted waiting for this to happen. It is also critically important to lodge the transfer line very firmly into the transfer cone, otherwise the nitrogen in the very bottom of the cryostat will not be able to come back out.

- **Cool cryostat to 4K** - After the nitrogen is gone, the cryostat is pumped and flushed as before with ultra pure helium gas. Now liquid helium is transferred. The rate of helium transfer is very important in terms of efficiently using helium, and I find that 2 or 3 psi of pressure is a good rate until liquid starts collecting in the bottom of the cryostat, and then something closer to 5 psi may be used. Fill it up, each transfer loses helium, so doing fewer transfers is better, even though the helium boil off rate is slightly faster when it is full compared to when it is half full. The temperature controller should be turned on so that the sorb does not cool below 25K (and absorb all the exchange gas) until after the mixing chamber reaches 4.23K. Since there is a lot of fridge and not a lot of exchange gas, this cooling can take a little while. Once the mixing chamber is cool, turn off the temperature controller and thermally isolate the fridge from the bath. The sorb should be allowed to pump for at least 20 minutes. If there is reason for concern that this did not proceed properly a leak detector can be used to check.

- **Run 1K pot** - The 1K pot can now be run. The auxilliary pump is run and connected to the 1K pot. The needle valve is slowly opened to allow a small amount of liquid helium into the pot. Once everything is working correctly, open the needle valve a full turn, and allow the pressure to rise to 100mBar, then close the pot almost, but not quite shut. This will rapidly pass over the initial hump of cooling the fridge to 1K. Once everything is cold, adjust the needle valve to attain about 4-8 psi pressure. The higher the vapor pressure

of the 1K pot, the more cooling power it has, but the higher the achievable temperature. This is related to the vapor pressure of a superfluid as it cools, when the vapor pressure goes to zero, the lowest possible temperature has been reached, and no more cooling is possible by evaporating liquid helium.

- **Condense mixture** - Now is the time for the mixture to come into play. It is critical that no impurities are in the mixture when it enters the dilution refrigerator, and therefore there is both a 77K and 4K cold trap. The cold traps cryopump impurities from the mixture. Opening up both the still and condenser line, the mixture should be slowly allowed into the dilution unit. The mixture should not be allowed in too fast, because the 1K pot is rather small, and can only provide so much cooling power. The still is much wider than the condenser line to allow for fast pumping, and so most of the mixture will condense into the still.

- **Circulate mixture** - At this point the still and condenser lines should be connected in series rather than parallel. The mixing chamber should be at about 1K, as the mixture is cooled by the 1K pot. Beginning the circulation must be done slowly. As the ^{3}He is evaporated from the chamber, it is cooled to .6K. At this point the phase seperation takes place and the mixing chamber runs down to 10mK. By adjusting the still heater, one can increase the cooling power by increasing the rate of circulation.

2.4.3 Electronic filtering and electron temperature

Below about 1K, the electrons in a metal become decoupled from the lattice. This has the somewhat frustrating effect that the electrons no longer have to have the same temperature as the solid that they inhabit, and they will be in general hotter than the temperature reading from the bolometers. The electronic temperature in general is a harder quantity to measure, but the best way is to use something like a single

electron transistor, where transitions are limited to a width of kT.

The goal of filtering is to provide electrons with a mechanism to dump their energy into the lattice. Most methods revolve around theories of a transmission line and trying to make a bad one. That way the electrons lose a lot of high frequency energy and thus lower their temperature. The classic transmission line has a series resistance R and inductance L per unit length, and a parallel conductance G and capacitance C per unit length. Most filtering schemes have a large G, C, L, or possibly all three. Obviously, the type of measurement is important, as in some instances filtering high frequencies would be undesirable. Furthermore, it is not sufficient to merely create an RLC filter and cool it to millikelvin temperatures in order to cool electrons, it is necessary to provide a method to dump this energy to the phonon bath.

Though there are many filter designs available I designed and built a copper powder filter similar to the one built in Ref. [29], as it is a stable, robust design that allows for a large number of electronic leads. The principle is to embed thin wires into a matrix of copper powder and epoxy. The copper powder acts as a large parallel capacitance to the wires, and the epoxy acts as a large parallel conductance at high frequencies. High frequency electrons in the wire emit radiation that is damped by the skin effect in the copper powder. The heat is transferred through the epoxy to the mixing chamber. Since the wire is densely packed in powder, the odds of radiation coming back to the wire are low. The most likely path is out of the filter to the mixing chamber.

Critical to manufacturing a good filter is to vacuum pack as much copper powder as possible into the epoxy. There should be as many copper grains as possible around each wire, and each one should have a good thermal sink to ground. To this end, I mixed a series of copper powder/epoxy concentrations, and pumped excess air with a vacuum pump. I used the mixture with the most copper powder that did not become powdery or brittle upon de-airing.

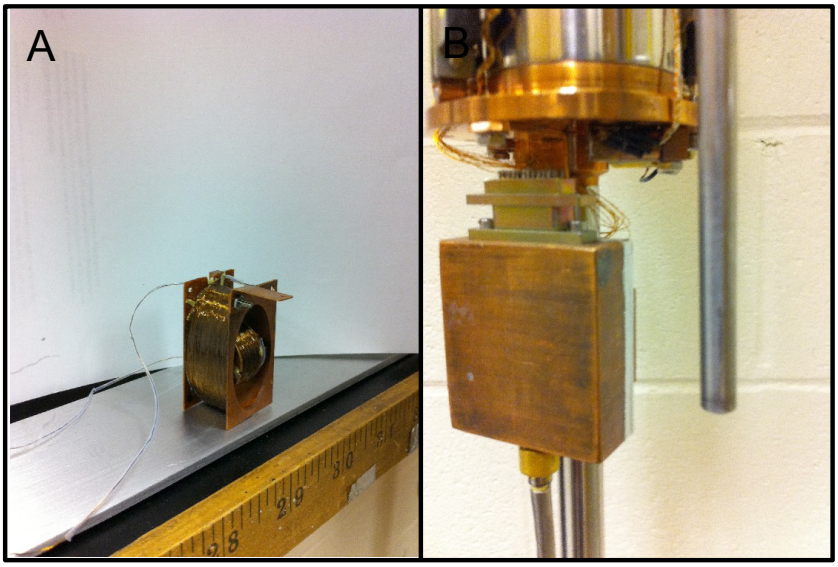

Figure 2.4: A: Two perpendicular magnets designed to fit inside the third magnet located in the cryostat. B: A Cu powder filter that is used to lower the electronic temperature.

2.4.4 Superconducting magnets

A great advantage of working at cryogenic temperatures, and sometimes a necessity, is the use of superconducting magnets. By using superconductors, a magnetic field can be created with very little heating to the bath. The major sources of heating are induction, and the magnet leads. No matter how well made, a superconducting magnet will have a very large inductance, so that the faster the magnet sweeps the more heat is wasted. Also, the non-superconducting leads that feed current to the magnet must be made of highly conductive material that by the Wiedeman-Franz law is also highly thermally conductive. Many magnets have a persistence switch that may be turned on or off to engage or disengage the Cu magnet leads.

A persistence switch is a small length of superconducting wire that connects two ends of the magnet, with a heater attached to the switch. If the heater is off, the switch is superconducting, and no current flows through the leads. In this state,

the magnet can maintain a steady field indefinitely with no additional power. If the heater is on the switch is normal, and current from the leads will flow through the magnet because it has a much lower resistance than the heater switch.

Magnets that generate large fields can be made by simple solenoids, though for nearly 5-20T magnets, the manufacture should be left to the professionals. Extremely large forces can develop on the windings of magnets since the current moves perpendicular to the field, and special power supplies are required to handle low resistance, high inductance loads that are prone to oscillations. Also, large magnets can quench catastrophically as one section transitions from the superconducting to the normal state, the transition cascades through the whole magnet and all the stored energy is released into the helium bath.

Smaller magnets for storage dewars or specialty applications can be made by wrapping and encapsulating wire, and can be done by hand. The encapsulation of wire with epoxy gives the magnet strength by taking on the stresses caused by thermal contraction/expansion and magnetic forces. Stycast 1266 is specifically formulated to have a low viscosity so that it can penetrate magnet windings. When deaired in vacuum, and cured with low heat under constant rotation, it can significantly improve magnet longevity.

2.5 Electronics & measurement

The simplest possible measurement is to apply a voltage on a sample, and measure the resulting current. However, this includes a large number of extraneous wires into the measurement, as the voltage is applied through the wires leading to a contact, through the contact, the sample, through a second contact, and out through the ammeter. In many microscopic tunneling measurements, this is not a problem, as the junction resistance will be significantly larger than all other resistances in the circuit.

Many times, however; this is not the case and the large input impedance of a

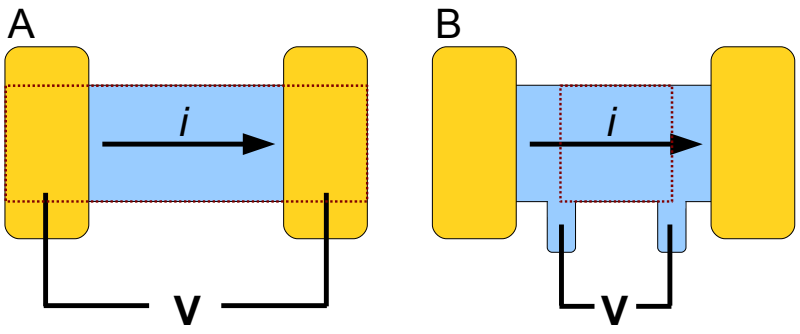

Figure 2.5: Two methods of measuring the bulk resistance of a conductor are shown here. A: The two probe measurement of a device includes both the conductor and contact resistance. B: A four probe measurement that measures the resistance of the conductor.

voltage amplifier is used to cope. By sourcing a current through part of a conductor, the voltage can be probed without forming a new current path using a high impedance amplifier. When measuring the resistance of a conductive channel, either two or four probe resistance is used as shown in Fig. 2.5. The three probe resistance is typically used only if a four probe resistance is desired, and one of the probes is broken. The four probe resistance measures channel resistance without the resistance of the contacts included. If the contact resistance is not troubling to the measurement; the two probe resistance can be much easier to use, and is sometimes preferred, especially in tunneling experiments where the contact resistance is essentially the quantity being measured. When specifically measuring contact resistances there are several choices as shown in Fig. 2.6. The two probe is the simplest, but includes a certain amount of bulk resistance in the measurement. High resistance tunnel junctions can be measured with a two probe measurement, as almost all the voltage will drop across the contact.

The three probe resistance measures the contact resistance plus the lead resistance. If the leads are highly conductive compared to the junction, but the bulk conduction

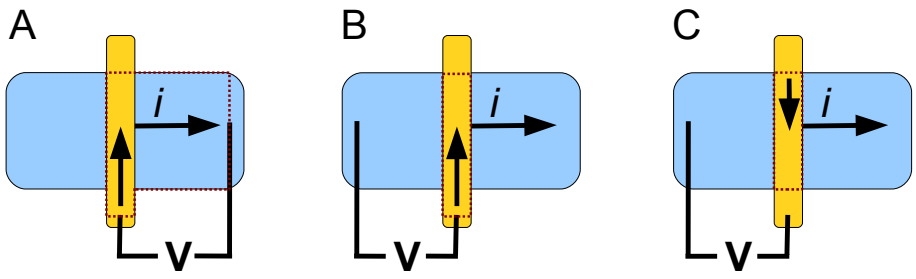

Figure 2.6: Three different methods of measuring the contact resistance are shown here. A: The two probe resistance includes the lead, contact, and conductor resistance. B: The three probe resistance includes the contact resistance and the lead. C: The four probe contact resistance measures the contact resistance.

is similar to the junction resistance, then the three probe configuration is the way to go.

A four probe configuration is also possible for a junction. This geometry technically measures only the junction resistance, however even this can be foiled by an uneven current distribution over the area of the junction. Giaver recognized this issue long ago when dealing with his large area, low resistance tunnel junctions, and found that making at least one lead a superconductor was a very effective way to make sure the lead was an equipotential.

All these measurements either involve sourcing a known current and measuring the voltage or sourcing a known voltage and measuring the current. Sometimes accomplishing this can be rather difficult, but generally rapid changes in both current and voltage at the same time is not recommended as this leads to more complicated data processing later. For example, a bias should be applied in steps smaller than kT so that no features are missed due to averaging. Our lab uses two circuits to accomplish these things.

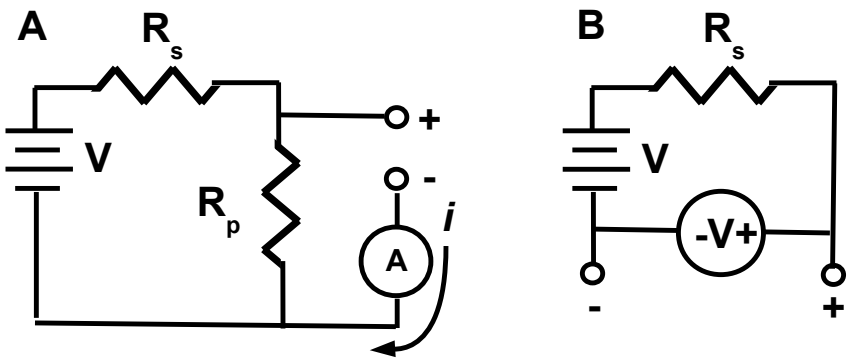

Figure 2.7: A: A measurement circuit for sourcing a constant voltage by placing a small resistance in parallel with the sample. B: A measurement circuit for sourcing a constant current by placing a large resistance in series with the sample.

Fig. 2.7-A shows a constant voltage circuit with a resistor R_p that is much smaller than the sample resistance is put in parallel with the sample. The sample thus sees a voltage $VR_p/(R_p + R_s)$, and then the current through the sample is measured. The true resistance from this circuit is $VR_p/i(R_p + R_s) - R_p$. Fig. 2.7-B shows a constant current supply. A resistance R_s that is much larger than the sample resistance is placed in series, and the voltage V_m across the sample is measured. The true resistance for this circuit is $R_sV_m/(V - V_m)$.

CHAPTER III

GRAPHENE TUNNEL JUNCTIONS

3.1 Introduction

In this chapter I will explain the manufacture and measurement of tunnel junctions between a free-electron metal and graphene. The importance of this measurement relates to the study of metal contacts to graphene. In traditional silicon based electronics, the contacts between semiconductors and other materials play a crucial role. In graphene, however; a prototypical device would be carved out from a single graphene sheet, including the interconnects. [1] This is perhaps the reason that the study of contacts between graphene and metals has not received as much attention as the intrinsic effects. Both for reasons of protection, and the layering necessary to create electronic architectures sufficiently complex for modern integrated circuits, graphene must have other materials stacked on top and possibly beneath it. Thus the study of heterostructures formed between graphene, and oxides, metals, semiconductors, or even other pieces of graphene is of great technological importance, yet there have been relatively few theoretical [30, 31, 32] and experimental [33, 34, 35] investigations of such contacts.

In particular, I study Al and Cu junctions separated from graphene by a sufficiently thin oxide to constitute a tunneling junction, and in many devices sufficiently thick to operate as a field effect transistor. These metals are chosen largely because junctions can be formed relatively easily, however the fact that they are theoretically calculated to not hybridize with the graphene band structure makes them doubly attractive materials. Until now, most low temperature tunneling studies of graphene have been done using scanning tunneling microscopy (STM). [36, 37, 38]

Those studies provided a wealth of information regarding the electronic states in graphene, [39, 40, 41] the Landau levels in a magnetic field, [40, 41, 42] and inelastic tunnel processes. [43] The few implementations of solid state junctions so far have almost exclusively focused on spin-injection studies. [44, 45]

3.2 Fabrication and experiment

I fabricated junctions by visually selecting samples of graphene exfoliated onto an oxidized silicon wafer that is used as a back gate, and confirmed that they were a single graphene layer using raman spectroscopy. [27] Electron-beam lithography was used to define a device pattern in a bilayer of PMMA/MMA resist, then thermally evaporate 35nm of metal, and lift-off in acetone. An image of a finished device is pictured in Fig. **??**-A & B. The large area ($>5\mu m^2$) leads have contact resistances to graphene of order kΩ; they will be referred to as the ohmic leads. In Al, the leads $\sim.5\mu$m wide or less rapidly increase their contact resistance to graphene after removal from the vacuum chamber. In Cu, leads are made narrower (100-200nm), and placed in dilute HNO_3 (12% in water) for several seconds to initiate the oxidation. The devices are rinsed in DI water, IPA, and blown dry. At this point they begin to age in air, though more slowly than the Al junctions. The resistance of the junction reaches the $M\Omega$-range after aging for several days.

The discovery of this simple fabrication method came about from the attempt to create clean tunnel junctions. Many early attempts at contacts were completely insulating, while some were very low resistance, even when extremely thin layers of oxide were evaporated. In the process of attempting to determine the mechanism that causes some evaporated contacts to be highly resistive, and others were ohmic, I came upon the sample identified as Al-2, where two contacts were less resistive, and one was slightly higher. After approximately 15 minutes, the slightly higher resistance contact was observed to significantly increase in resistance, and after an hour, the resistance

was over $100k\Omega s$. Putting the sample in a low humidity environment appeared to do nothing to stop the climb in resistance, but low temperature did in fact arrest the aging. As a result of the delay between the manufacture of Al-2 and wiring the device for measurement at low temperature, this is one of the higher resistance devices reported here.

I also found that it is essential not to heat the Cu samples above room temperature, during the aging or before measurement (heating can promote rapid oxidation in air, and vacuum heating above $\sim$100° C will reduce the Cu-oxide). The sample used in a magnetic field study featured in chapter 4 was heated in vacuum, and restored to full conductivity ($k\Omega s$) even though the leads had oxidized in air to become fully insulating. Since the melting point of Cu is a bit over 1000° C, I believe that the reduction of the oxide to be much more likely than significant movement in the metal.

I suppose that due to these metals' poor bonding with graphene, [30] diffusion of oxidizing agents through the interface is responsible for the oxidation of the junction. This method has been used for fabricating tunnel junctions in the past. In his original tunneling experiments, Giaever [17] oxidized Al in normal air to create tunnel junctions of $\sim$50Å thickness, and the procedure worked even when a semiconducting film was deposited on top of the metal electrode before removal from the vacuum chamber. [46] It should be noted that a similar method was used to study screening in multilayer graphene devices, [47] and that similar reasoning was applied to the poorly bonding metal gold to make tunnel junctions to nanotubes, though in that study a large number of samples had to be made to find a poorly bonding contact. [48]

After allowing the junction to age in air to a high resistance, I cooled the device to 77K to arrest the aging process. At low temperatures, the devices can sit for many days without noticeable change to their resistance, whereas at room temperature they may increase several orders of magnitude within several hours. The junction resistance changes by about 10% upon cooling room room temperature to 77K, and

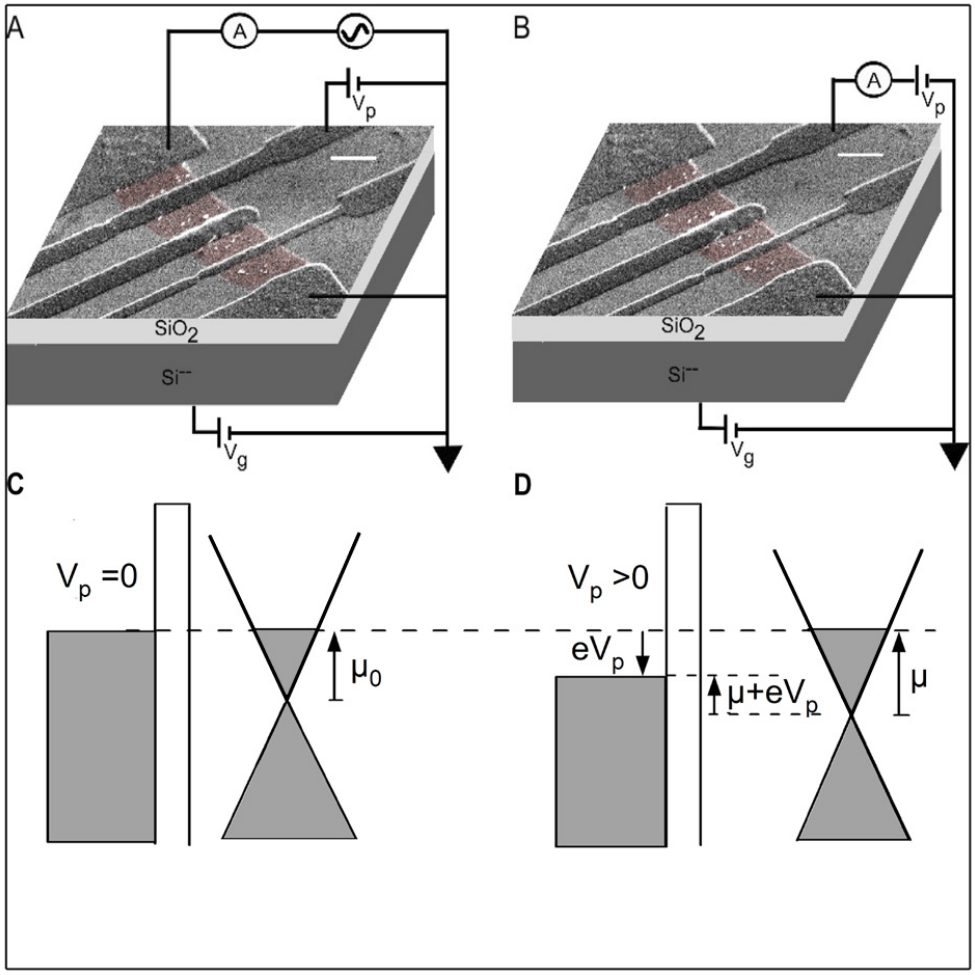

Figure 3.1: Colorized SEM image of device S1 (after measurement) with schematic of A: An FET experiment and B: A tunneling experiment. For low resistance samples, a three-probe measurement was used to remove the effect of the contact resistance of the grounding electrode. Scale bar is 1μm. C: Schematic of Fermi levels at zero, and D: Non-zero probe voltage.

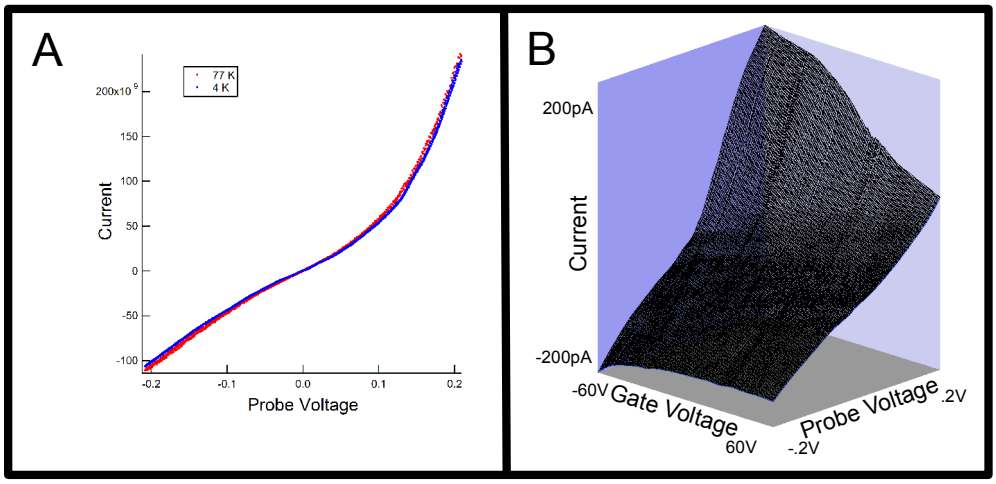

Figure 3.2: A: The IV curve for sample S1-B at 77K and 4K showing a very weak dependence of resistance on temperature. B: Current vs probe and gate voltage at 4K for the same sample. A numerical derivative with respect to the probe voltage is used to calculate conductance.

by less than an order of magnitude upon cooling to 4.2K. All transport measurements in this chapter are performed at 4.2K. I-V curves are shown in Fig. 3.2-A for both 77K and 4K. The lack of significant temperature dependence implies a tall potential barrier to electron tunneling.

I performed two complementary graphene studies. First, I use the probe as a local gate in sufficiently high resistance junctions. The experimental setup is shown in Fig. 3.1-A. By measuring the change in resistance between the two ohmic leads, I obtain the average doping in graphene under the probe.

In the second experimental setup, the current between the probe and the graphene was measured versus probe voltage, while the back gate voltage is swept slowly. The measurement geometry is shown in Fig. 3.1-B. I then numerically calculate a derivative from the IV curve, and create a 2D map of differential conductance versus probe (V_p) and back gate voltage (V_g). These 2D maps will be referred to as conductance maps.

I have investigated many samples. I will focus on the highest quality samples that

include an Al junction tested at several points in the aging process (Al-1A, Al-1B, and Al-1C), a second Al sample (Al-2), and two Cu junctions (Cu-1 and Cu-2). A few other samples have been studied in less detail, but generally confirm the effects presented here. The sample displayed in Fig. 3.1-A & B is Al-1.

One of these additional samples made using a different procedure is worth noting here. Due to highly variable results before the fabrication process reported here was settled upon, I wished to create a sample without any lithographic processing. To this end, I used a thin glass slide to cover half of a graphene flake. I knew that the glass slide was sufficiently close to the Si chip to create a fairly sharp metal edge by noting the Newtonian rings made between the two pieces of glass (implying subwavelength distances between the two surfaces). The flake was then placed into the evaporator and a Cr/Au lead was evaporated after heating the sample to 100°C to remove adsorbed water. Next, an Al lead was evaporated in a similar way. The flake and resulting device is displayed in Fig. 3.3.

The sample as fabricated showed ohmic behavior. After exposure to nitric acid and heat, the sample's resistance increased significantly. This sample was measured at 77K, and though the data is less complete than in the lithographed devices, it provided important direction on how to proceed in the later measurements. Nitric acid does not etch Al, it is merely an effective oxidizer, thus it could be used for such a sample with a large area lead. A similar device was made with a Cu lead, and with two Cr/Au leads. In this way, I could assure myself that the Cr/Au leads were not affected by the concentrations of nitric acid used in these studies. By using 65% nitric acid (fuming) Cr/Au leads can generally be removed given sufficient etching time since Cr is etched by nitric. Cu is greatly affected by nitric acid, and since metal is actually removed by the solution, very narrow leads are required to allow sufficient undercut of the acid before the Cu leads are significantly etched.

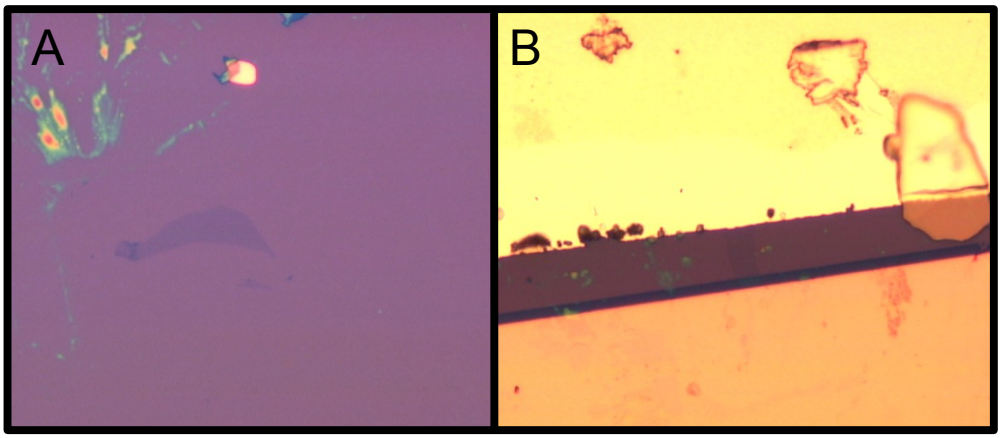

Figure 3.3: A: graphene flake before and B: after deposition of clean electrodes without the use of PMMA processing.

3.3 Theory of tunneling in graphene

I now develop a quantitative theory that I can use to analyze the data. Since the graphene DOS is much smaller than in metals, it cannot be assumed that the probe electrode used for tunneling does not itself gate the graphene. This situation merits a rethinking of some standard analysis. I use as a starting point the expression for a tunneling current into a two dimensional material. An explanation of this equation appears in the introduction. When tunneling into very thin films, the electron tunnels from a bulk metal, into a state that is confined in the direction perpendicular to the plane of the electrode. Thus there are electron in a box states in the perpendicular direction. Since graphene is nearly two dimensional, these states are exceptionally widely spaced (many volts), and in practice only the very first one can actually be accessed. Therefore, taking E_{nx} as the energy of the nth electron in a box state, $D(E, E - E_{nx})$ as the transmission coefficient at an energy E and a perpendicular energy E_{nx}, and $g_n(E - E_{nx})$ as the density of states (DOS) of the nth band the tunneling current at zero temperature [18]

$$J_n = \frac{e}{h}\int_{\mu}^{\mu+eV_p} g_n(E-E_{nx})D(E,E-E_{nx})dE \tag{28}$$

I assume that only n= 1 is important, and that $D(E, E-E_1) = D$. I justify the assumption of a constant transmission coefficient of the barrier in the section on inelastic tunneling, in particular, that the barrier height is much larger than the bias voltage. We, however; do not assume that μ stays constant while the probe voltage is changed. Then,

$$G = \frac{dJ}{dV_p} = \frac{De^2}{h}\left[g(\mu+eV_p)\left(1+\frac{1}{e}\cdot\frac{d\mu}{dV_p}\right) - \frac{g(\mu)}{e}\cdot\frac{d\mu}{dV_p}\right] \tag{29}$$

where $g(E) = g_1(E-E_1)$.

Normally, when looking at the tunneling conductance, the Fermi level is taken as constant, but in the junctions presented here, μ is a function of both V_p and V_g, and a capacitor model is used to express the relationship. The graphene chemical potential μ is measured from the Dirac point, as sketched in Fig. 3.1-C and D. Graphene is grounded via the Ohmic contact shown in Fig. 3.1-A or B. In equilibrium ($V_p = V_g = 0$), the graphene electro-chemical potential, $\mu + e\phi$, is equal to that of ground, that is set to zero, ϕ is the electrostatic potential, and $e = -1.602\cdot10^{-19}$C. Since the gate is well insulated from graphene, the graphene remains in equilibrium with ground at finite V_g.

At finite V_p, the current flows between the probe and the graphene, resulting in a potential drop across the graphene and the Ohmic contact. This potential drop can be neglected, because the resistance between the tunnel probe and graphene (typically $> M\Omega$) is much larger than the sum of the graphene resistance and the Ohmic contact resistance (typically $< 10k\Omega$), so the condition $\mu + e\phi = 0$ remains satisfied in graphene. To be precise, the electrochemical potential of the graphene beneath the probe is $eVR_G/(R_G+R_J)$ where R_G and R_J are the resistances to graphene and the

junction respectively. When $R_G << R_J$, the electrochemical potential is zero, and therefore high resistance tunnel barriers are preferable.

At finite probe and gate voltages, electrons will be attracted or repelled from graphene, because of the capacitive coupling to the probe and the gate. The change in the carrier density changes the graphene chemical potential, while the electrostatic potential adjusts to maintain equilibrium $\mu + e\phi = 0$. In the capacitor model,

$$C_p(V_p - \phi) + C_g(V_g - \phi) = -\sigma_0 - e\int_{\mu_0}^{\mu} g(E)dE \tag{30}$$

where C_p and C_g are the capacitances between the probe and graphene, and the gate and graphene, respectively, per unit area, and σ_0 and μ_0 are the charge density and the chemical potential at $V_g = V_p = 0$, respectively. It follows that $\sigma_0 = -(C_p + C_g)\mu_0/e$ for the initial doping of graphene. C_g is measured to be $124\mu\mathrm{F/m}^2$ on a test sample. The test sample was prepared by lithographically depositing several $1\mathrm{mm}^2$ Cr/Au pads onto a typical silicon wafer. A four probe LCR meter from SRI was used to detect the capacitance, and the stray capacitance of the probes was accounted for by measuring the capacitance with the probes just barely above the pad. This capacitance was subtracted in the final calculation, as it is in parallel with the SiO_2 capacitance as long as the contacts to the Si and Metal pad are low resistance.

In ideal graphene, $g(E) = g_0(E) = D_0|E|$, where $D_0 = 2/\pi(\hbar v_F)^2 = 1.47 \cdot 10^{18}/(eV\,m)^2$ is the DOS per unit energy and unit area, assuming $v_F = 1.0 \cdot 10^6\mathrm{m/s}$. As a function of V_p and V_g, the resistance of graphene has a maximum when the Fermi level is at the Dirac point, $\mu = 0$. Substituting $\mu = 0$ and $g(E) = g_0(E)$ in Eq. 30, the solution for μ_0 is

$$\mu_0 = -sgn(C_pV_{p,D}+C_gV_{g,D})\left[-\frac{C_p+C_g}{D_0e^2} + \sqrt{\left(\frac{C_p+C_g}{D_0e^2}\right)^2 + \frac{2|C_pV_{p,D}+C_gV_{p,D}|}{|e|D_0}}\right], \tag{31}$$

where $V_{p,D}$ and $V_{g,D}$ are the probe and the gate voltages, respectively, at the resistance maximum. This relation will be used to obtain the average doping in graphene under the probe and outside the probe.

Though a great deal can be drawn from these analytic equations, and they can be explicitly solved for the ideal graphene DOS, $2|E|/\pi(\hbar v_F)^2$, they can become rather complicated if one tries to insert a non-ideal value for the DOS, and so I have set out to calculate conductance maps numerically. I use a tight binding hamiltonian with periodic boundary conditions and a potential of randomly placed charged impurities, sketched in Fig. 3.4-A. The Hamiltonian is then written as [49]

$$H = \sum_{i}^{N} E_i c_i^\dagger c_i + \sum_{i,j}^{n.n.} t_{ij} c_j^\dagger c_i + \frac{Ze^2}{4\pi\epsilon} \sum_{i}^{N} \sum_{k}^{N_{imp}} \frac{c_i^\dagger c_i}{r_{ik}} \tag{32}$$

where $t_{ij} = t = 2.25$eV is the hopping energy, $E_i = E = 0$ is the site energy, and N_{imp} corresponds to an impurity density of $\sim 3 \cdot 10^{11} cm^{-2}$. The hopping energy is chosen so that the final result for the Fermi velocity agrees with $1.0 \cdot 10^6 m/s$. I use an even number of oppositely charged impurities so that there is no net doping, and I may enforce a doping of my choosing (σ_0 in Eq. 30) when constructing a conductance map. I simulated an area of graphene corresponding to roughly 11,000 unit cells, or 600nm^2. The eigenvalues $E(\alpha)$ are derived from the matrix, the DOS is obtained as $g(E) = \sum_\alpha \delta(E - E(\alpha))$, and a $5meV$ broadening was introduced to the eigenvalues to create a continuous DOS.

Fig. 3.4-B displays a typical DOS, indicating the fluctuations with energy. Also shown is the same spectrum with 50 meV broadening, showing the correct functional dependence. In the vicinity of the Dirac point, the fluctuation amplitude is comparable to the average DOS. The fluctuations will prevent clear observation of the tunnel-conductance suppression near the Dirac point. It is important to understand that far away from the Dirac point, the fluctuations are weak and the density of states is close to linear. Realistically, the coulomb interactions in graphene are screened [8],

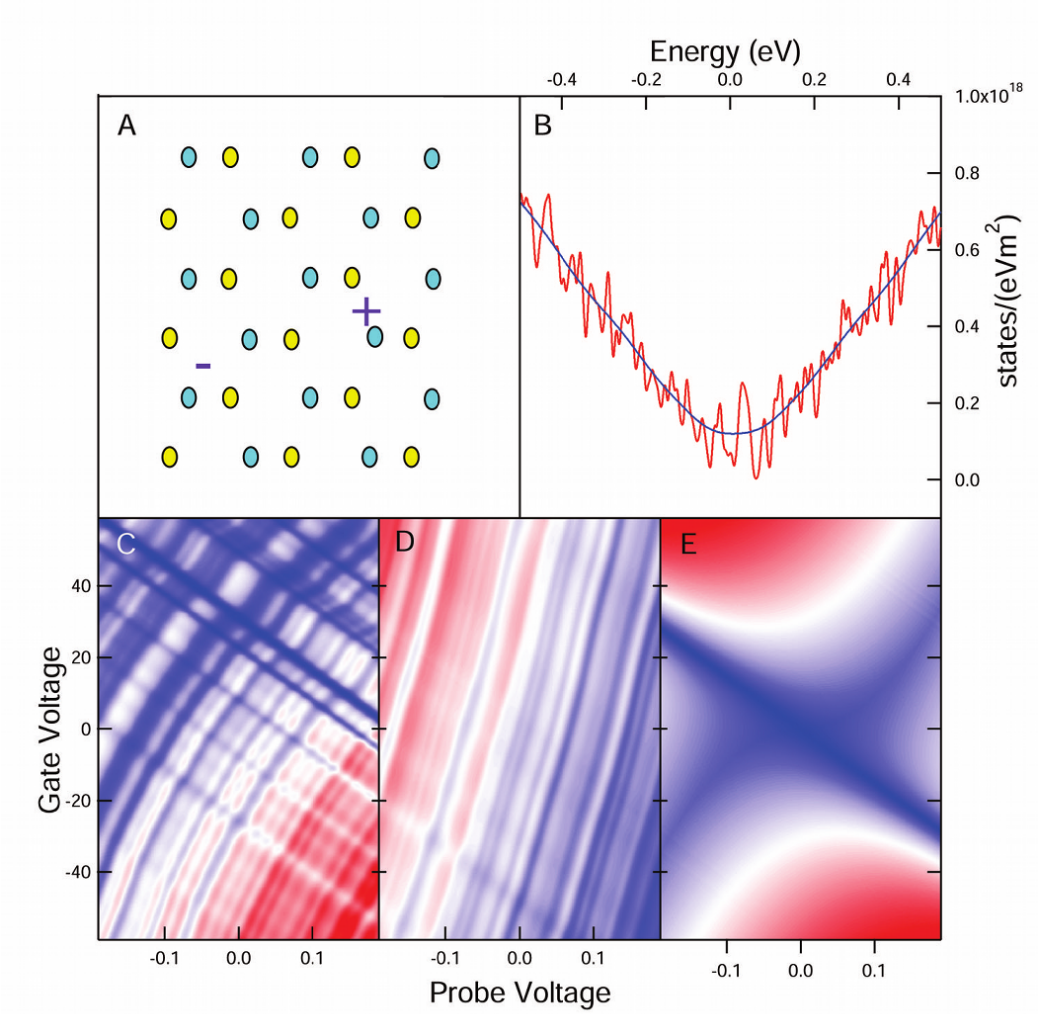

Figure 3.4: A: The graphene lattice with randomly placed impurities. B: Calculated DOS with 5 meV smoothing function (red), and 50 meV (blue). C: Simulated conductance map with .150 eV p-doping. D: A conductance map of the same DOS with .4 eV n-doping. E: Simulation of conductance map for the ideal graphene density of states. There are two suppressions in the conductance as the probe energy (parabolic line), and Fermi energy (negative sloping line) pass through the Dirac point.

but the unscreened coulomb potential used in ref [49] creates fluctuations in the DOS. To explain the conductance maps, only the fluctuations are necessary, and their physical origin is a topic for more detailed investigation. In fact it would have been possible to produce the same qualitative conductance diagrams just by adding noise to an ideal graphene DOS.

To obtain a conductance map, I solve Eq. 30 numerically to obtain μ and $d\mu/dV_p$ as a function of V_p and V_g, and calculate the conductance with Eq. 29. A conductance map constructed at $\mu_0 = -.15eV$ and $\mu_0 = +.4eV$ doping is displayed in Fig. 3.4-C and D repsectively. Clearly, two sets of parallel lines, one with positive slope and one with negative, are present in the maps.

The positive and negative sloping lines in the conductance map arise when $\mu + eV_p = const$ and $\mu = const$, respectively. For example, if V_p and V_g are varied so that $\mu + eV_p = const$, the upper bound of the integral in Eq. 28 is constant, so the contribution to the differential conductance from the upper bound is constant. A similar condition holds for the lower bound, if V_p and V_g are varied so that μ is constant.

To see how this translates into the lines seen in the conductance maps, take the differential of Eq. 30, and finding how the back gate electrode must change to enforce either $\mu + eV_p = constant$ or $\mu = constant$

$$\left.\frac{dV_g}{dV_p}\right|_{\mu+eV_p} = 1 + \frac{e^2 g(\mu)}{C_g} = 1 + \frac{C_Q}{C_g} \tag{33}$$

$$\left.\frac{dV_g}{dV_p}\right|_{\mu} = -\frac{C_p}{C_g} \tag{34}$$

where C_Q is the quantum capacitance as defined in [23] replacing the graphene DOS for that of a 2DEG. The slope of lines of constant energy $\mu + eV_p$ always have positive slope, and are related to the graphene DOS at the Fermi level. The curvature of the positive sloped lines $\mu + eV_p = const$ is

$$\left.\frac{d^2V_g}{dV_p^2}\right|_{\mu+eV_p} = -\frac{e^3}{C_g}\frac{dg(\mu)}{d\mu} \tag{35}$$

Fig. 3.4-E shows a conductance map calculated for an ideal, undoped graphene DOS, to clearly illustrate how Eq. 14-16 are interpreted. In ideal graphene, there are no DOS fluctuations and there is only one sharp feature in the DOS, the Dirac point. There are two distinct signatures of the Dirac point in the conductance map. One is the conventional conductance suppression at energy $eV_p + \mu = 0$, that leads to a positive sloping line in the conductance map. The curvature of the positive sloping line is $sgn(\mu)|e|^3 D_0/C_g$. The curvature magnitude is constant except at the inflection point. The curvature is positive or negative, for $\mu > 0$ (n-doped) and $\mu < 0$ (p-doped), respectively. The second signature of the Dirac point is a conductance minimum along the line of $\mu = 0$. As V_g is varied, the second minimum shifts along the line $C_g V_g + C_p V_p = 0$. Thus, for a given gate voltage, the probe voltages corresponding to the two Dirac-point conductance minima have opposite signs and different magnitudes. The two lines intersect at $V_p = 0$. Recently, an STM experiment on exfoliated, backgated graphene has revealed a conductance map resembling the ideal case [50], though in making comparisons it should be noted that STM typically uses a bias convention reversed from that presented here.

In finite size disordered graphene, the DOS fluctuations with energy lead to multiple minima and maxima in conductance near the Dirac point. A set of parallel positive sloping lines in the conductance map arise. Along those lines, $eV_p + \mu$ is constant, equal to the energy of a feature in the graphene DOS. The curvature of the positive sloping lines changes from negative to positive in the vicinity of $\mu = 0$. Among the various positive sloping lines, the inflection shifts following the negative sloped line $C_g V_g + C_p V_p = const.$ The negative curvature in the positive sloping lines in Fig. 3.4-C indicates p-doping, while the weak positive curvature in the positive sloping line in Fig. 3.4-D indicates n-doping. I will show that Fig. 3.4-C and Fig. 3.4-D agree with the conductance maps of Cu and Al junctions respectively. The strong suppression in the conductance of ideal graphene is difficult to observe due to the

DOS fluctuations near the Dirac point. However, the inflection (flattening) remains visible, since the fluctuations move in parallel despite disorder. Thus the inflection is a more robust signature of the Dirac point in the tunneling data.[1]

3.4 Experimental results and discussion

3.4.1 FET geometry

Now I will discuss the results of the first setup, sketched in Fig. 3.1-A. This experiment gives us a global view of the capacitance of the probe electrode, and the doping level of the graphene under the probe. The resistance between the two Ohmic leads, that is the two-probe resistance, was measured using a lock-in technique, with an excitation current of 1μA. The two-probe resistance versus back gate voltage (V_g), at zero probe voltage, ($V_p = 0$), is shown in Fig. 3.5-A for sample Al-1B. The two-probe resistance has a maximum at $V_g = -.4$ volt, indicating a Dirac point in bulk graphene. Since the maximum location is very close to zero volts, this indicates that the doping in graphene is very weak. The doping in this sample is weak by random chance; among different samples, the location of the maximum varies by up to 20 volts.

Next, the two-probe resistance is measured while sweeping the probe voltage at fixed back gate voltage, as shown in Fig. 3.5-B for sample Al-1B. Again, the two-probe resistance exhibits a maximum in resistance, but the location of the peak is very different from that measured in bulk graphene. The effect of the probe and back gate voltages can be separated by mapping resistance in colorscale versus probe voltage and back gate voltage as seen in Fig. 3.5-C. The peak beneath the probe is much smaller due to the smaller area beneath the probe as compared to the area not underneath the probe, so the bulk Dirac peak has been subtracted from Fig. 3.5-C. There is no visible effect on the bulk peak by the probe voltage. Similar patterns

[1] I have also obtained the local DOS at site i, $g_i(E) = \sum < \alpha|c_i^+ c_i|\alpha > \delta(E - E(\alpha))$, found the corresponding conductance map (assuming tunneling into the site i only), and find qualitatively similar behavior as in Fig. 3.4 C and D. The local DOS would be appropriate for a pinhole, while the global DOS $g(E)$ would be for a uniform tunnel junction.

have been seen in other double gated samples. [51, 52] For Cu samples, the two-probe resistance also exhibits a maximum in resistance versus V_p, as shown in Fig. 3.5-D for sample Cu-1, but the maximum is located at positive probe voltage.

The slope of the resistance maximum in Fig. 3.5 B,C, and D indicates the capacitance ratio of the probe with the graphene and back gate with graphene, and the intercept of the peak at zero back gate voltage is the Dirac point underneath the junction. The capacitance ratio for the tunnel probe and the back gate is obtained by locating the maximum in the curves shown in Fig. 3.4-B and D and finding the best linear fit of the maximum location versus V_g. This capacitance ratio gives us a global measure of the junction thickness, and is 71.9 in Al-1B, 32.2 in Al-1C, 73.2 in Al-2, and 85 in Cu-1. I will discuss the capacitance ratio again, after discussing the tunnel spectroscopy results that lead to a higher capacitance ratio.

Fig. 3.6 shows the same sample as Fig. 3.5-C, but at a further point in the aging process. Here, the background is sufficiently weak so that both the bulk and top gated resistance maxima are visible.

In the case of bulk graphene (outside the probe), $C_p \ll C_g$ and I obtain $\mu_0 = +0.020eV$, indicating weak doping. Beneath the probe I obtain $\mu_0 = +.25eV$ for sample Al-1B, sample $+.22eV$ for Al-1C, $+.29eV$ for Al-2, and $-.15eV$ for Cu-1. I would like to stress that all Al junctions tested are n-doped, all Cu junctions are p-doped, and that this doping differs from that in the bulk graphene. This claim will be further verified by the tunneling spectra. Note also that this is a global measure of the doping under the probe. That is, μ_0 represents the average doping level over the entire area under the probe.

3.4.2 Tunneling geometry

To study the tunneling spectra, the set-up sketched in Fig. 3.1-B was used. The data for the sample without lithographic processing is displayed in Fig. 3.7. The raw

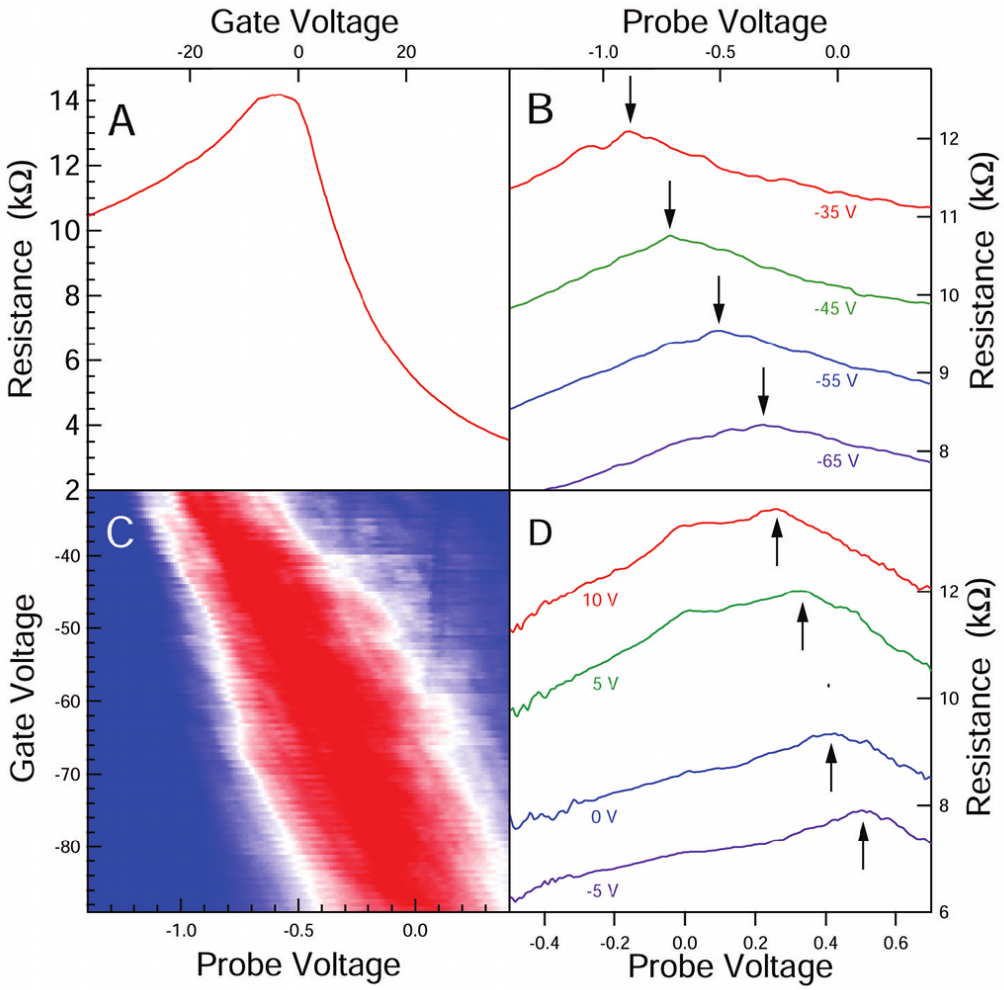

Figure 3.5: A: The back gate voltage response of bulk graphene in Al-1B at $V_p = 0$, the Dirac point is near zero, indicating weak doping. B: Several scans of the probe voltage response at different back gate voltages for Al-1B, the Dirac point can be seen to shift towards zero probe voltage with large negative back gate voltage. C: 2D colorscale of 2 probe resistance with probe and back gate voltages for Al-1B. The slope of the Dirac point beneath the probe is measured to be 72, and the bulk Dirac peak has been subtracted for clarity. D: Several scans of the probe voltage response at different back gate voltages for Cu-1.

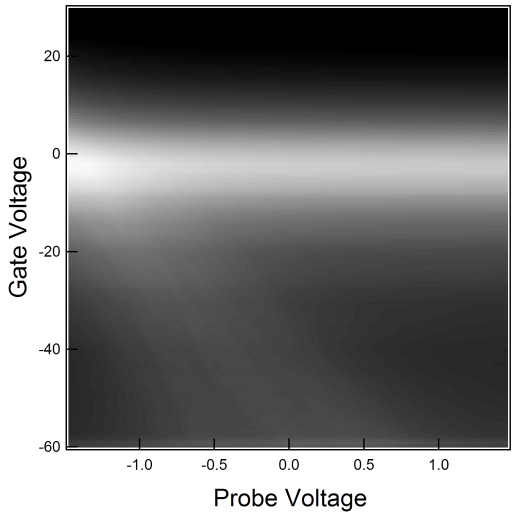

Figure 3.6: A top gate vs back gate map of the two probe resistance for sample S1-C. In this case the gate resistance was 200MΩ.

data consists of I-V curves as seen in Fig. 3.7-B, and a numerical derivative is taken to obtain the conductance curves. Conductance curves were taken at several gate voltages, and several striking features can be seen. One is that there is a substantial increase in conductance around ±65meV, another is that there are several repeatable fluctuations in the spectra, and finally, this spectra, does not display the spectra predicted by the elastic tunneling theory laid out earlier in Sec. 3.3.

For the lithographically manufactured samples, Fig. 3.2-A shows an example of the I-V curves for Al-1B at both 77K and 4K, as well as the plot of the current vs probe and gate voltage at 4K in Fig. 3.2-B. Once again, a derivative is taken vs. the probe voltage to obtain the conductance. In this way I have created conductance maps for all of the measured samples.

Fig. 3.8-A, B, and C display the conductance dI/dV_p versus bias voltage V_p at 4.2K, for sample Al-2, Al-1B, and Al-1C, respectively, at $V_g = 0$. The probe voltage range is smaller than the ranges in Fig. 3.5-B, C, and D and Fig. 3.6, because the current becomes noisy at large bias, $|V_p| > 0.2V$. Similarly, the current becomes

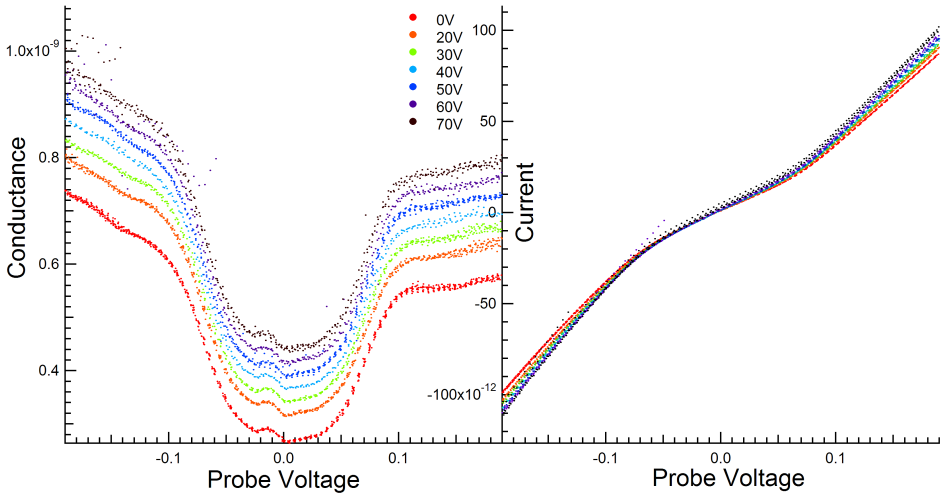

Figure 3.7: A: Conductance vs probe voltage at different gate voltages for the Al device featuring clean leads at 77K. B: The I-V curves for the same device, corresponding to the same gate voltages.

noisy if the back gate voltage is large, $|V_g| > 60V$. Fig. 3.8-D, E, and F display the conductance maps, defined as $G(V_p, V_g) = dI/dV_p$ as a function of V_p and V_g. As noted above, the figures correspond to the samples in Fig. 3.8-A, B, and C, respectively. Fig. 3.10-A and B display the conductance maps for Cu-1 and Cu-2.

The conductance in Fig. 3.8 exhibits fluctuations that are reproducible with bias voltage. Fig. 3.8-G through I display the conductance with a low frequency background subtracted, this subtraction greatly enhances the features under discussion. Fig. 3.10-C displays the conductance averaged over all back gate voltage that demonstrates the emergence of inelastic threshold in large resistance samples.

The central observation of this chapter can be seen in the positive and negative sloping lines of Fig. 3.8-D through I, and Fig. 3.10-A and B. The positive sloping lines are indicated by full lines, while the negative sloping lines are indicated by dashed lines. As I explained in Sec. 3.3, the positive sloping lines are related to the DOS in graphene, while the negatively sloping lines are related to the capacitance ratio

between the tunnel and the gate electrode.

The Cu samples in Fig. 3.10 display curvature in the positive sloping lines, and in fact all Cu samples tested have displayed curvature in the conductance maps. If the slope of these lines is related to the DOS as I claim, these lines should display an inflection when passing through the Dirac point. I see just this in Fig. 3.10-A, though the lines do not flatten to nearly zero since disorder broadens the DOS.

A low resistance sample is also shown. The fluctuations are still observable, showing that such behavior can be seen in samples even approaching the conductance quantum. In this case the sample is $30k\Omega$, and is shown in Fig. 3.9. Both sets of parallel lines can be seen, though here they are broadened compared to the other samples, and the negative sloping lines are less well resolved.

All Al samples display positive sloping lines that are nearly linear. This would be expected if the doping were high, as in Fig. 3.8-D since more voltage is required to shift the Fermi level to change the curvature significantly. The doping predicted by the FET experiment should allow us to access the Dirac point in the lower portion of some Al junctions, that is, the positive sloping lines should display an inflection in that region. Since no inflection is evident I suppose that the FET experiment is not an accurate predictor of the doping level in the tunnel spectrum. The discrepancy between the FET results and the tunnel data could be explained by nonuniform doping that is common in exfoliated graphene. [37, 38] If the tunneling junction were point like (a pinhole), tunneling would depend on local doping, whereas the FET experiment would depend on average doping in graphene under the entire probe.

Thus in Fig. 3.8-G-I, Fig. 3.9, and Fig. 3.10-B, doping prevents us from observing the Dirac point within the window of probe and gate voltage that keeps the signal noise acceptably low, though the negative curvature in Fig. 3.10-A and B, and the slight positive curvature in Fig. 3.10-G and H (indicating p and n doping respectively) can clearly be observed. Despite the lack of a Dirac point in all data, there is still

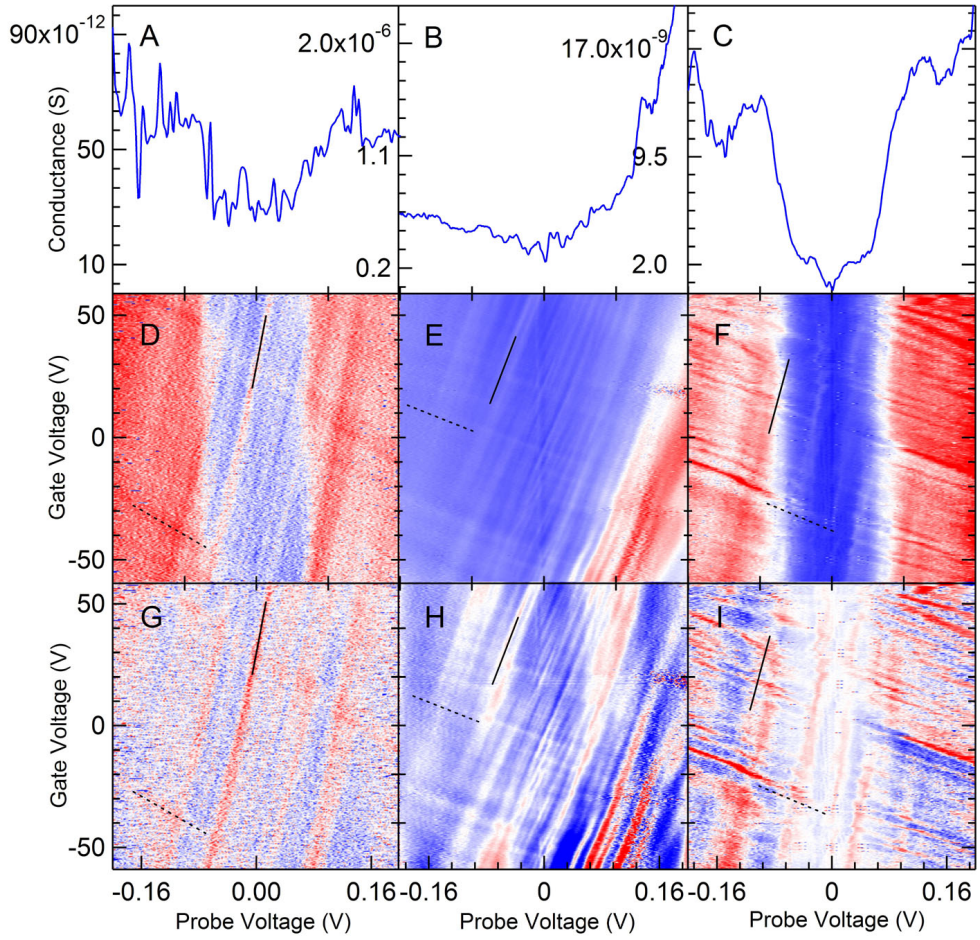

Figure 3.8: A-C: dI/dV vs Probe Bias at zero back gate voltage for three different junction resistances in Al-2, Al-1B, and Al-1C. D-F: 2D conductance maps of A-C vs probe voltage and back gate voltage. Two sets of parallel lines are visible. G-I: D-F after subtracting the background conductance, enhancing the two sets of parallel lines.

enough information to prove my interpretation.

The lines of constant Fermi level $\mu = const$ are always negative and equal to the capacitance ratio of the two electrodes as discussed in Sec. 3.3. This is a local capacitance ratio specific to the small area where the tunneling takes place, and is 160 for Al-1A, 101 for Al-1B, 104 for Al-1C, 133 for Al-2, 120 for Cu-1, and 180 for Cu-2. The fact that this capacitance ratio is much higher than the one stated earlier from the FET measurements indicates that tunneling occurs in a portion of the junction that is thinner than the average junction thickness. Since the oxidation proceeds inward through the interface, it creates thicker oxide at the edges, and a thinner one near the center. A thickness measurement of the junctions is not strictly possible using either capacitance value, as I cannot know the dielectric constant of the insulating layer. For the Al junctions, the thickness to dielectric constant ratio can be estimated from the capacitance of the junction, leading to a typical thickness of 6nm for a dielectric constant of 8. Since oxide is formed in ambient conditions, with ambient humidity, the dielectric constant could vary from it's ideal bulk value of 8.9. Electron tunneling over such a thick dielectric is not possible, suggesting that any tunneling would be confined to pinholes.

Eq. 14 can also be used to derive the local value of doping in the area that contributes to the tunnel conductance. By assuming an ideal graphene DOS, $g_0(\mu_0) = D_0|\mu_0|$, and measuring the positive slopes in conductance map, the doping level is $+.39eV$ in Al-1B, $+0.76eV$ in Al-1C, and $+.47eV$ in Al-2. I can estimate these doping for the Al junctions because at large doping levels the Fermi level doesn't shift much over the conductance map, and the lines remain close to linear. The sign is chosen as positive because of the weak positive curvature. These doping levels should be compared with those from the FET measurements, $+.25eV$, $+.22eV$, and $+.29eV$, respectively. Cu junctions, on the other hand, consistently demonstrate positively sloping lines with a curvature described by Eq. 14 and 16. By adjusting the doping

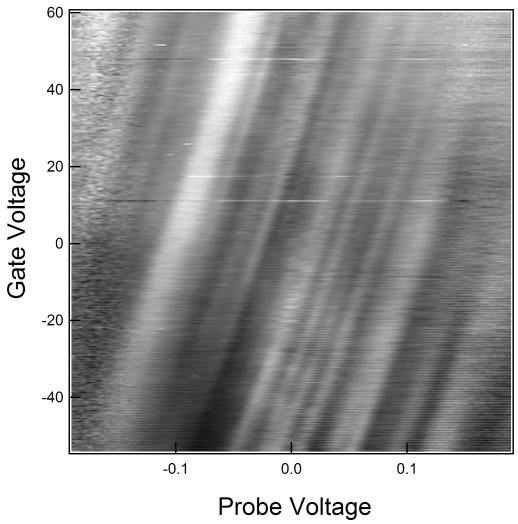

Figure 3.9: A spectra of a low resistance ($\sim 30k\Omega$) junction; notice that both sets of lines are still present, but much broader, as there is stronger coupling between the tunnel probe and graphene.

level so that the slope is equal to $1 + e^2 D_0 \mu_0 / C_g$ at zero probe and gate voltage, I obtain the correct fit of lines on the conductance map and an estimate of μ_0. The fit lines obtained in this manner are displayed in Fig. 3.10-A and B, and yield doping values of $-.05eV$ in Cu-1 and $-.25eV$ in Cu-2. The curvature of the best fit lines is independent of the doping level, contains no free parameters, and agrees with the data.

Considering that there is no immediate reason to connect these lines to the graphene DOS, it is remarkable that the positive slopes in the conductance map lead to the Fermi level of graphene close to that in the FET experiment. That is, multiplying the measured positive slope with the back gate capacitance, and dividing it with D_0, produces not only the correct order of magnitude, but also the Fermi level that agrees within a factor of two with the Fermi level measured by the FET experiment. The slope of the positively sloping lines *is* the DOS of graphene. In addition, the lines of constant energy that display curvature, given by Eq. 14 and 16, agree

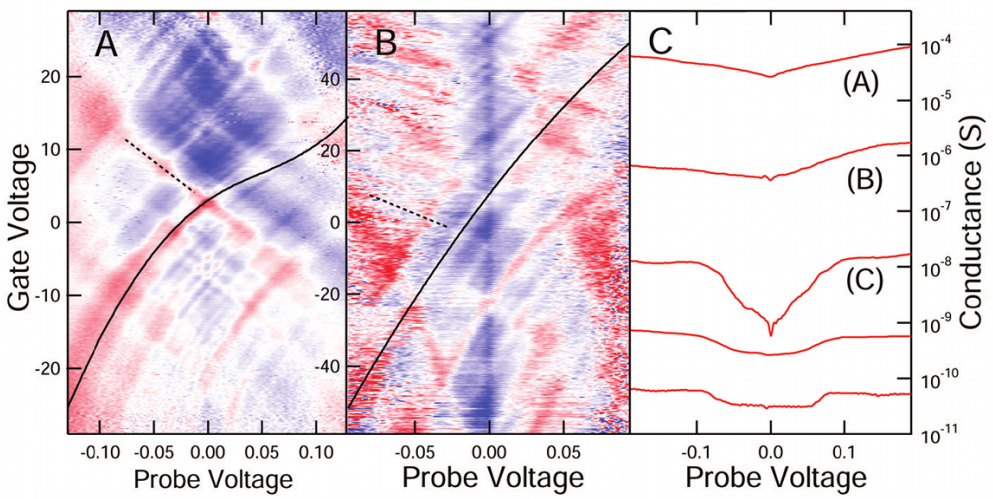

Figure 3.10: A and B: Conductance maps for Cu-1 and Cu-2, respectively. The superimposed lines are explained in the text. C: Conductance vs probe bias averaged over many back gate voltages, five different Al samples are displayed here, the top three being from Al-1A-C. The phonon resonance can be seen to emerge at high junction resistances.

well with the measurement with only the doping level as an adjustable parameter.

3.4.3 Inelastic tunneling

Now I will discuss inelastic tunneling. Fig. 3.10-F shows that there are features, at about $\pm 65mV$, that do not shift with back gate voltage. Similar conductance thresholds have been observed in scanning tunnel microscopy of exfoliated graphene [37]. They were attributed to inelastic electron tunneling involving an electron transition in graphene with a phonon emission. In these samples, the phonon feature is observed only in high resistance samples exceeding 5MΩ in tunnel resistance, restricting the discussion to the Al junctions. Fig. 3.10-C displays the tunnel conductance versus bias voltage in several samples, covering 7 orders of magnitude in conductance. Curves A, B, and C are obtained by averaging the conductance versus V_p over different V_g in Fig. 3.8. These curves are obtained in the same sample at various stages of aging. The remaining curves were obtained in different samples. The transition at $\pm 65mV$ is

clearly seen in samples with resistance $50G\Omega$, $5G\Omega$, and, $1G\Omega$, while lower resistance samples do not exhibit strong thresholds.

This trend with the tunnel resistance agrees with the explanation from ref [37, 53] in terms of inelastic tunneling with an electron-phonon transition. In an ideal planar graphene tunnel junction, the momentum component of electrons parallel to the plane must be conserved in tunneling [54]. The Fermi wavevector in Al, $k_F = 1.75 \cdot 10^{-8}\text{cm}^{-1}$ is close to the magnitude of the momentum at the K-point in graphene, or $1.70 \cdot 10^{-8}\text{cm}^{-1}$. As a result, one can always find a state on the Al Fermi surface with an in-plane momentum equal to the electron momentum in graphene. In that case, both the in-plane momentum and the energy are conserved in tunneling and the elastic tunneling at zero bias voltage is observed in this system. However, the wavefunctions with large wavevector components parallel to the tunneling interface decay rapidly according to a wave function that behaves like [54]

$$\psi \sim exp(-(2m_e(V - E_F)/\hbar^2 + k_{||}^2)^{\frac{1}{2}} z) \tag{36}$$

The $k_{||}$ term increases the effective barrier to tunneling in the case of graphene where $k_{||}$ is the K-point. For electrons tunneling into the K-point of graphene, $\hbar K^2/2m_e \approx 11eV$. I believe, therefore, that band bending is not an issue for the bias range of at most 200meV, and is irrelevant in Eq. 4. However, this does not preclude phonon assisted tunneling.

The energy of the out-of-plane acoustic phonon in graphene with wavevector $\mathbf{K}$ is approximately $65meV$. So, at a bias voltage of $65mV$ or above, electrons can enter or exit graphene via a higher order, two step process, involving a virtual state at the graphene Γ-point that has a wavevector of length zero. [37]

As the barrier thickness increases by aging, the resistance of the elastic tunnel channel increases much more rapidly (exponentially) than the resistance of the inelastic tunnel channel (roughly constant). In the sample studied in this paper, at the

junction resistance of about 5MΩ, the rates of elastic and inelastic tunneling become comparable, and a weak resonance emerges.

It can be seen directly from Fig. 3.8-D,E, and F that the lines are unaffected by inelastic tunneling events, as they can be seen to pass through the inelastic thresholds without changing their slope. This demonstrates that the inelastic and the elastic tunneling processes are added in parallel, as independent tunneling channels.

3.5 Conclusions

To conclude this chapter, I have presented a solid state realization of a tunnel junction into graphene, and introduced a measurement technique that extracts information of the graphene region under the tunnel junction. I determined the doping level of the graphene under the junction, both locally at the tunnel spot and globally averaged over the entire junction area, and find doping to be significantly different than in the region outside the junction. In Al junctions, doping is strong on the n-side, in Cu junctions, doping is small to moderate on the p-side. I observe mesoscopic fluctuations in the tunnel DOS of graphene that shift with applied back gate voltage in accordance with the electronic DOS in graphene, and an inelastic conduction threshold associated with high resistance junctions. An important point is that the electrostatic gating of graphene caused by the tunnel probe needs to be considered, and understanding its effect provides an important tool for interpreting tunneling experiments in graphene. Much of the data and analysis in this chapter is summarized in Ref. [55].

CHAPTER IV

GRAPHENE TUNNELING IN A MAGNETIC FIELD

4.1 Introduction

Mesoscopics is the study of what general effects can be observed in samples that are smaller than the carrier phase coherence length. [5] The disorder leads to quantum interference effects that can be measured by transport.

As I showed in the last chapter, though disorder and imperfections in tunneling contacts to graphene create a situation where conductance versus bias can be unsensible, two sets of lines in the conductance map exhibit predictable properties that can be used to identify parameters in the material. Now the material is placed in a magnetic field and there are three different 2D plot options: V_g vs. V_p, B vs. V_p and B vs. V_g. The goal is to identify the important features of each of these plots and decide which maps, or combination of maps can be used to derive information about the formation of Landau levels in a disordered piece of graphene.

Again, I also look to the observation of graphene properties in the tunnel junction as evidence that close proximity to a metal can leave the graphene spectrum weakly perturbed. In addition, I can identify an unusual form of Coulomb blockade physics, and an illustration of the mobility gap that plays an important role in the quantum Hall effect.

4.2 Landau levels and disorder

Turning on a magnetic field has a strong effect on the energy levels in a material. As stated before, the energy levels of graphene are quantized into highly degenerate Landau levels, and vary as the square root of the field and the Landau level index.

This break up of orbits is complicated by the disorder potential. As long as certain requirements are kept, disorder will not completely destroy the Landau level structure, but merely broaden the levels, as there will be orbits of slightly different energies, but a common Landau index.

The requirements on the disorder potential can be broken up into three contributions, a weak potential, a scattering potential, and a smooth potential. [56] The weak potential must have a strength less than $\hbar\omega_c$ throughout the sample, the scattering potential must be short range in the sense that there is some length $l_m$where the sample is potential free for more than the magnetic length, and the smooth potential must have a gradient less than $\hbar\omega_c/l_m$.

A spatial picture of Landau levels in the presence of disorder in the quantum Hall regime is a combination of localized and delocalized states. The extended states are much rarer, and in high quality samples are found near the edges (thus they are sometimes called edge states). The coexistence of these two types of states is what creates the mobility gap necessary for the quantum Hall effect. In high quality samples, each edge state is on opposite sides of a rectangular strip, with localized states located between them. A region of low electron density, or an incompressible region, prevents transport between neighboring states except by a tunneling process. Thus the forward and backward moving extended state are kept far apart, and current flows through ballistic channels, leading to the zero longitudinal resistance and quantized Hall resistance that characterize the QHE. [5]

As disorder is increased in a sample, the Landau levels begin to mix, and motion between different states becomes possible, leading to finite back-scattering, and an imperfect QHE. [56] In this chapter I demonstrate that this story can actually be seen to unfold in a tunnel junction between Cu and graphene. The disorder potential further creates a situation where single electron tunneling can occur between a localized state, and an extended state that is connected to the macroscopic leads. In high

field, the theory of single electron tunneling is applicable to resonances observed in the data of several samples, and allows us to define capacitances between the metal and localized state, and the localized state and the extended state.

4.3 Fabrication

The fabrication of tunnel junctions for use in a magnetic field is similar to those junctions tested in zero field. Aluminum junctions aged too fast to be transferred into the cryostat that contains a superconducting magnet capable of 12T magnetic fields. Therefore, copper junctions were used. In one case the junction was only partially overlapping the sample, and in two other cases the junction was entirely overlapping. In all cases, the probe was too narrow to be a truly efficient gate, however; double gate experiments similar to those performed in the zero field experiments were performed when possible.

Cu junctions were directly evaporated onto graphene through an MMA/PMMA mask patterned by e-beam lithography. Once the mask was lifted off in acetone, the device was placed in dilute nitric acid ($\sim$12% HNO_3) for several seconds, and then rinsed with DI water, isopropanol, and blown dry. The acid promotes oxidation of the Cu, and some junctions become highly resistive after this treatment (>1 MΩ), afterwards they continue to age, though slowly, taking several weeks to fully oxidize.

Narrow junctions (<200nm) were used to insure that the undercutting of the acid occurred before the lead was overetched. Though tarnishing could be seen in the leads, the fact that the source and drain were highly conductive, and conductance was not severely suppressed at low temperatures, means that the junction provided the primary mode of resistance in the circuit. The few leads that did exhibit large changes in conductance at low temperatures were rejected.

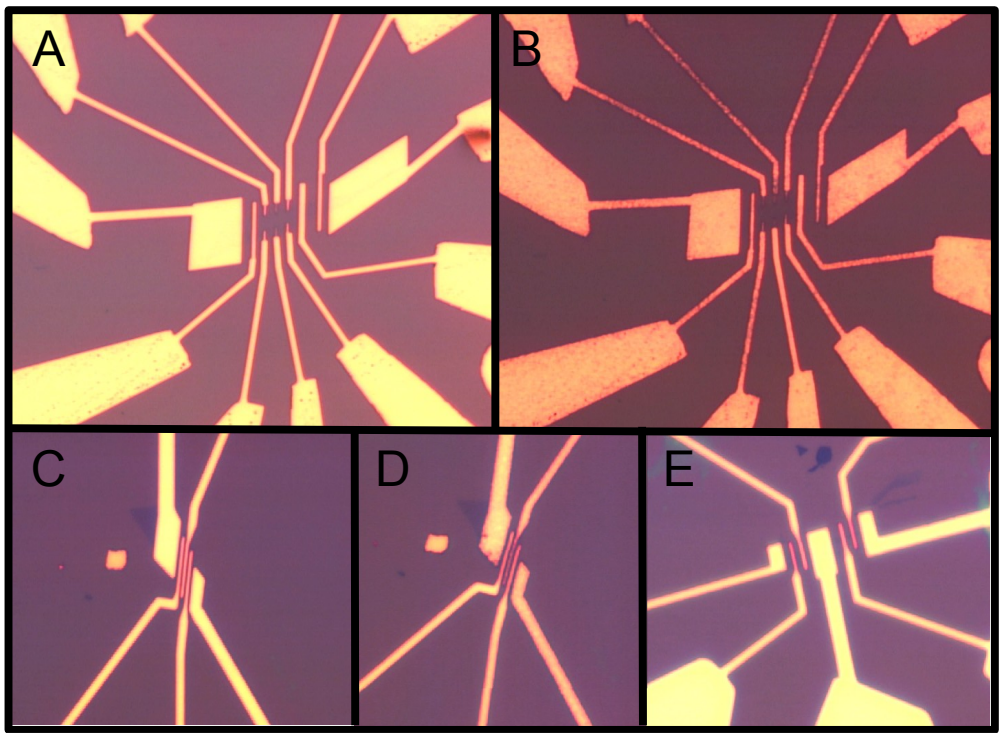

Figure 4.1: A & B: Cu sample with many leads before and after acid treatment, one lead in particular is discussed as sample CuB-1. C & D: Cu sample with several leads before and after acid treatment, referred to as CuB-2. E: Cu sample with several leads referred to as CuB-3. No acid was required to achieve a high resistance in one lead, perhaps owing to the narrowness of the actual graphene flake.

4.4 Application of the tunneling theory

From the earlier theory of electron tunneling I can form a qualitative picture of how a disordered Landau level spectrum should look in a gate map. Lines of constant energy will form an upward sloping staircase as the Fermi level passes through regions of high DOS followed by low DOS. Lines of constant Fermi level will trace out a series of peaks as the tunneling probe energy passes through each Landau level. A consequence of the earlier theory is that lines of constant energy and lines of constant Fermi level always meet at zero bias ($\mu = \mu + eV_p$ when $V_p = 0$). Therefore it is not terribly surprising to see a series of criss-crossed lines near zero bias voltage. At high fields, near the top and bottom of Landau levels new physics appears in the form of single electron tunneling. This was discussed in the introduction, and will be discussed with respect to the experimental results later in this chapter.

At most energies and fields I do not observe the single electron tunneling effect, so an extension of the prior theory to include magnetic fields may in fact be worth the effort. The main conceptual difference is that the density of states $D_0|E|$ must be replaced by $\sum_{i=-\infty}^{\infty} \frac{4eB}{h}\delta\left(E - \mu_0 - v_F sgn(i)\sqrt{2e\hbar B|i|}\right)$. An important fact to note is that this expression does indeed transform into the original expression for the density of states at low field. To see this the expression is integrated over a small energy interval, and calculate the number of states between $\epsilon - \delta\epsilon/2$ and $\epsilon + \delta\epsilon/2$ in the limit of low field. In this limit, it is always possible to choose a small enough B such that there exists a discrete state that is less than $\delta\epsilon/2$ away from ϵ.

$$\lim_{B\to 0} \sum_{i=-\infty}^{\infty} \lim_{\delta\epsilon\to 0} \int_{\epsilon-\frac{\delta\epsilon}{2}}^{\epsilon+\frac{\delta\epsilon}{2}} \frac{4eB}{h}\delta\left(E - \mu_0 - v_F sgn(i)\sqrt{2e\hbar B|i|}\right) dE \tag{37}$$

As the magnetic field goes to zero, the Landau levels become closer and closer together, meaning that it becomes more and more accurate to approximate the Landau index as a real number rather than an integer. In this case, the highest state i_{max}

with energy less than $\epsilon + \delta\epsilon/2$ is $i_{max} = (\epsilon + \delta\epsilon/2 - \mu_0)^2/2eB\hbar v_F^2$ and the lowest state with energy greater than $\epsilon - \epsilon/2$ is $i_{min} = (\epsilon - \epsilon/2 - \mu_0)^2/2eB\hbar v_F^2$. The number of states in the interval is thus $i_{max} - i_{min}$ and neglecting terms smaller than order $\delta\epsilon$ the number of states in the interval is:

$$\frac{4eB}{h}\frac{2\left|\epsilon-\mu\right|\delta\epsilon}{2eB\hbar v_F^2} = \frac{2}{\pi(\hbar v_F)^2}\left|\epsilon-\mu\right|\delta\epsilon = D_0\left|\epsilon-\mu\right|\delta\epsilon = g(\epsilon-\mu)\delta\epsilon \tag{38}$$

Aside from this substitution, I proceed as before, but complicate matters by including a magnetic field, this has little effect on the formula for conduction other than a more pronounced ZBA at high fields. The changes are to the electrostatics of the problem that are greatly affected by the density of states.

$$C_p(eV_p + \mu_F) + C_g(eV_g + \mu_F) = -\frac{4e^3 B i_F}{h} \tag{39}$$

where i_F is the highest Landau index at or below the Fermi level, and $\mu + e\phi = 0$. This equation defines the shifts in Fermi energy given applied probe voltage, gate voltage, and magnetic field. As in the prior case, there will be imperfections in the sample that cause resonances, these resonances will provide contrast in the conductance, and tracking their shapes in 2D maps of two parameters can provide a more robust measure of the parameters of the system than can the tunneling conductance curves themselves. Now I will look at the various solutions to this equation.

4.4.1 Constant field

With a constant field the equations to solve look very much like those in zero field, with the same solution for constant μ:

$$C_p deV_p + C_g deV_g = 0 \quad \rightarrow \quad \frac{dV_g}{dV_p} = -\frac{C_p}{C_g} \tag{40}$$

and constant energy $\mu + eV_p$

$$-C_g deV_p + C_g deV_g = e^2 g(\mu, B) deV_p \qquad \rightarrow \qquad \frac{dV_g}{dV_p} = 1 + \frac{C_Q}{C_g} \tag{41}$$

The major difference is that $g(\epsilon, B)$ and thus C_Q differs from the field free density of states, and the initial qualitative picture of conductance maps for constant field is correct.

4.4.2 Constant gate voltage

At constant gate or constant bias, there is a slightly different map, since either parameter will now be graphed against the field. It still makes sense to look at constant Fermi level and constant energy, but the Landau level index is a simpler quantity to look at, as the Fermi level can be a rather complex function of gate voltage, probe voltage, and field. Note that the two are not the same since the Fermi level for a given index will change with magnetic field. So lines of constant Landau index are represented by:

$$\frac{dB}{dV_p} = -\frac{C_p}{\frac{-2e^2 i_F}{\pi\hbar} + (C_p + C_g) v_F sgn(i_F)\sqrt{\frac{\hbar|i_F|}{2eB}}} \tag{42}$$

In this case, it is easier to write the constant energy constraint in terms of the variables rather than slopes:

$$E = v_F sgn(i_F)\sqrt{2e\hbar B|i_F|} + eV_p \tag{43}$$

$$\rightarrow \quad B = \frac{(E - eV_p)^2}{2ev_F^2\hbar|i_F|} \tag{44}$$

So Eq. 42 says that there will be lines that follow a roughly constant slope that is given by the Fermi velocity, Landau index, and probe capacitance. There is a slight correction given by the potential shift adding a small curvature to otherwise straight lines that becomes less significant at higher fields. The constant energy lines traces out parabolas, as seen in Eq. 44. Since the Landau level index is allowed to change with the probe voltage, the parabolas will occasionally be disrupted whenever a constant energy line crosses a constant index line. When this happens, the parabola will change it's curvature to the one appropriate for the new Landau index.

4.4.3 Constant probe voltage

When the probe voltage is held constant, there is a very similar equation for the constant index lines, with the role of gate and probe reversed.

$$\frac{dB}{dV_g} = -\frac{C_g}{\frac{-2e^2 i_F}{\pi\hbar} + (C_p + C_g)v_F sgn(i_F)\sqrt{\frac{\hbar|i_F|}{2eB}}} \tag{45}$$

The constant energy condition boils down to a constant Fermi level condition for a constant probe voltage, so that $\mu_F = v_F sgn(i_F)\sqrt{2e\hbar B|i_F|} = constant$. This means that the constant energy lines follow:

$$B = \frac{(E - eV_p)^2}{2v_F^2 e\hbar|i_F|} \tag{46}$$

There appears to be no new information in such diagrams compared to the prior two cuts, except for an independent measurement of the gate capacitance, and thus I did not take a large number of these scans.

Over all, the theory demonstrates a much more complex structure than the original theory in zero magnetic field. Fortunately, many major parameters of the junction may be evaluated despite a distributed, disordered system. The probe capacitance, gate capacitance, and Landau indices may all be determined by these measurements, and may prove to be valuable in the evaluation of material effects on graphene, as well as measures in quality of gated devices. It should again be stated that the fact that information pertaining directly to the area of the graphene in proximity to a gate is more valuable than some other techniques, as a very sensitive probe of the disorder present.

Also, with the magnetic field, as I alluded to before, there is one more parameter that can be measured in this system that while relatively simple, is arguably of greater fundamental interest. This is the capacitance between a localized state and an extended state when a sample is nearing the Quantum Hall regime.

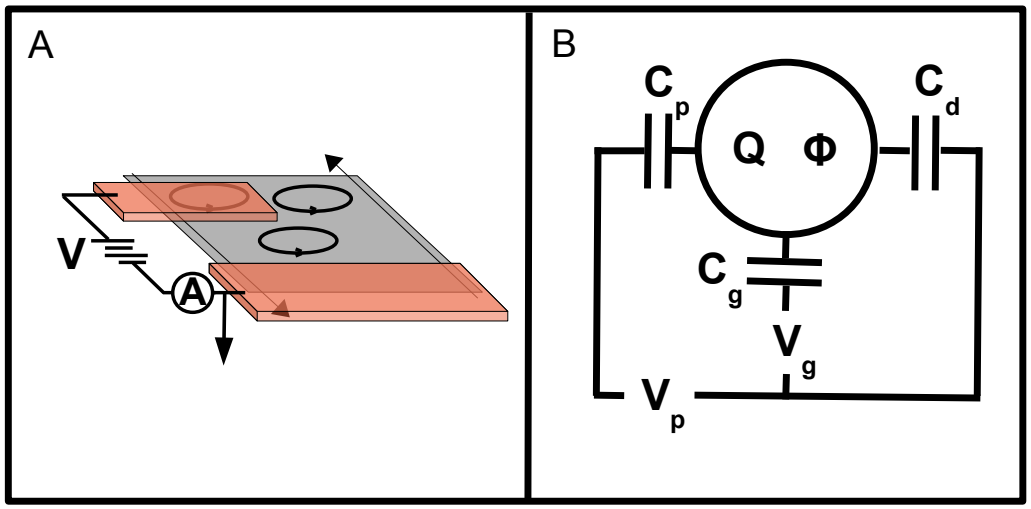

Figure 4.2: A: A cartoon of the device, including the localized Landau orbits that act as the isolated island in the double barrier system. B: A schematic of a quantum dot capacitively coupled to a source and drain lead as well as a gate electrode.

4.5 Experimental results

I begin by pointing out one junction in particular; however, the primary results presented here were observed in two other devices that displayed tunneling properties. Fig. 4.1-A & B shows an optical image of the completed device both before and after exposure to HNO_3. Many of the other probes on this device did not become highly resistive after the short exposure to HNO_3. In the present case the junction was only partially overlapping the sample, and in two other cases the junction was entirely overlapping. All measurements presented here were taken while the sample was in vacuum in a cryostat operated at or below 4.2 K, and equipped with a 12T superconducting magnet. Tunnel spectra were gathered by applying a DC probe voltage, V_p, across a highly resistive and an ohmic probe, and a gate voltage, V_g, between the Si back gate and an ohmic probe, and measuring the current as shown in Fig. 4.2-A. A numerical derivative was then taken to calculate the conductance.

The data consists of mapping the conductance with V_g and V_p at different magnetic fields, as well as some conductance maps vs. B and V_p. Fig. 4.3 displays conductance

maps at 0, 3, 6, 9, and 12T, as well as a conductance map with a constant 0 V on the back gate. The tunnel spectra are dominated by the gate voltage independent zero bias anomaly (ZBA), similar to other tunneling experiments. [50, 37] As explained earlier in this chapter the data can be analyzed despite the ZBA by inspecting how tunnel resonances in the spectra shift with V_g. Those features that shift with gate voltage are related to the graphene DOS, and their slope is directly proportional to the DOS at the Fermi energy $E_F(V_p, V_g)$, [55] where $E_F(V_p, V_g)$ is the Fermi level in graphene. By applying a gate or probe voltage, charge is added to or subtracted from the graphene. In regions of high DOS, the added charge does not shift the Fermi level much, whereas in regions of low DOS, the added charge shifts the resonance quickly.

Looking at Fig. 4.3-A, lines of high conductance can be seen at 0T. These are resonances in the DOS caused by the disorder potential, and become slightly flatter at positive gate voltage, where the density of states is lower. This I interpret as a broadened Dirac point, and it's location at positive gate voltage means the graphene is hole doped. As the magnetic field is increased, these lines are seen to break up, and are replaced by lines with a staircase like structure of alternating high and low sloped lines. I identify these lines as the formation of Landau levels.

To compare the conductance maps with those expected from perfect graphene I numerically calculate the tunneling conductance assuming constant transmission for states between the Fermi level and the probe voltage for given magnetic field, probe, and gate voltages. Using the theory described earlier, I arrive at Fig. 4.4-C by applying a 2.5meV lorentzian broadening function. A staircase structure where the gate voltage is unable to shift features in the spectra until the highly degenerate Landau levels are filled, and the spectra are quickly shifted when the DOS is low.

The simulation of a B vs. V_p map shows that the expected parabolic lines are disrupted by shifts in the Fermi level caused by the tunnel probe. I show for comparison data taken from the tunnel probe that shows similar behavior (Fig. 4.4-B), at at

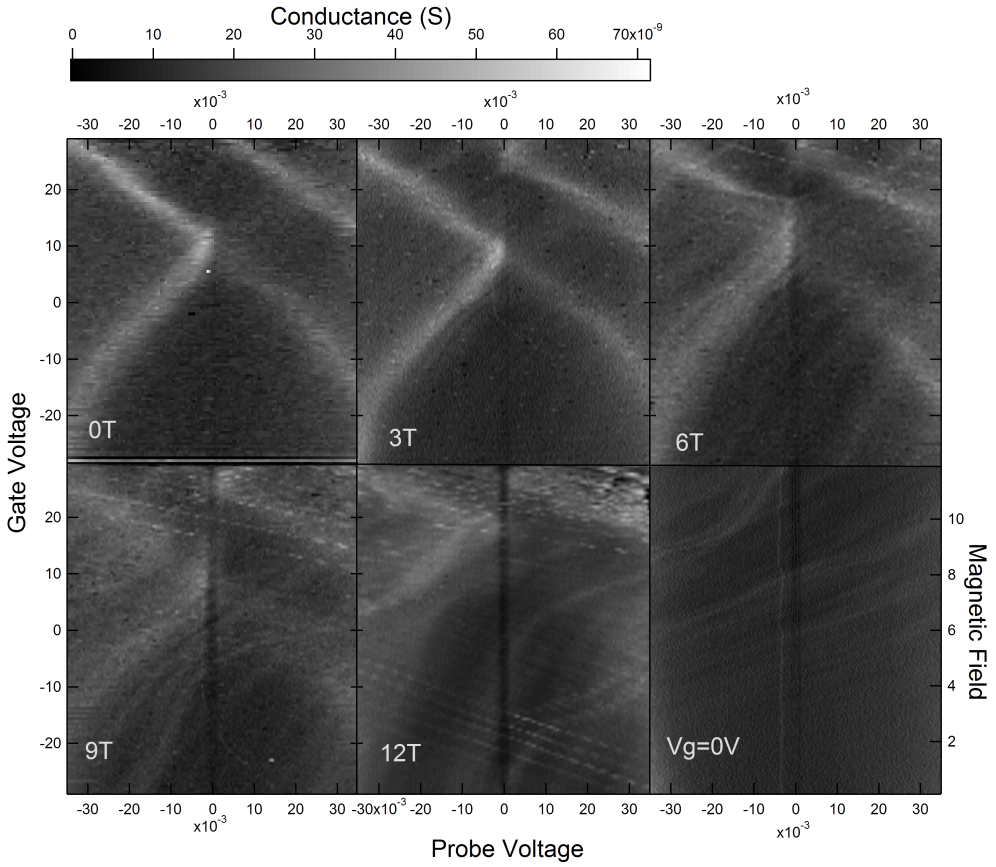

Figure 4.3: A progression of conductance vs. probe and gate voltage maps with magnetic field for CuB-1. At 0T, the disorder induced resonances can be seen, and break up into Landau levels at high fields. Already by 6T, the sharp resonances can be seen to emerge near 30 V, and by 12 T, a second set appears near -20 V on the back gate. Also shown is a map of conductance vs. probe voltage and magnetic field while the back gate is held at a constant 0V.

$V_g = -40V$, far removed from the Dirac point.

An important observation of this paper is the sharp resonances that begin to appear in the upper portion of the 6T map as seen in Fig. 4.3-B, and become very well resolved, with the lowest resonance appearing at $V_g = -20V$ and $V_p = 0mV$ at 12T in Fig. 4.3-D. I interpret these resonances to be due to single electron charging effects near the filling of Landau levels. In the progression from Fig. 4.3-B-D, the set of sharp resonances where the lowest resonance appears near +25V do not appear to shift, whereas the second set of resonances is seen to shift from near 0V in Fig. 4.3-C to ∼-20V in Fig. 4.3-D. This, combined with its clear appearance before any other level, leads us to the conclusion that the Dirac point is near +25V, and that these resonances are associated with the n=0 Landau level. The other set of resonances that show near -20V at 12T would therefore be the n= -1 Landau level. The bright, high conductance, positive sloping lines at -20V are steep when they intersect with the resonance lines. This suggests that the resonances form when the Landau level is pinned (while the level is filling).

The gate voltage spacing is much larger than expected if these are in fact the n=0 and n=-1 levels. The spacing between the bottom resonance of the n=-1, and the bottom resonance of the n=0 is ∼45 V, when 16 V is expected at 12T. As can be seen by Fig. 4.4-C, the spacing in gate voltage between the various Landau Levels is uneven in the presence of a strongly capacitive tunneling probe. When the back gate electrode is brought to a large enough potential to induce the amount of charge in a Landau level ($-2e^2B/\pi\hbar$), to shift the Fermi level from n=-1 to n=0, the graphene shifts its electric potential to keep the electrochemical potential constant ($e\phi = -v_F\sqrt{2|e|\hbar B}$ in the case of n=-1 → n=0). This causes the tunnel probe to induce a charge $C_p\phi$ on the graphene, and the gate electrode must add an additional C_gV_g of charge to counteract this. Thus, the expected shift is 47 V for this sample, rather than 16 V. The resonances near 0V in Fig. 4.3-C are not well developed enough to accurately

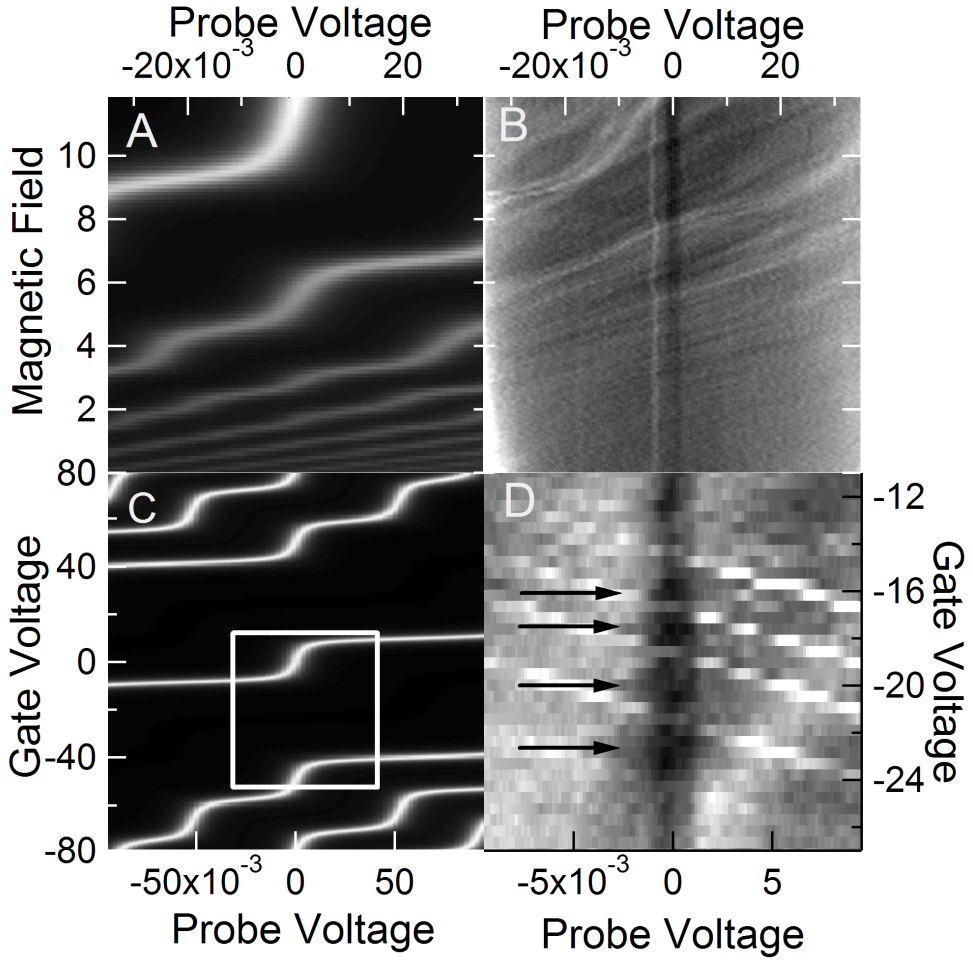

Figure 4.4: A: A simulation of a conductance map vs. V_p and B assuming undoped graphene and -35 V on the back gate. B: Data taken at 0V gate voltage in Sample CuB-1. C: A simulation of a V_p vs V_g map, showing the staircase structure of the Landau levels at 12T, a box denotes the approximate range of at least one of the conductance channels measured in the data. D: Arrows mark the Coulomb diamonds at 12T.

measure their position.

At some combinations of magnetic field, gate voltage and bias, new lines appear in the conductance map that have approximately the same slope as the negative sloping lines that denote lines of constant Fermi energy, and form diamonds with the set of positive sloping lines of constant energy near zero bias voltage, as well as near the beginning or end of a Landau level being filled. What is surprising is the sharpness of some of these lines. The resonances described earlier at zero field, and even many at higher fields are on the order of $10meV$ in width. The resonances under discussion however are on the order of kT. This is a strong indication that the energies probed are due to a dot that has been electrically isolated from other sources of charge, since coupling to leads broadens sharp energy levels.

I propose that in addition to the tunneling barrier between the probe and the graphene, there also exists a barrier between a localized dot and an extended state within the graphene. The calculation of a capacitance should be possible between such structures, but I also open up the possibility that such information could probe some fundamental aspects of the Quantum Hall Effect.

One might ask how exactly the tunneling probe can come into contact with just one localized state. One obvious answer is that it doesn't, and that the measured conductance is several states in parallel, since the states that have a low resistance path to the grounding electrode should be more likely to be better represented. On the other hand, since the tunneling resistance is exponential with distance, and the Landau levels of graphene can be extremely large (25nm at 10T), it is not unreasonable that only a few states are participating in tunneling, and if the tunneling resistance between the probe and graphene is similar to that of the tunneling resistance between the localized and extended state, then there is much less advantage to tunneling straight into an extended state. In addition, as the magnetic field increases, the disorder potential is less able to disrupt the formation of Landau levels, and the

number of localized compared to extended states increases, increasing the likelihood of the observation of single electron tunneling.

The resonances can be explained by the theory of Coulomb blockade, as explained in the introduction. When a conductor becomes extremely small and isolated from charge reservoirs, the charging energy to add a single electron becomes non-trivial, and an electron can only tunnel onto a central island if sufficient voltage is applied. [25] In the present case, a localized state within a Landau level becomes the central island, tunnel coupled to both the metal lead and an extended state within the graphene that in turn couples to the grounding electrode. Such samples exhibit sudden onsets of conductance along the sides of a Coulomb diamond.

A closer inspection of Fig. 4.4-D reveals that there is a group of four lines, and the resonances are spaced by approximately 10meV. The appearance of four diamonds suggests splitting of the spin and valley degeneracies, but the fact that the spacing is larger than the expected Zeeman (1.4meV) or valley splitting (negligible) in the 1st Landau level of graphene, indicates that the charging energy dominates these spacings.

From orthodox theory of single electron tunneling, [25] the slope of the resonances is $-C_p/C_g$. The spacing between the negative sloping lines, measured parallel to the probe voltage axis, is e/C_p, assuming the energy level spacing due to Zeeman and the valley degeneracy splitting much smaller than the charging energy. Thus, I obtain $C_p = 16aF$. Assuming a gate capacitance per unit area of $124\mu F/m^2$ as measured on a test wafer from the same batch of oxidized Si wafers, this leads to a radius of the localized state of 13nm. The magnetic length of graphene at 12T is 7.4nm [57], suggesting that tunneling could indeed be occurring through a single localized Landau level. I note that the resonances located near +25V gate voltage have a larger spacing ($\sim$15meV).

This data is to be compared with, [50] in that work, the Landau levels are

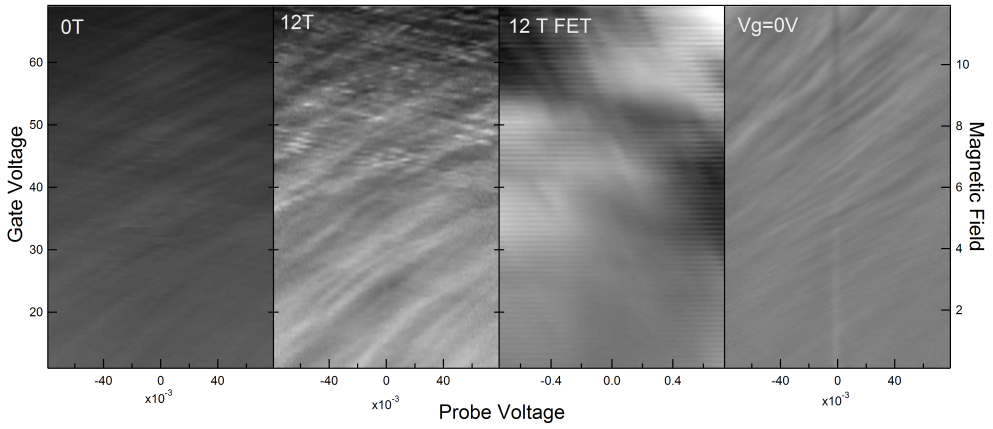

Figure 4.5: A sequence of conductance maps in CuB-2. The emergence of regions of lower DOS can be seen as well as sharpening negative sloping lines. The third panel displays data taken by placing Cu-2 in the FET configuration, at 12T, weak plateaus can be seen after subtracting a smooth background. The fourth panel is the constant gate map at 0V (below the Dirac point). All voltages are given in volts.

identified as a staircase structure in the conductance maps, and at high fields, sharp resonances are seen to emerge at the filling and emptying of Landau Levels. It was suggested that the larger energy spacing near the zero Landau level was due to a lifted valley degeneracy, adding 10meV at 8T to the charging energy in the n=0 Landau level. The staircase structure has recently also been observed in ref. [42].

As mentioned before, similar observations were in fact made in two other samples. Fig. 4.5 displays a sample in a higher resistance junction and larger positive doping. The step structure at 12T is not as dramatic as the first sample, however there is a visible alteration. The zero field image has softly curving lines with a constant curvature, while the 12T image adds some amount of waviness. Also, the sharp resonances are clearly visible at 12T. Since the capacitance ratio is much smaller than the first sample $\sim$ 50, the spacing is much closer to 15V, although it is not entirely clear where to measure.

The conductance map vs. B and V_p at 0 V also reveals the higher doping. Since there is little flattening in the parabolic lines, the map is taken far from the Dirac

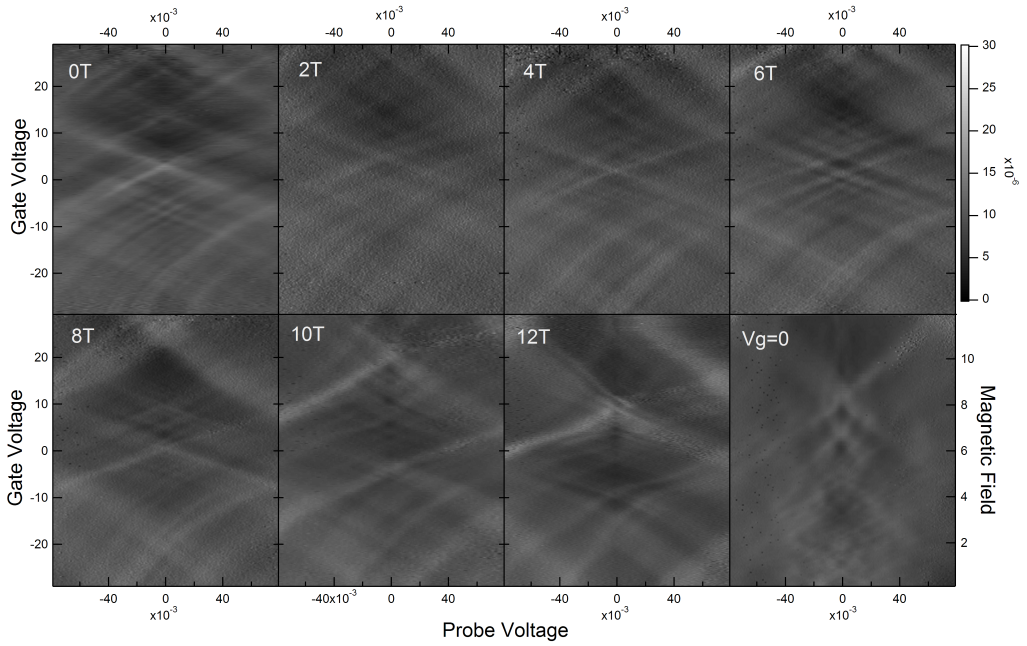

Figure 4.6: The conductance map at 0T and 12T for sample CuB-3 that clearly displays the sharp negative sloping sharp lines observed in Cu-1, the conductance between the source and drain after a low frequency background has been subtracted, and the constant gate map at a voltage for below the Dirac point.

point. An interesting point in this sample is that it was possible to carry out a double gate experiment similar to those explained in the previous chapter. After subtracting a background resistance, a series of diamonds can be seen at high field. Both implying the p-doping and the existence of the quantum Hall effect underneath the contact.

Finally, a third sample, though perhaps not as high quality as the first discussed, also shows a clear flattening of the energy resonances in high field. The group of four charging resonances can be observed at high magnetic field, but only barely, this combined with the fact that the parabolas in the conductance map vs B and V_p are almost completely obscured imply that the Landau levels in this sample are much broader than in the other junctions studied here. However, this sample does provide an excellent view of a Landau level actually shifting as the field is increased, the 6, 8, 10, and 12T scans clearly track a level as it shifts from 30 V to 10 V. Another interesting point is that several impurity resonances at 0T completely disappear at

high field, most notably the one that crosses $V_p = 0$ at $V_g = 15$.

In conclusion, transport through graphene tunnel junctions in a high magnetic field demonstrates localized states in the quantum Hall regime. The direct probing of a localized state in a Landau level is both important as confirmation of earlier experiments, and a new way to study Landau level physics in condensed matter.

CHAPTER V

DIRECT METAL CONTACTS TO GRAPHENE

5.1 Introduction

Though my tunneling studies answer many questions about the interaction between graphene and a metal, there is still a question of the role of a truly clean contact between graphene and a metal. In search of this, I attempted both annealing metals after electrical contacts were defined by e-beam lithography, and depositing metals at high temperatures to completely avoid resist residues.

5.2 Contact resistance

The parameter of scientific and technological interest when attempting to make a clean contact to graphene, is the contact resistivity per unit area. Since graphene is atomically thin, it is difficult to measure the contact resistivity directly without also including some of the sheet resistance of graphene. If the resistances are high, as with the tunnel junctions already presented, the voltage drop occurs exclusively across the contact, and there is no problem. As the resistance becomes lower, the current is not uniformly distributed throughout the contact, and an electron may diffuse into and out of the metal many times before leaving the contact area.

I will therefore illustrate here a successful model for metal-semiconductor contacts, the Transfer Length Method, [58] since it is both relevant to at least highly doped graphene, as well as used in several publications [59, 60, 61]. This model is similar to the telegraph model of a resistance and inductance in series and a conductance and capacitance in parallel with a grounding electrode. The inductance and capacitance are set to zero as shown in Fig. 5.1-A, and lead to the set of differential equations

$$\frac{dV(x)}{dx} = -\frac{W}{R_{ch}}I(x) \quad (47)$$

$$\frac{dI(x)}{dx} = -\frac{\rho_C}{W}V(x). \quad (48)$$

The solution to these equations is

$$V(x) = V_0 cosh\left(\frac{x}{L_T}\right) - I_0 Z sinh\left(\frac{x}{L_T}\right) \quad (49)$$

$$I(x) = I_0 cosh\left(\frac{x}{L_T}\right) - \frac{V_0}{Z} sinh\left(\frac{x}{L_T}\right) \quad (50)$$

where ρ_C is the contact resistivity, R_S is the sheet resistance (of the region beneath the contact), $Z = \sqrt{\rho_C R_S}/w$ is the characteristic impedance, and $L_T = \sqrt{\rho_C/R_S}$ is the transfer length. An actual measurement often takes the form of Fig. 5.1-B where transistors with similar contacts, but differing channel lengths are measured. If the contacts and channels have relatively uniform properties, then a straight line is formed in a graph of two probe resistance vs. channel length, and extrapolates to $2R_c$ at zero channel length, and $-2L_T$ at zero resistance.

From the solutions to the transmission line equations above, $R_C = V(0)/I(0)|_{I(d)=0} = Z\coth(d/L_T)$, relating the measured R_C to the microscopic parameter of interest, ρ_C. Another measurement is the contact end resistance or the three probe resistance $R_e = R_{3probe} = V(d)/I(0)|_{I(d)=0} = Z/\sinh(d/L_T)$. One more useful relation is the resistance under a probe that has been left floating so $R_{float} = (V(0) - V(d))/I(0)|_{I(d)=I(0)} = 2Z(\cosh(d/L_T) - 1)/\sinh(d/L_T)$.

Let's briefly check the limits of these solutions to make sure that they make sense. If the contact resistance is high, the contact should act very similarly to a vertical one, since most of the voltage should drop across the junction, rather than the conductor. For similar reasons, current passing under a floating contact should stay in the conductor rather than enter and exit the contact. In this case, $\rho_C >> R_S$ and I can

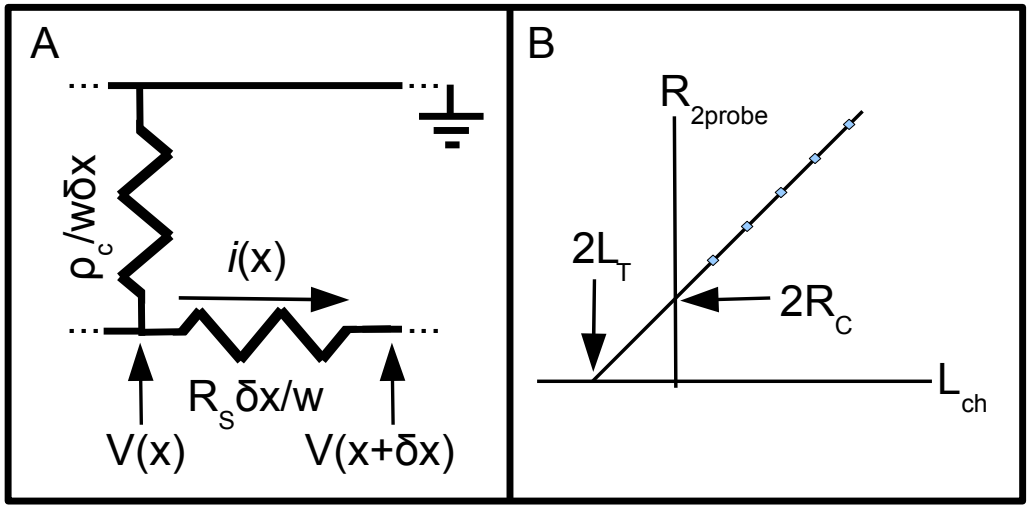

Figure 5.1: A: The model used to analyze contact resistance. The contact is made up of distributed resistors based on a homogeneous contact resistivity and sheet resistance. B: A TLM measurement to extract R_C and L_T.

easily fabricate leads such that $L_T >> d$, so $R_C = R_e = Z(L_T/d) = \rho_C/(dw)$, and the resistance of a floating contact is $R_{float} = R_S d/w$. On the other hand, if the contact resistance is very small, I expect most of the current to flow through the edge of the contact, so that the two and three probe resistances will be very different. Similarly, a current should flow almost exclusively through the floating contact, experiencing the characteristic impedance as it enters and exits the contact. In this case, it is easier to make $d >> L_T$ so $R_C = Z$, $R_e = 2Ze^{-d/L_T}$, and $R_{float} = 2Z$.

The difficulty arises because there is a mismatch between the quantities measured in the experiment, and those needed to plug into the theory, even for the ideal measurement just described. First, the R_S measured is for the channel region, and not the contact region. Because of charge transfer near the leads, these two values may differ significantly, and I will differentiate this by calling the channel sheet resistance R'_S. The R_C measured is correct, since even if the channel resistance is different than the contact sheet resistance, the line in Fig. 5.1-B will still extrapolate to the same value. L_T is incorrect, because this is the value where $R'_S L_T/w = R_C$, so if $R'_S = R_S$

then $L_T = \sqrt{\rho_C/R_S}$ as stated earlier; however, in the case where $R'_S \neq R_S$ then $L_T = \sqrt{\rho_C R_S/R'^2_S}$.

Therefore the correct method may actually be to measure both the three probe resistance and the two probe resistance. If $d << L_T$, then $R_e = R_C = ZL_T/d = \rho_C/dw$, and the two resistances will match. Furthermore, the measured contact resistance will in fact be geometrically related to the desired contact resistivity.

5.3 Vacuum annealed Cu contacts

One way to attempt a cleaner metal contact is to use normal e-beam lithography, and thermally anneal the devices in the hopes that some of the PMMA residue will escape the contact region, or the metal will diffuse into cleaner areas. In this experiment I use Cu, and mechanical exfoliation is used to deposit graphene onto the surface of an oxidized silicon wafer. [20] Single graphene layers are identified using an optical microscope, and authenticated via Raman spectroscopy. [27] The devices were created by two e-beam lithography processes. The first was used to define a Poly(methyl methacrylate) (PMMA) mask to protect the graphene from an O_2 plasma to create well defined rectangular strips. All remaining PMMA is removed using Acetone. In the second process, I use a methacrylic acid/PMMA bilayer of resist and define exposed regions for metal contacts. The leads of sample B were slightly underdeveloped, leaving additional resist residue on the contact area to increase the level of contamination. The sample is then transferred to a thermal evaporator, and pumped down to 10^{-7} torr. At this point, approximately 35nm of Cu are deposited onto the sample, followed by lift-off in acetone.

Each pattern is designed with many rectangular leads that entirely overlap the sample. Each lead was 3 μm wide in Sample A, and 2 μm in Sample B, while the channel length was varied between 1 and 6 μm in approximately 1μm increments, similar to the devices found in Ref. [59]. The contact resistances were evaluated

on a probe station in ambient conditions and room temperature by measuring the pairs of adjacent contacts on each sample, and then these resistances were plotted vs channel length and normalized by the width of the ribbon. The two probe resistance is given by the equation $R_{2probe} = 2R_c/w + (R_S/w)L_{ch}$ where R_c is the effective contact resistance, R_S is the square resistance of the graphene channel, L_{ch} is the channel length, and w is the width of the sample. The width of Sample A is 4.7μm and the width of sample B is .95μm.

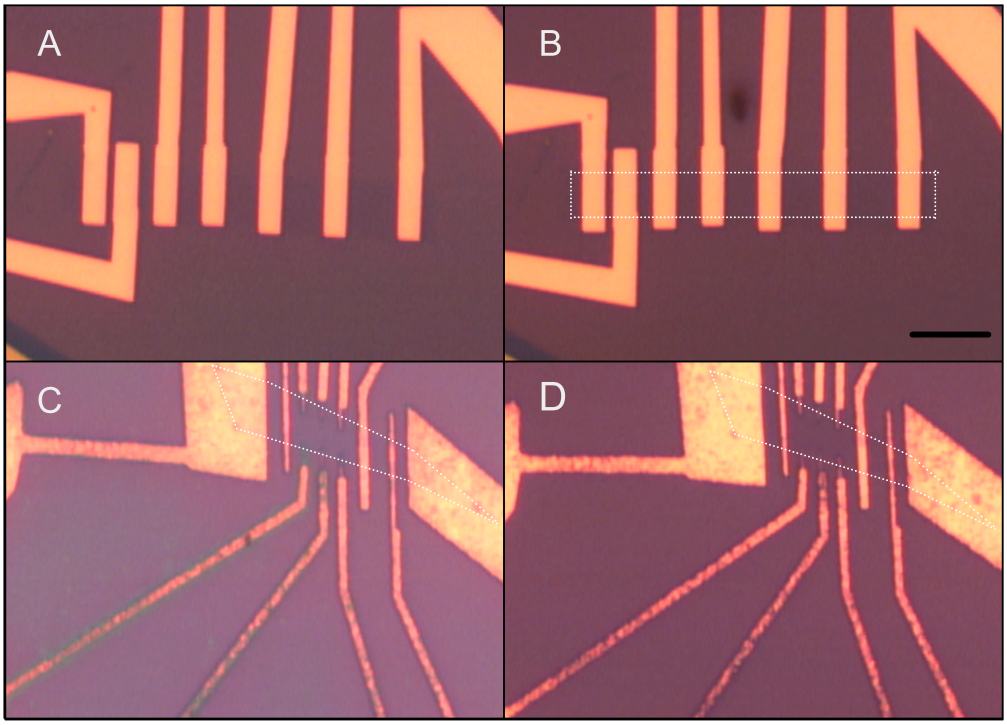

Figure 5.2: Sample A and Cu-1 before (A & C) and after (B & D) the 306°C, 12 hour anneal. There is no damage visible to the device from this treatment. The scale bar is 10μm.

The Cu contacts as deposited have relatively high contact resistances. To treat this problem I placed them inside a vacuum chamber, pumped down to 10^{-7} torr and annealed them for 12-15 hours. Sample A was annealed twice, once at 260°C,

and again at 306°C. The second sample was annealed only once at 300°C. Sample A, both before and after the anneal is shown in Fig. 5.2A & B. After annealing, the contact resistance in general decreases, even when the sample is heavily contaminated as in Sample B. Shorter times were tried with varying results. The extremely long bake time consistently improves the contact resistance. A method involving gentle O_2 plasma exposure in combination with a shorter, higher temperature anneal was recently explored in Ref. [60]. I find that the derived values for the contact resistivity compares favorably with their method for Cu contacts. Note that O_2 plasma is not used to clean the graphene surface from contamination in the technique presented here.

Fig. 5.3-A displays the line fits to the two probe resistances for Sample A. A clear improvement can be seen after the annealing process. Fig 5.3-B displays the line fit to the two probe resistances for Sample B. Due to the higher contamination of this sample the two probe resistances were hundreds of kΩs; however, the annealing process still repaired the leads. The extracted values of R_c, L_T, R_S, and ρ_c for both samples are displayed in Table 5.3.

Sample Cu-1 as discussed in the last chapter further demonstrates the effectiveness of annealing to repair imperfect graphene contacts. As discussed previously, it was dipped in dilute (12%) HNO_3 for several seconds. The leads were not fully oxidized by this process, and in fact most still made contact to the graphene via kΩ resistances. After several weeks in atmosphere, the contacts were all highly resistive (>MΩs), as seen in Fig. 5.2-C; however, an anneal such as the one described above returned the contacts to resistances on the order of kΩ, and some tarnishing visible before the anneal was no longer visible afterwards, as evidenced by Fig. 5.2-D. I do not have precise contact resistance values for this sample since its geometry was not designed for the types of measurements presented here.

Sample A was tested at low temperature to measure two probe resistance vs gate

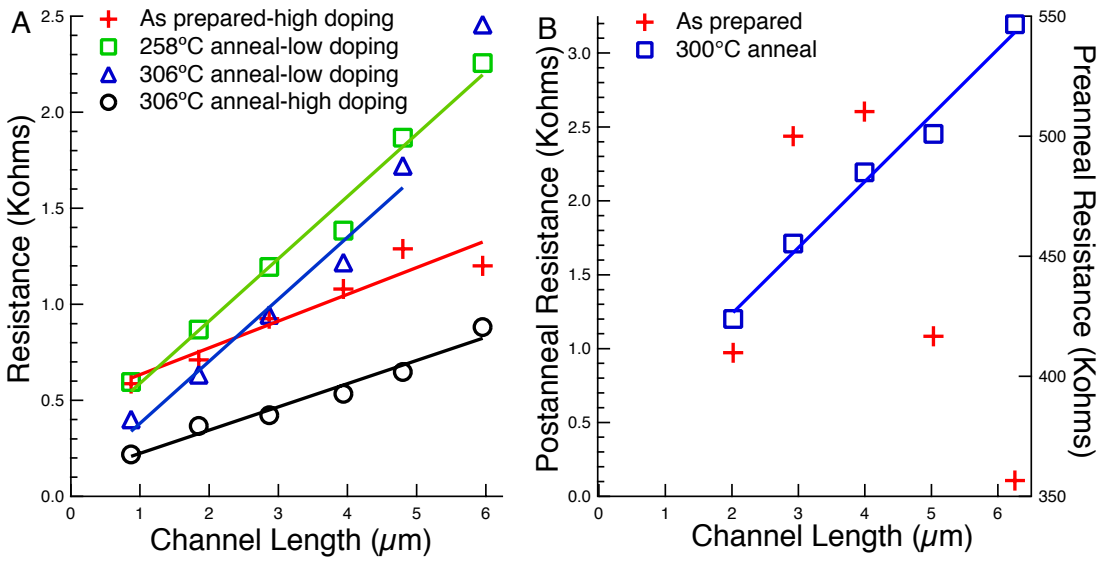

Figure 5.3: A: Sample A after several annealing cycles to the sample. Immediately after removal from the vacuum chamber, the TLM measurement displays a much larger uncertainty than after the channel has returned to a high doping value, after being exposed in air for >100 hours. The point for the longest channel length for the 306°C anneal at low doping is omitted from the fit, as it causes the effective contact resistance to become negative. B: Sample B, due to the additional contamination, the resistance is dominated by the contacts, and is unrelated to the channel length, however; the contact resistance decreases dramatically after vacuum annealing.

voltage for several channel lengths. The sample was annealed a third time to reduce environmental dopants on the graphene, and quickly transferred to a dipstick for measurement at 4K. Fig. 5.4-A shows that many of the channel regions are relatively uniform, but some are not. Even those that appear uniform show large variability when attempting to derive contact resistances near the Dirac point. Fig. 5.4-B & C show three probe resistances which are extremely small ($\sim 25\Omega$). This demonstrates that for these contacts d>> L_T.

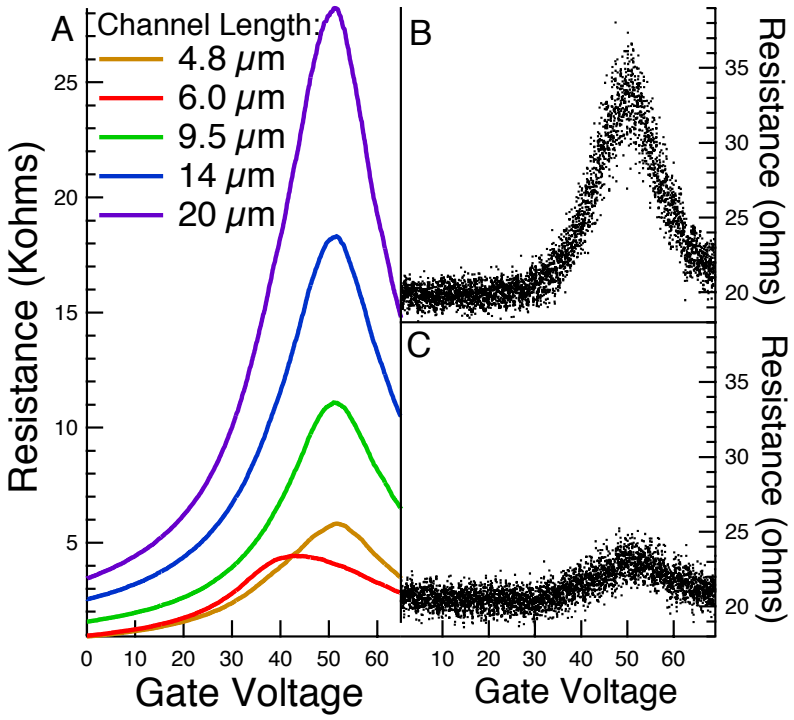

Figure 5.4: A: Gate voltage dependence at 4K for several graphene transistors on Sample A. The properties can be seen to be largely, but not perfectly, uniform. This adds uncertainties to the contact resistance measurements. Note that for some channel lengths shown the current passes beneath contacts that are allowed to float. B & C: 3 probe resistances for two different probes. The resistance is very small due to wide contacts, and practically flat except near the Dirac point. Since the BrPh electrical leads are $\sim 14\Omega$, the true three probe resistance is even smaller.

Table 1: Measured values of R_c and R_S, along with derived values of L_T and ρ_c

Sample	$R_c(\Omega\mu m)$	$L_T(\mu m)$	$R_S(\Omega/\square)$	$\rho_c(\Omega\mu m^2)$
A - as prepared	1161	1.77	655	2058
A - 260°C anneal	620	0.407	1524	252
A - 306°C anneal				
high doping	241	0.424	568	102
low doping	135	0.089	1516	12.0
B - as prepared	1.75e6	N/A	N/A	5.26e6
B - 300°C anneal	163	0.384	425	213

In conclusion I present a method to significantly improve the contact resistance between graphene and Cu. Though the technique presented here requires long annealing times and high vacuum, there is no reason to believe that the use of flash annealing, or other high temperature methods may not significantly decrease the time necessary to anneal the contacts. I also find that the annealing process has the ability to improve contact resistance even in the presence of large degrees of contamination.

5.4 Au islands evaporated at high temperatures

In order to completely avoid resist residues in the fabrication process, a more novel form of fabrication had to be developed: evaporating gold islands onto the graphene at high temperatures and high vacuum. By depositing at high temperatures two things are accomplished, first I sought to keep the graphene free from impurities while the metal interface is formed. Second, it is possible to evaporate relatively thick films (and therefore large islands) that are not electrically conductive even on the silicon surface. Thus it is possible to attach electrical leads to a piece of graphene treated in this way without shorting all the signal through the Au film.

Crystal growth at high temperature is a complex process with several regimes of growth identified. Since both Au and graphene are highly inert, the surface mobility is quite large, and newly arrived atoms at the surface would much rather stick to other gold atoms than on graphene. This type of growth is known as 3D non-wetting

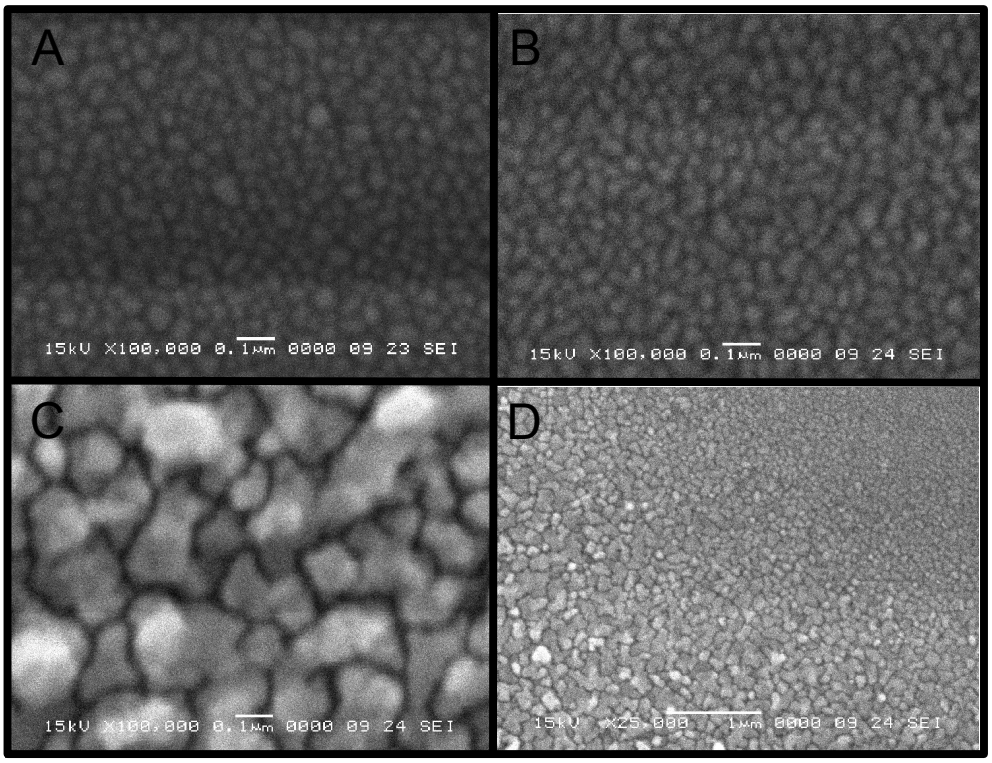

Figure 5.5: A: 300° and 10nm of gold evaporated on Si B: 450°C and 10nm of gold evaporated on Si. C: 300°C and 30nm of gold evaporated on Si. D: A region near the clip that secured the 300°C sample to the substrate heater, giving a demonstration of the mechanism of island formation as thickness is increased between zero and 30nm.

growth. [62] Films grown in this way have extremely low adhesion, and are non-conductive for much larger thicknesses than films grown at room temperature.

I constructed a simple evaporator compatible heater stage from a single 100W lightbulb filament, whose current was adjusted with a variac. The goal was to heat the sample for long periods of time without also heating the rest of the evaporator, causing damage and increasing the cool down time. Thus, an enclosed, reflective space was constructed from copper and heavy-duty aluminum foil. Stainless steel pillars supported the copper sample stage, providing moderate thermal isolation from the rest of the evaporator. The maximum temperature possible is found by solving the heat transport equations so that $T_{max} = \frac{P}{\kappa}$. Where P is the power supplied to the

heating element, and κ is the thermal conductivity to the heat sink.

Thus the weaker the thermal link, the lower the power necessary to reach high temperatures, at the cost of longer cool down times. Vacuum tight tubes that can flow air and water through the sample stage, thus providing cooling inside the evaporator, to shorten the cooling process. The best use of these is to run dry air through the tubes during the entire heating procedure. This way, the larger stage does not significantly increase in temperature, since heat is constantly being carried away, and the sample temperature will have greater stability. In this way, I have kept a sample at 300°C for over 12 hours with only a degree temperature rise. The temperature is measured using a K-type thermocouple, and is read with a Fluke multimeter that is calibrated for K-type readings. I have also checked that these correctly read the temperature of boiling DI water, and liquid nitrogen, as well as room temperature.

I also tried the procedure on epitaxial graphene seen in Fig. 5.6 A & B, which decorates defects near the surface and demonstrates the exceptional flatness, resembling growth on exfoliated graphite in the lower left hand corner of Fig. 5.6-C rather than the exfoliated graphene seen in Fig. 5.6-D. This is also a demonstration of the importance of having good quality samples to image for SEM. Having a good SEM is only half of taking a decent image, the other half is having a high-contrast sample (like gold on graphite) that is relatively free of contamination. Gold standards for the SEM will accumulate contamination remarkably quickly, and must be cleaned or replaced periodically. A substrate heater is valuable to produce replacement standards, as SEM accessory companies charge quite a bit for them.

The samples used here for transport measurement were mounted on a metal deposition stage and pumped to high vacuum (1.0×10^{-7}Torr), immediately after the exfoliation before any chemical processing. The samples are heated in high vacuum to 250°C for approximately 12 hours. After this bake-out, a Au film is deposited over the sample at ∼460°C at the rate of 1.0 Å/s, by thermal evaporation. The nominal

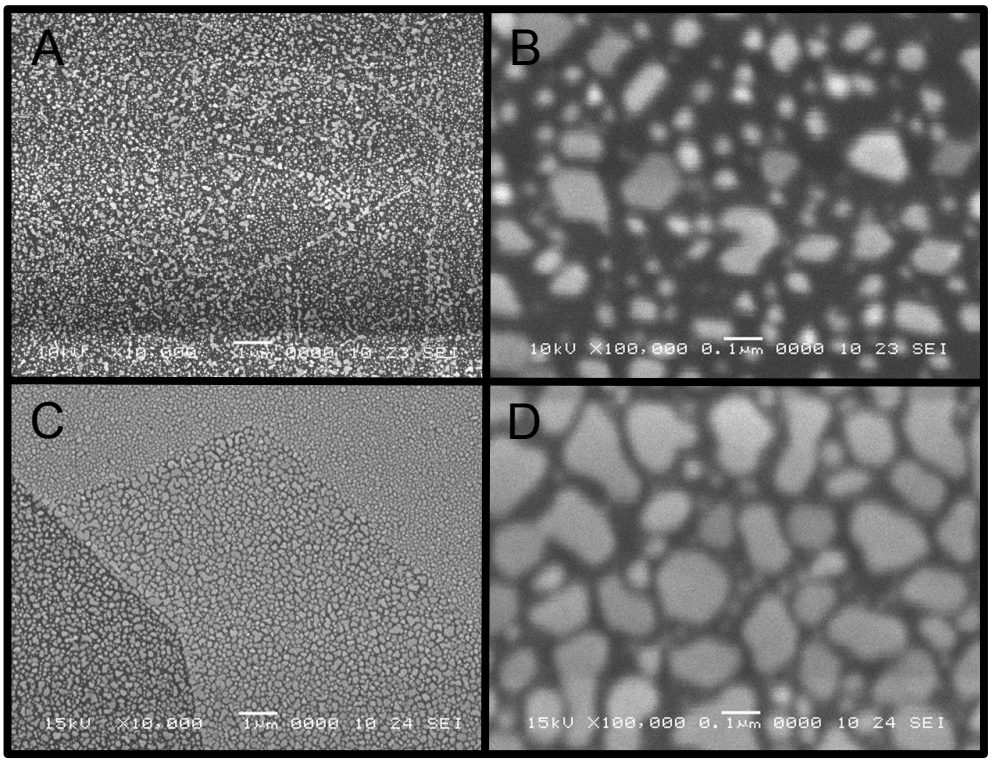

Figure 5.6: A: Au islands evaporated onto a substrate of epitaxially grown graphene, the growth can be seen to be dominated by defects due to the high surface mobility. B: A closer image of Au islands on EG, there are many faceted edges of the islands. C: Au islands evaporated onto graphene and a nearby graphite exfoliated flakes, The difference between growth on Si, graphene, and graphite can be clearly seen. Islands become larger and more widely spaced as surface mobility increases from the Si substrate to the disordered graphene, to the flatter graphite. D: Close up of Au islands on graphene, though not as faceted as the EG islands, many facets can be seen. Very few if any facets are observed in Au grown on a Si substrate.

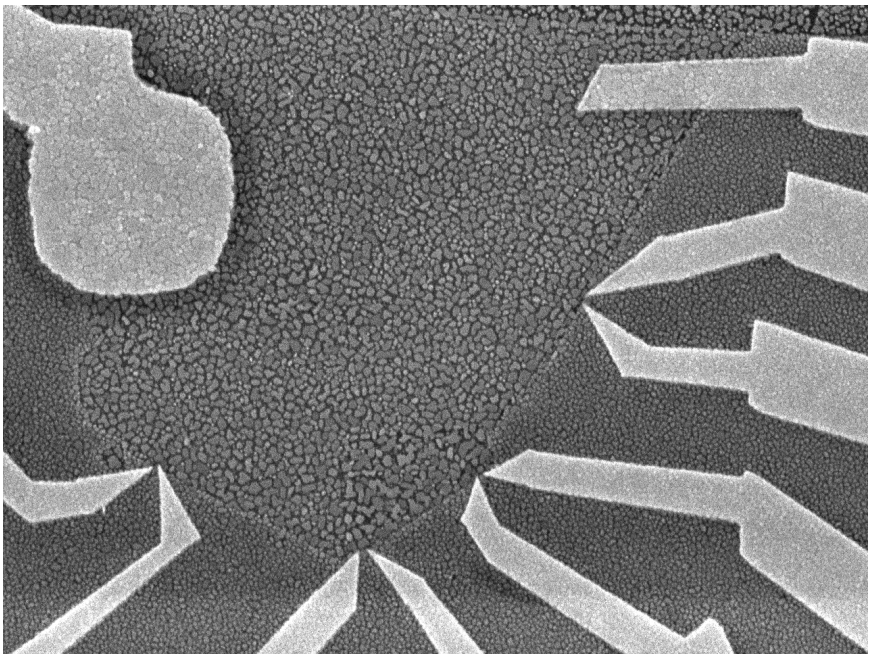

Figure 5.7: A sample with Au grains deposited on graphene at high temperatures. To create single grain contacts, locations of islands believed to overlap the grains are recorded by SEM, and then Cr/Au leads are deposited to make ohmic contact to the grains without touching the graphene. Large Cr/Au leads are deposited in order to make contact to the graphene directly.

Au film thickness is in the range 15nm-20nm. In some samples I made contacts to enable 4 probe conductance measurements, with no further attempt to align to the deposited Au grains. In some other samples, I made Cr/Au electric contacts to those single Au grains that overlap between the SiO_2 and the graphene substrate by e-beam lithography. There is no special trick to this, just careful, speedy alignment.

The first step in the alignment is to take an SEM image of the flake with deposited Au grains. The grid of alignment marks can be used to rotate the stage and achieve rotational alignment to with .1° by squaring a chosen section of the alignment grid with the borders of the computer screen. It is important to note several things about rotational alignment.

Aligning the rotation first is important, as the usual method of obtaining rotational alignment using multiple windows is too slow, and drift may be seen in the

final pattern. Also, .1° is actually quite good for most applications, for example, the maximum distance error caused by a rotation of θ and a length r between the alignment mark and pattern is $r\theta$. Thus for .1° and a $10\mu m$ Field of View there is a maximum error of 17nm, and that is smaller than the line spacing in the lithography software.

After the stage is aligned, the flake is registered to an alignment marker, and the grains have been imaged at x10,000 magnification, then the most accesible grains can be selected for contacts, and groupings of grains are chosen to be used for the alignment. The sample is spun with a MMA/PMMA bilayer (for a gentler lift-off process), and placed back in the SEM. Once again the stage is aligned to the grid of alignment marks, and the sample is coarse aligned at x1,000. Next a fine alignment at x5,000 or greater is done to find the Au islands chosen for alignment. As long as several grains were traced from the original image, it is always seems possible to unambiguously match the overlay to the image. Once the alignment overlay is placed on the grains, the window should be scanned a second time to adjust for any small movements that occurred while the grains were being searched for. After this, the pattern is written, with the critical features that touch the Au grains being written first, and within a few seconds of alignment. In this way, alignment with 50nm error is possible. A finished device with several pairs of leads is shown in Fig. 5.7.

5.5 DC bias dependence

As stated earlier, a strong electric field across a conductor can create a non-equilibrium distribution. The Boltzmann transport equations can be used to solve for the non-equilibrium distribution if the details of scattering processes are known. Alternatively, if information about the non-equilibrium function are known, then details of scattering processes may be inferred. Therefore, the study of DC bias dependence can reveal spectroscopic information, even if it is not as easily interpretable as that in tunnel

junction data. Adapting from Ref. [63], for a simple rectangular conductor with a bias V across the conductor the position dependent distribution function in the absence of any electron-electron scattering is a two step Fermi function

$$g(x,E) = \frac{1-x}{1+exp(E/k_BT)} + \frac{x}{1+exp((E+eV)/k_BT)}. \quad (51)$$

Since there is scattering in our system, the distribution function will have a more complicated form, but it can be seen in this equation that there are electrons with energy eV above the equilibrium Fermi level throughout the conductor. Thus by applying a bias to a large number of grains rather than a single grain, it may be possible to amplify at least some spectral information.

The earlier discussion of contact resistance also clearly shows that the information on contact resistivity is always included as part of the resistance when floating contacts are measured. So to understand what aspects of the data have to do with the contact resistance, I must first measure a clean sample with no Au grains.

Such a sample is shown in Fig. 5.8, and demonstrates the half integer QHE at a mobility of about 5000. In addition, weak localization can be observed at low fields. Fig. 5.8-B shows weak localization curves taken at a carrier density near the Dirac point at several different values of a DC voltage applied on the source and drain. It can clearly be seen that higher biases destroy the weak localization effect, as well as several other low field features of the data. This is because a DC bias acts on the system in a way similar to an effective temperature eV/k_B, spreading the electrons over a larger number of states than they inhabit in equilibrium. In all these experiments, the sample is directly immersed in liquid helium, and therefore the temperature like effects are caused by the non-equilibrium distribution, and not ohmic heating. The difference between a bias and a temperature is that a bias creates a much more complicated and spatially varying distribution than a temperature.

Prior measurements of the metal-graphene contact resistance show large variability; the fabrication, temperature, the metal used, and gate voltage seem to have an

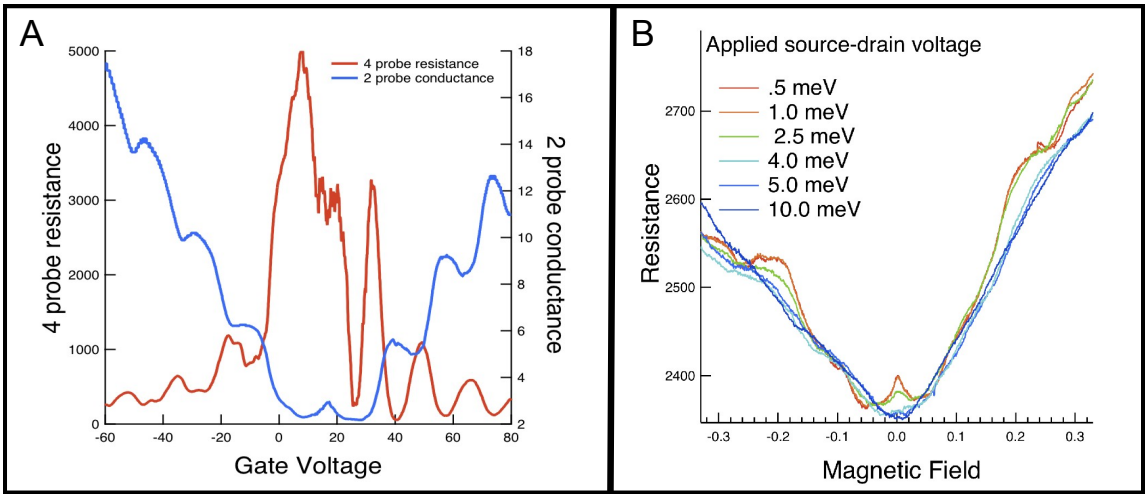

Figure 5.8: A: The 4 probe resistance (red) and 2 probe conductance (blue) of the Control sample at 12T, demonstrating the half integer quantum Hall effect in graphene. B: The weak localization peak at 0 gate voltage and several applied voltages. The peak can seen to be suppressed at higher electric fields.

effect on the contact resistance. [64, 65, 61, 34, 59] If lithography is involved between the exfoliation step and the metal deposition step, which appears to have been the case in the prior measurements, then polymer residue can be left in the contact, thereby changing the contact resistance. To eliminate the residue, the contacts in the samples are made without any lithography. The graphene between the grains makes channels with typical length L =35nm and width w =160nm that is within the range previously studied by theory. [32] The grain coverage, as well as the graphene channel dimensions L and w, are affected by the amount of deposited Au, as well as the precise temperature, and substrate interactions. I have studied in detail two samples for each grain coverage, the major results presented here were reproducible among those samples.

Fig. 5.10 A-C displays four probe bulk resistance versus gate voltage at 4.2K, in the control sample (Fig. 5.10-A); the sample with intermediate grain coverage (Fig. 5.10-B); and the sample with high grain coverage (Fig. 5.10-C). The resistance is measured by lock-in voltage detection, at the excitation current 100nA. As the

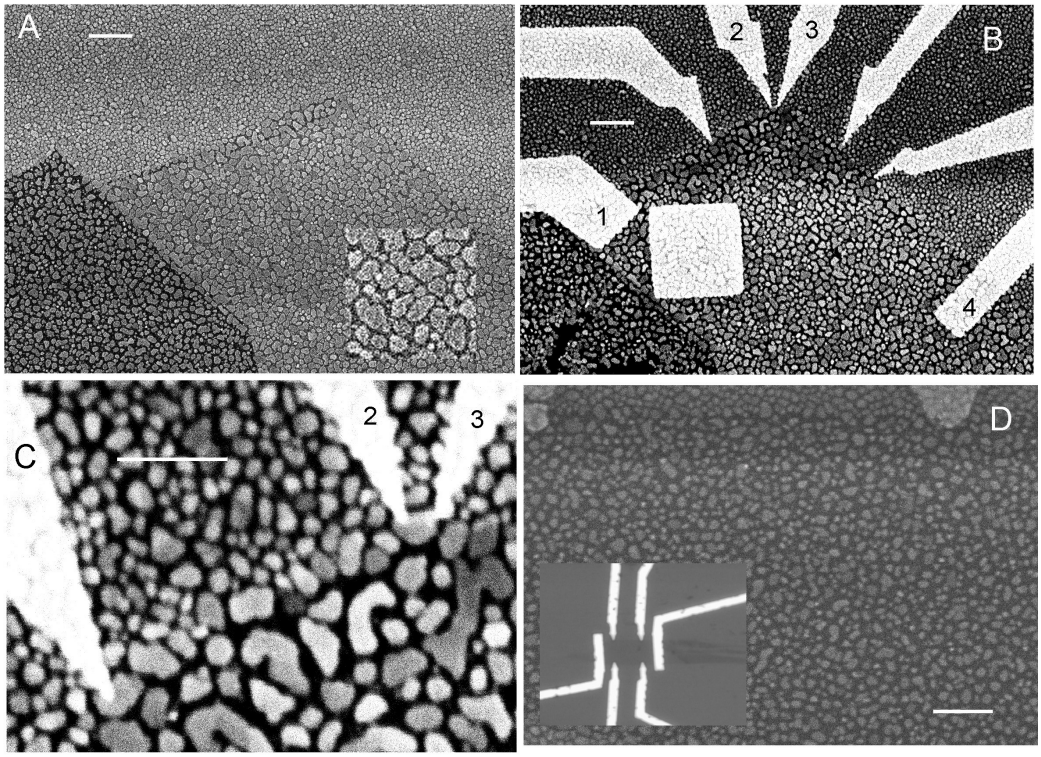

Figure 5.9: A: Sample showing an area of SiO_2 (upper), graphene (right), and graphite (left) with deposited Au islands, the inset shows a close up of the Au islands on graphene. B: Same sample with deposited leads, the window used for alignment can be seen in the lower left. Ina four probe contact measurement, current would be sourced between leads 1 and 2, and voltage would be measured between 3 and 4. This would eliminate the error caused by finite contact resistance between the leads and Au island, while introducing an error caused by finite current flow near the voltage measurement ground. C: Close up of the two leads touching a Au island. D: A different device with a different, and lower density of Au islands. Inset is an optical image of the graphene device with Au leads. In this case, I studied the ZBA found in the four probe resistance, so the leads are not aligned to individual grains.

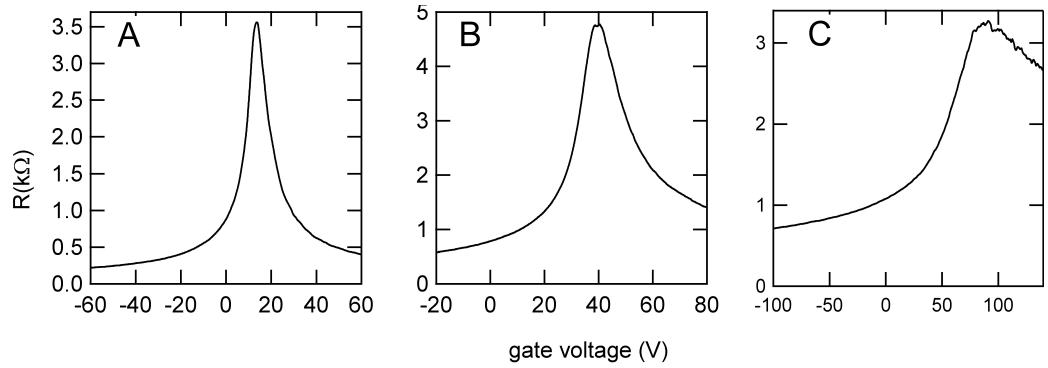

Figure 5.10: Square resistance vs. gate voltage for three different Au grain coverages. A: A control sample with no Au grains. B: A sample with intermediate coverage. C: A sample with dense grain coverage. An overall trend of higher doping and broader charge neutrality points can be clearly be seen with increased grain coverage.

grain coverage increases, the resistance maximum shifts to higher gate voltage, reaching $V_{g,max}$=85V in Fig. 5.10-C, indicating p-doping in graphene in accordance with the grain coverage. Similarly, the electron-hole asymmetry in the resistance maximum increases with grain coverage. A wider resistance peak in Fig. 5.10-B with two visible maxima and electron hole asymmetry would be qualitatively consistent with theoretical findings, [32] discrepancies may be due to the fact that electrons can follow a large number of paths and the resistance curve reflects an averaging of these paths.

Using the fabrication technique described earlier, the high density sample has two probes attached to a single grain, the two probes are used to subtract the resistance between the Au grain and the Cr/Au probe, as well as at least part of the sheet resistance of the bulk graphene. Fig. 5.11 shows both an optical and SEM image of the probe under discussion. Between this and the control sample, I can form a much better picture of what the meaning of the data from four probe measurements mean.

Fig. 5.12-B shows that the bulk resistance in the high grain coverage sample, increases with the perpendicular applied magnetic field. In the intermediate grain coverage sample, the resistance increases with magnetic field up to 8T, where it starts to decrease with the field (not shown). Quantum Hall effect is not yet developed in

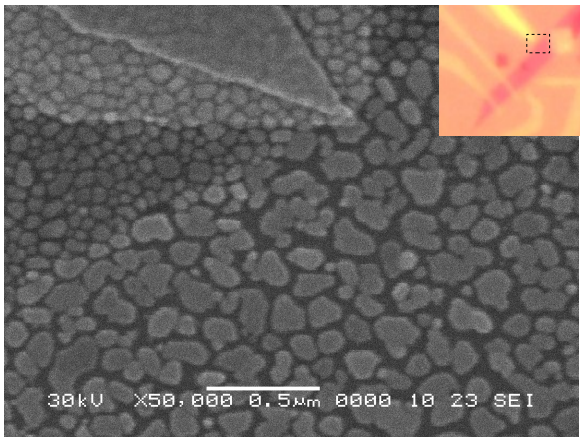

Figure 5.11: The sample reported here for dense grain coverage, as well as the particular probe featured in the 3 probe measurements. The inset shows an optical image of the device with a dashed line indicating the approximate area of the SEM image. It is interesting to note that the change in island morphology between SiO_2 is reflected in optical contrast.

that sample at 12T.

The electron-hole asymmetry in bulk resistance, versus grain coverage, can be explained by p-n junctions, as in Ref. [33]. Since the graphene channels in Fig. 5.11 are short and wide, the channels will be doped because of the proximity to the contact. [66, 32, 67] From the calculations in Refs. [67], I estimate that the charge density near the middle of the channels, at zero gate voltage, is approximately 50% of the charge density directly under the contact. At the gate voltage below the resistance maximum, both the channels and the graphene under the contact are p-doped. As the gate voltage increases, the charge neutrality will be reached in the channels first, creating p-n junctions, thereby reducing the slope in bulk resistance versus gate voltage. [33]

Next, I measure the effective contact resistance, defined as the ratio of the voltage measured between leads 3 and 4, and the current applied between leads 2 and 1 as shown in Fig. 5.9-B. Fig. 5.12-A displays the gate voltage dependence of the effective contact resistance, versus magnetic field. The resistance maximum is now near 120V, demonstrating that the doping is enhanced compared to the bulk. At

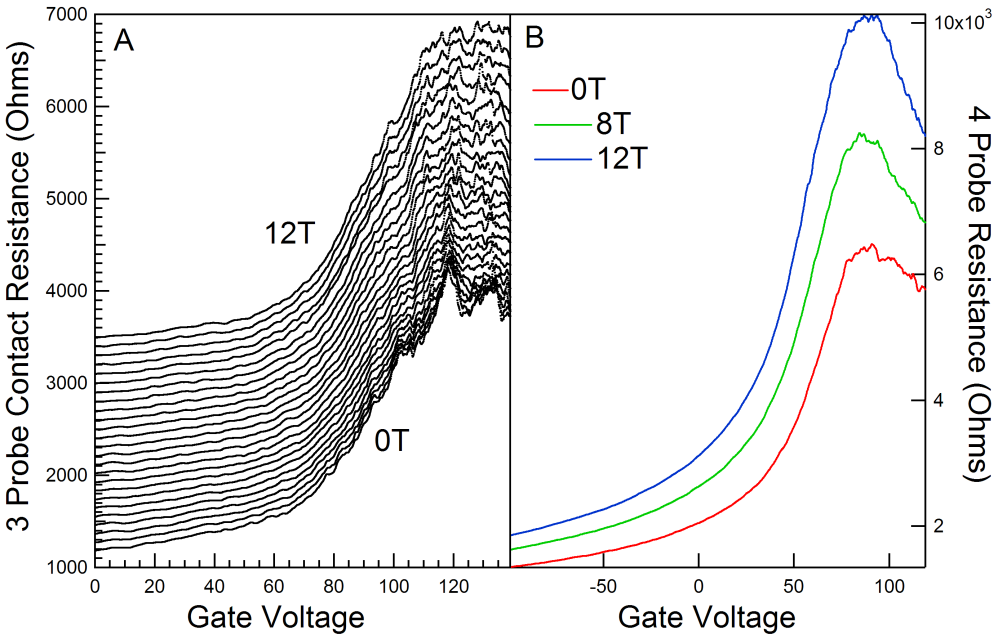

Figure 5.12: A: The 3 probe resistance vs gate voltage at different magnetic fields in the densely covered sample. Each successive scan increases the field by .5T, and is offset by 100 ohms. At large negative gate voltages, the curves are all roughly equal. B: The 4 probe sheet resistance is shown at several different magnetic fields. No quantum Hall effect is observed.

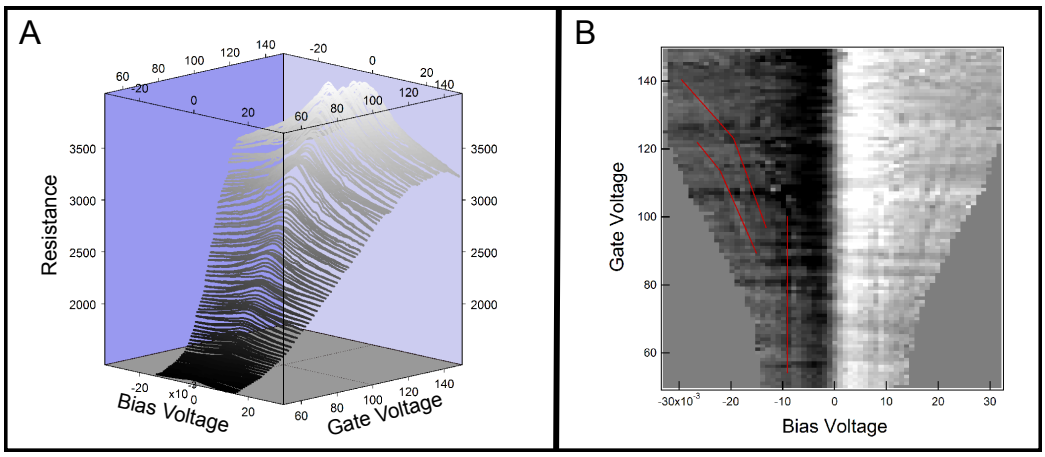

Figure 5.13: A: Plot of the resistance vs Bias voltage and Gate voltage for the 3 probe arrangement. Resonances can be seen that are symmetric with bias, as well as a ZBA that becomes larger near the charge neutrality point. B: Plot of dR/dV vs bias and gate voltage derived from the data in A. The resonances are outlined on the left in red lines, and their symmetric counterparts can be seen on the positive bias side. The gray area does not have any data due to the fact that the applied voltage varied slightly with sample resistance.

120V, the added electron density in graphene, induced by the gate charge, is $n = C_g V_{g,max}/|e| = 9.3 \cdot 10^{12}/cm^2$, where C_g is the capacitance to the gate per unit area, measured to be $12.4nF/cm^2$ on a test sample from the same batch of oxidized Si-wafers. This corresponds to the p-doping in graphene with a Fermi level shift $\Delta E_F = \hbar v\sqrt{\pi n} = 0.35eV$, where I assume that $v = 10^6 m/s$. First principle calculations of the Fermi level shift under a clean Au-graphene contact, under $\langle 111 \rangle$ Au face, predict that $\Delta E_F = 0.19eV$ and the equilibrium separation between the carbon atoms in the graphene sheet and the Au atoms of the top-most Au layer 3.3Å. [30, 68] The calculation leads to $\Delta E_F = 0.35eV$ at the separation of $\approx 4\mathring{A}$. [30, 68] It should be noted that experiments on HOPG using solid metal tips of Cu and Al have also observed large changes in the transport properties for small changes in the tip-graphite distance. [69]

The observed Fermi level shift is also larger than reported in previous experiments. The effects of individual Au atom adsorbates on graphene conduction have

been investigated at low temperatures. [70] Individual Au atoms lead to n-doping in graphene, but as Au-atoms bind into clusters, the Fermi level shifts back to neutrality. [70] The measurements of ΔE_F in large Ti/Au-graphene contacts, obtain $\Delta E_F = 0.25eV$ by photocurrent microscopy, [71] but those contacts involved electron-beam lithography over graphene, before the metal deposition. Photoemission spectroscopy of SiC-graphene with intercalation of Au monolayers displayed smaller p doping, $\Delta E_F = 0.1eV$. [72]

At zero gate voltage, the effective contact resistance is 915Ω. The contact area between the grain and graphene, estimated from the sample image, is $\approx 0.016\mu m^2$, so the effective resistivity of the contact would be $\rho = 14.6 \cdot 10^{-8}\Omega cm^2$. Alternatively, the diameter of the grain is approximately 140nm, and so the effective resistance per unit length is only $128\Omega\mu m$, comparable to the current record. [59] At -100V on the back gate, the specific contact resistance drops to $95\Omega\mu m$. The effective contact resistance measured in other similarly sized grains agrees with the above.

The effective contact resistance is equal to the contact resistance only if the spread resistance from graphene under the contact and from graphene surrounding the contact is negligibly small compared to the contact resistance. If the spread resistance is significant, then the effective contact resistance will be larger than the contact resistance. Thus, the estimate presents an upper bound of the contact resistance. I expect that effective contact resistance is not far above the contact resistance.

The contribution to the effective contact resistance from the graphene channels cannot be strong, because of the very weak magnetic field dependence of the effective contact resistance compared to the bulk (Figs. 5.12 A& B). The graphene channels are less doped than the graphene directly under the contact. Since the maximum in the effective contact resistance is 30V above the bulk resistance maximum, the channels have a reduced contribution to the effective contact resistance.

Next, I discuss nonequilibrium electron transport. Figs. 5.14 A & B display bulk

differential resistance versus bias voltage at 4.2K, in samples with intermediate and high grain coverage, respectively. In this measurement, a 4 probe resistance measurement of the graphene/Au grain system is measured and graphed versus the DC bias voltage applied to the current source leads. The dominant feature in the figure is a resistance maximum near zero bias voltage, or a zero-bias anomaly (ZBA). The ZBA is common in mesoscopic electron transport, and generally arises from the enhancement of electron-electron interactions in samples with restricted dimensions and weak disorder. [73, 74, 63] Similar ZBA is confirmed in the control sample, although the ZBA versus magnetic field, in the control sample exhibits oscillations between resistance maxima and the resistance minima, due to the quantum Hall effect.

The ZBA in Au-covered graphene samples exhibits additional peaks. The first peak is observed near ±70mV, as indicated by arrows in Fig. 5.14. All the peak locations are symmetric with respect to the sign of the bias voltage. The absence of peaks below 70mV suggest that the sample resistance is affected by some inelastic scattering process requiring an energy difference of at least 70meV.

Inelastic conduction thresholds near 70meV have been observed in scanning tunneling spectroscopy in graphene [75] and in graphene tunnel junctions. [55] They have been attributed to the 67 meV out-of-plane acoustic graphene phonon modes located near the K/K' points in reciprocal space. [76] In this case, the energy to overcome the additional energy barrier comes from the non-equilibrium distribution of electrons by creating an effective temperature eV_B/k_T (in the absence of electron-phonon relaxation).

The DC bias dependence of all three samples is shown in Fig. 5.15. As the coverage becomes larger, the reversal of the resistance peak to a resistance dip is seen to disappear, as the QHE is also seen to disappear. The resonances can also be seen in the Au grain samples, and Fig. 5.15-D demonstrates a very clear signature of the resonances with magnetic field by taking a numerical derivative of the data, leading

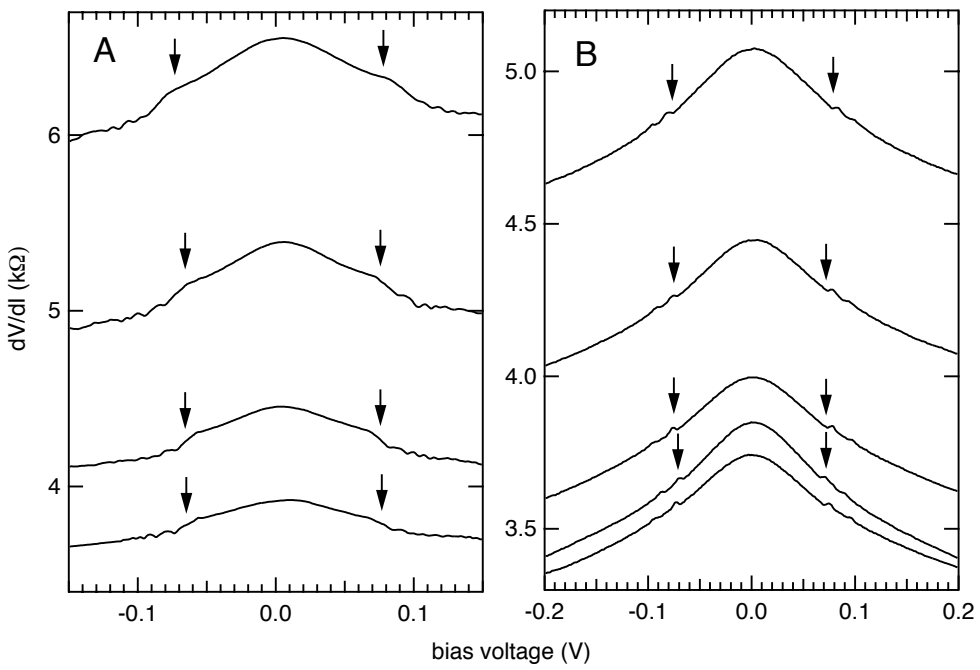

Figure 5.14: Resonances seen in the 4 probe resistance at different magnetic fields in the Intermediate (A) and Dense (B)coverage samples

to a d^2V/dI^2 signal. This signal is often used in inelastic spectroscopy. [19]

Fig. 5.16 displays the dR/dV vs. bias for the Densely covered sample. A complex pattern can be clearly seen, but it is not yet completely clear what interaction is being probed. Electron-phonon, [77] and electron-plasmon [78] have recently been probed by other spectroscopic methods. Ref. [77] found a carrier density dependence to the interaction, but such a dependence for the electron-plasmon interaction has yet to be measured. Though the effect has been observed in multiple samples, more samples are necessary to determine how reproducible the pattern is from sample to sample, to measure the spectrum more sensitively, and to isolate the details of sample fabrication necessary to best observe the inelastic features.

In conclusion, Au grains in clean contact with graphene lead to significant p-doping, with the Fermi level shift $\Delta E_F = 0.35eV$, consistent with first principle

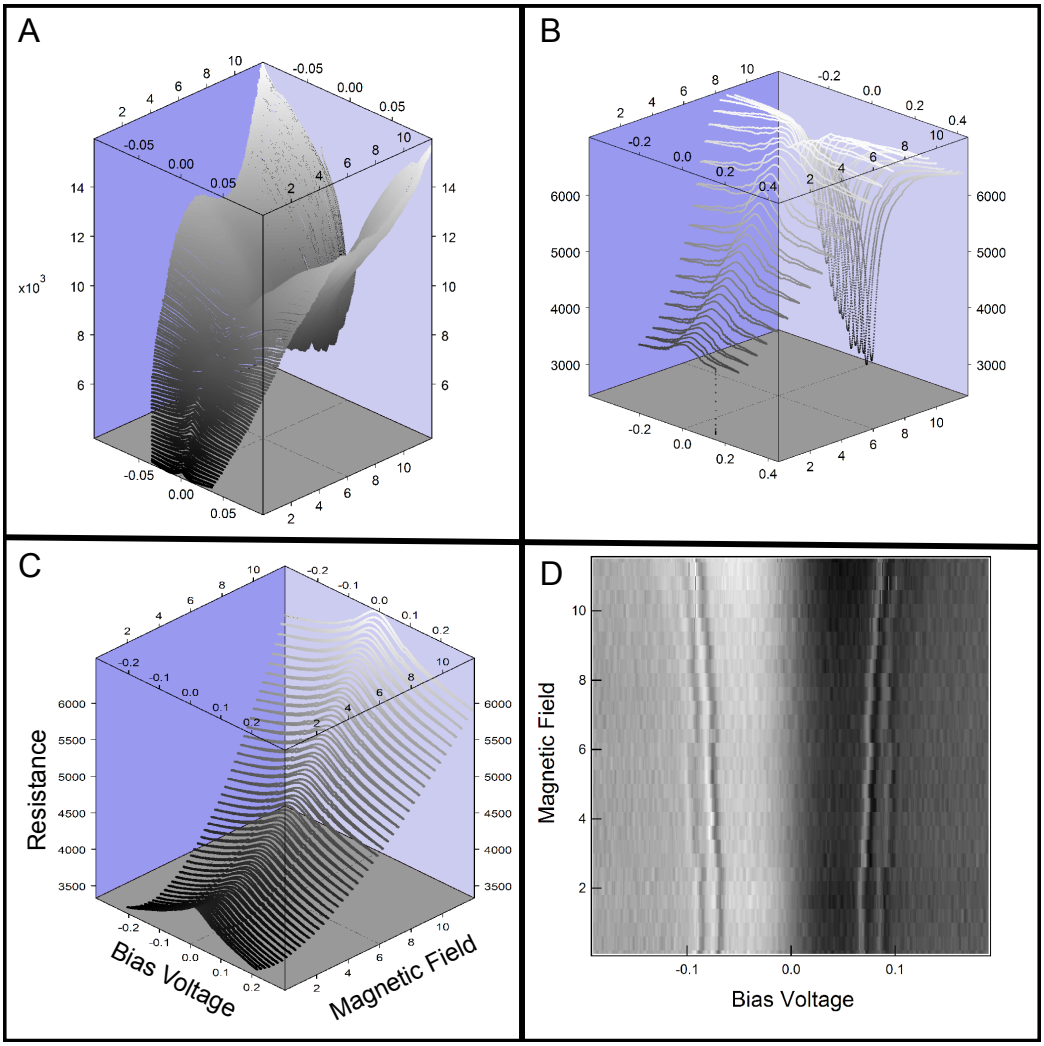

Figure 5.15: Resistance vs Bias voltage and Magnetic Field for Control (A), Intermediate (B), and Dense (C) coverage samples. D) d^2R/dV^2 vs bias voltage and field to enhance the resonances seen in the Dense coverage sample. A weak magnetic field dependence can be seen as the resonances become more widely spaced at higher fields.

calculations if the separation between the the graphene layer and the Au layer closest to the graphene is greater by $\approx$1Å with respect to equilibrium on the $< 111 >$ face. The substrate interaction can affect the separation between carbon and Au atoms. Nonuniform conformation of the substrate may play a big role. Van der Waals contributions from the SiO_2 substrate that are not included in the first principle calculations, may also induce large graphene-metal separations. Nonequilibrium electron transport in Au-covered graphene exhibits inelastic thresholds at the giant phonon energy in graphene, confirming a new, and fairly direct method of measuring inelastic scattering at a metal-graphene interface.

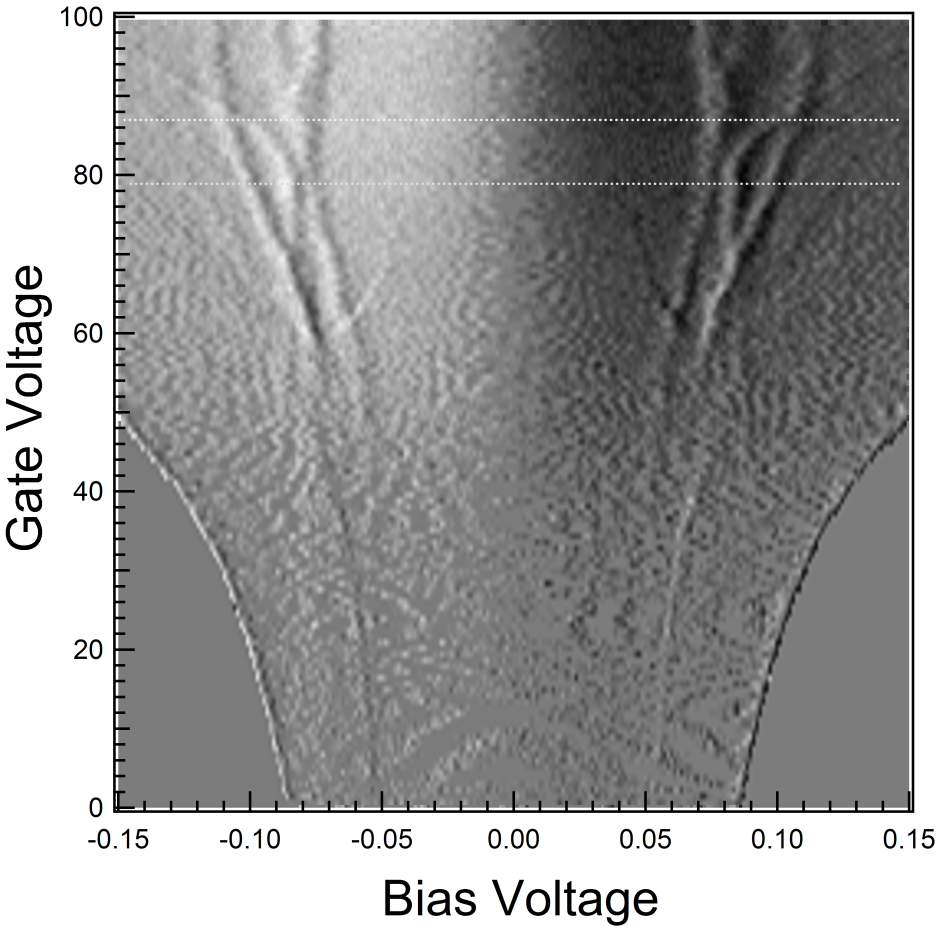

Figure 5.16: The gate voltage dependence of the inelastic peaks in the two probe dR/dV. The dashed lines bound the location of the charge neutrality point. In this sample, the two probe DC voltage is inferred from the applied DC current and the small signal AC two probe voltage.

CHAPTER VI

CONCLUDING REMARKS AND FUTURE WORK

Graphene has been a very popular topic of research in recent years, largely because of the ease access to the basic materials, and the widespread belief that it could be useful in the electronics industry. In many studies, graphene is treated in isolation: a carbon sheet, infinite in extent, and floating somewhere in space far from any perturbing influences. The fact that in many ways a real sample behaves this way is another reason for its allure. However, the effect of real materials on graphene is important, and the influence of metals is possibly of very great importance. With both tunneling and contact experiments, I believe I have shown some merit to the idea that metal contacts, and particularly the choice of metal used can have as great an effect on graphene as in Si and other semiconductor devices.

The main utility of the tunneling studies is a method to directly probe the quality of graphene in devices with very thin gate dielectrics. Such information, in conjunction with FET data can be more valuable to assessing a device than by FET data alone since the quantum capacitance can be directly probed, and the uniformity can to some extent be evaluated.

Though the tunneling studies presented here are of high quality and I believe further refinement of the techniques and material could create even higher quality devices, the interface between graphene and a metal is still interrupted by both an oxide and resist residue. Also, STM measurements have proven that they can work at both high fields and low temperatures, comparable to those available in our lab, and will most likely continue to stay ahead of us in terms of physics results. The fact that I can obtain similar results in a realistic device geometry at a fraction of the cost

is heartening, but perhaps does not by itself merit future studies.

Samples involving clean metal contacts in the form of the high temperature evaporated islands is in my opinion the most fruitful course for future study. A scanning probe method is less obviously applicable to this system, as a probe cannot fit into the interface formed between the graphene and metal, and a tip actually made of the metal in question may or may not behave the same way as a contact with no external mechanical forces acting on it. The method also seems a more direct and relevant way to answer questions of charge transfer between a graphene and a bulk metal.

Therefore, I suggest that more metals be explored, including those that I did not consider due to concerns over oxidation. Vacuum baking of e-beam resists or other methods may be employed to avoid oxidation. Many different metals have been considered theoretically, and as many of these as possible should be investigated so that a general theory of a metal-graphene contact can be agreed upon by the community. With theoretical support, perhaps the meaning of some aspects of the inelastic spectra will become clear, and the technique will shed light on the phonon spectrum of the metal graphene interface, and the nature of the metal-graphene interaction.

Another direction is to attempt to construct devices from individual islands. New geometries could offer a way to better define the area of graphene contacting a metal. These experiments may be able to differentiate what aspects of our data are universal of the metal contacts, and which are pathological to a specific contact. By employing a plasma etch step, contact areas to specific grains could be defined. Perhaps some metals will prove to protect graphene more effectively than PMMA. With the right choice of metal and island size very small, high quality devices may be possible.

APPENDIX A

MATLAB CODE

This code is used to generate a density of states in disordered graphene

```
%M is the number of atoms on each side of the graphene square, N is the
%number of atoms, M must be odd, and N must be even, or the periodic
%boundary conditions won't work.  Keep M<~71 to diagonalize the matrix
%exactly.  An odd number is an A atom, an even number is a B atom.
M=121;
N=M^2+M;

%R is the lattice constant, t is the transfer integral, A is the area, and
%various physical constants
R=2.46e-10;
t=2.7;
A=5.24e-20*N/2;
hbar=6.58e-16;
e=1.61e-19;
eps0=8.85e-12;

%functions that link lattice site index to x,y coordinates
xa = @(p) (sqrt(3)/2)*((rem(p-1,M)));
yab = @(q) .5*floor((q-1)/M);
xb = @(r) (sqrt(3)/2)*(rem(r-1,M))+1/(2*sqrt(3));

%Nimp randomly placed impurities, the impurities sit 3.4A above the lattice
Nimp=2;
ei=0;
r=zeros(3,Nimp);
q=1;
while(q<=Nimp)
    r(1,q)=rand(1)*(xb(M-1));
    r(2,q)=rand(1)*(yab(N));
    r(3,q)=2*round(rand(1))-1;
    q=q+1;
end
r(3,:)=0*[1  -1];

%A sparse matrix is used to save on memory space (since each row/column has
%three entries, this is a huge savings and allows the program to run much,
%much faster).  The first and last atoms are assigned their elements first
%since the boundary conditions are more complicated
H=sparse([1  1 N N],[2  1+M N-1 N-M], [-t -t -t -t],N,N);

%This constructs the full Hamiltonian
n=1;
while(n<=N)
    %condition if A(odd) and B(even) sublattices are not on an edge
```

```
if((rem(n,2)==1)&&(rem(n-1,M)~=0)&&(n-M>0)&&(n+M<=N)&&(n~=1))
    xn = xa(n);
    yn = yab(n);
    x1 = xb(n-1);
    y1 = yab(n-1);
    xp = xb(n+M);
    yp = yab(n+M);
    xm = xb(n-M);
    ym = yab(n-M);
    ei=U0*sum(r(3,:)./sqrt((r(1,:)-xn).^2+(r(2,:)-yn).^2+(3.4/2.46)^2));
    H=H+sparse([n n n n],[n-1 n-M n+M n], [-t -t -t ei],N,N);
elseif((rem(n,2)~=1)&&(rem(n,M)~=0)&&(n-M>0)&&(n+M<N)&&(n~=N))
    xn = xb(n);
    yn = yab(n);
    x1 = xa(n+1);
    y1 = yab(n+1);
    xp = xa(n+M);
    yp = yab(n+M);
    xm = xa(n-M);
    ym = yab(n-M);
    ei=U0*sum(r(3,:)./sqrt((r(1,:)-xn).^2+(r(2,:)-yn).^2+(3.4/2.46)^2));
    H=H+sparse([n n n n],[n+1 n-M n+M n],[-t -t -t ei],N,N);
%A or B atom lies on a top armchair edge
elseif((rem(n,2)==1)&&(rem(n-1,M)~=0)&&((n-M)<=0)&&((n+M)<N)&&(n~=1))
    xn = xa(n);
    yn = yab(n);
    x1 = xb(n-1);
    y1 = yab(n-1);
    xp = xb(n+M);
    yp = yab(n+M);
    xm = xb(n+N-M);
    ym = yab(n+N-M);
    ei=U0*sum(r(3,:)./sqrt((r(1,:)-xn).^2+(r(2,:)-yn).^2+(3.4/2.46)^2));
    H=H+sparse([n n n n],[n-1 n+M n+N-M n], [-t -t -t ei],N,N);
elseif((rem(n,2)~=1)&&(rem(n,M)~=0)&&((n-M)<0)&&((n+M)<N))
    xn = xb(n);
    yn = yab(n);
    x1 = xa(n+1);
    y1 = yab(n+1);
    xp = xa(n+M);
    yp = yab(n+M);
    xm = xa(n+N-M);
    ym = yab(n+N-M);
    ei=U0*sum(r(3,:)./sqrt((r(1,:)-xn).^2+(r(2,:)-yn).^2+(3.4/2.46)^2));
    H=H+sparse([n n n n],[n+1 n+M n+N-M n], [-t -t -t ei],N,N);
%A or B atom lies on bottom armchair edge
elseif((rem(n,2)==1)&&(rem(n-1,M)~=0)&&((n-M)>0)&&((n+M)>N))
    xn = xa(n);
    yn = yab(n);
    x1 = xb(n-1);
    y1 = yab(n-1);
    xp = xb(n-N+M);
    yp = yab(n-N+M);
    xm = xb(n-M);
    ym = yab(n-M);
```

```
        ei=U0*sum(r(3,:)./sqrt((r(1,:)-xn).^2+(r(2,:)-yn).^2+(3.4/2.46)^2));
        H=H+sparse([n n n n],[n-1 n-M n-N+M n], [-t -t -t ei],N,N);
    elseif((rem(n,2)~=1)&&(rem(n,M)~=0)&&((n-M)>0)&&((n+M)>N)&&(n~=N))
        xn = xb(n);
        yn = yab(n);
        x1 = xa(n+1);
        y1 = yab(n+1);
        xp = xa(n-N+M);
        yp = yab(n-N+M);
        xm = xa(n-M);
        ym = yab(n-M);
        ei=U0*sum(r(3,:)./sqrt((r(1,:)-xn).^2+(r(2,:)-yn).^2+(3.4/2.46)^2));
        H=H+sparse([n n n n],[n+1 n-M n-N+M n],[-t -t -t ei],N,N);
    %B atom lies on right zigzag edge
    elseif((rem(n,2)~=1)&&(rem(n,M)==0)&&(n-M>0)&&(n+M<N)&&(n~=N))
        xn = xb(n);
        yn = yab(n);
        xr = xa(n+1-2*M);
        yr = yab(n+1-2*M);
        xp = xa(n+M);
        yp = yab(n+M);
        xm = xa(n-M);
        ym = yab(n-M);
        ei=U0*sum(r(3,:)./sqrt((r(1,:)-xn).^2+(r(2,:)-yn).^2+(3.4/2.46)^2));
        H=H+sparse([n n n n],[n-M n+M n+1-2*M n],[-t -t -t ei],N,N);
    %A atom lies on left zigzag edge
    elseif((rem(n,2)==1)&&(rem(n-1,M)==0)&&(n-M>0)&&(n+M<N)&&(n~=1))
        xn = xa(n);
        yn = yab(n);
        xr = xb(n-1+2*M);
        yr = yab(n-1+2*M);
        xp = xb(n+M);
        yp = yab(n+M);
        xm = xb(n-M);
        ym = yab(n-M);
        ei=U0*sum(r(3,:)./sqrt((r(1,:)-xn).^2+(r(2,:)-yn).^2+(3.4/2.46)^2));
        H=H+sparse([n n n n],[n-M n+M n-1+2*M n],[-t -t -t ei],N,N);
    end
    n=n+1;
end
%calculates eigenvalues and eigenvectors, or just some eigenvalues
%[V,E]=eig(full(H));
%E=eig(full(H));
E=eigs(H,500,1/N);
%Calculates a DOS from the discrete spectrum, dE is the width of a gaussian
%broadening function
dE=.005;
eps=(-1:.0001:1);
DOS=0*eps;
m=1;
p=1;
while(m<=(length(eps)))
    %Use for simple global DOS
    DOS(m)=sum((1/(sqrt(2*pi*dE^2)))*exp(-(eps(m)-E).^2/(2*dE^2)));
```

```
    %bins the DOS
    %a=sign((eps(m)+dE/2)-E)+1;
    %b=sign(E-(eps(m)-dE/2))+1;
    %DOS(m)=sum(a.*b)/(2*dE);

    %Use for LDOS, must calculate the eigenvectors
    %DOS(m)=sum((V(N/2+1,:).^2).*(1/(sqrt(2*pi*dE^2)))...
    %.*exp(-(eps(m)-E).^2/(2*dE^2)));
    m=m+1;
end
%Normalizes the density of states so that the final answer is in
%states/(eV m^2)
DOS=DOS/A;
plot(eps,DOS);

%Code for creating a lattice image, great for checking your math!
m=1;
dl=.02;
[X,Y]=meshgrid([-.5:.01:2],[-.5:.01:2]);
Lattice=0*X;
while(m<=N)
    if(rem(m,2)==1)
        Lattice=Lattice+((1/(sqrt(2*pi*dl^2)))*...
            exp(-(X-xa(m)).^2/(2*dl^2))).*...
            ((1/(sqrt(2*pi*dl^2)))*exp(-(Y-yab(m)).^2/(2*dl^2)));
    else
        Lattice=Lattice-((1/(sqrt(2*pi*dl^2)))*...
            exp(-(X-xb(m)).^2/(2*dl^2))).*...
            ((1/(sqrt(2*pi*dl^2)))*exp(-(Y-yab(m)).^2/(2*dl^2)));
    end
    m=m+1;
end
m=1;
while(m<=Nimp)
    Lattice=Lattice+((1/(sqrt(2*pi*dl^2)))*...
        exp(-(X-r(1,m)).^2/(2*dl^2))).*...
        ((1/(sqrt(2*pi*dl^2)))*exp(-(Y-r(2,m)).^2/(2*dl^2)));
    m=m+1;
end
```

This is the code used to generate a conductance map given a density of states and a doping level

```
%introduce constants: electronic charge, hbar, Fermi velocity and gate
%capacitance per unit area

e=1.61e-19;
hbar=6.58e-16;
vf=1e6;
Cg=124e-6;

%introduce parameters: probe capacitance, doping level, and the accuracy to
%which the Fermi level should be calculated

Cp=225*Cg;
```

```
u0=0;
ufstep=1e-4;

%introduce the energy scale and calculate the density of states
eps=(-1:.0001:1);
% DOS=2/(pi*vf^2*hbar^2)*abs(eps);

%uncomment for the DOS in a magnetic field
DOS=0*eps;
i=-500;
while(i<=500)
    DOS=DOS+((2*12*(.0035))/(pi^2*hbar))./...
        ((eps-sign(i)*vf*sqrt(2*hbar*12*abs(i))).^2+.0035^2);
    i=i+1;
end

%u0i is the numerical index of the doping level
u0i=round((u0+1)/ufstep)+1;

%Vg and Vp define the grid of gate and probe voltage points
Vg=(100:-.5:-100);
Vp=(-.21:.001:.21);

%Q is used as a charge on the graphene for a given Fermi level, this is
%used to reduce the number of calculations performed to determine the Fermi
%level
Q=0*eps;

%uf is the value of the Fermi level for a given gate and probe voltage
uf=zeros(length(Vg),length(Vp));

%duf is the derivative vs Vp of the Fermi level
duf=uf;

%G is DOS(uf+eVp)
G=uf;

%G is DOS(uf+eVp)(duf+1)-DOS(uf)duf
G1=uf;

%indices used in the loops
m=1;
n=1;
q=1;

%Calculates the charge on the graphene for a given Fermi level
%using the trapezoid rule, saves calculation steps later.
while(q<length(DOS))
    Q(q)=e*(ufstep/2)*(sign(q-u0i)*sum(DOS(u0i:sign(q-u0i):q))...
        +sign(q+1-u0i)*sum(DOS(u0i:sign(q+1-u0i):q+1)));
    q=q+1;
end

%The Fermi level is calculated for each gate and probe voltage by searching
%for the zero crossing of the test function.  The test function assumes the
```

```
%Fermi level is -1 and stops guessing if 1 is reached.  To speed up the
%process, large steps are taken at first, and then the program backs up and
%takes smaller guesses.
while(n<=length(Vg))
    while(m<=length(Vp))
     q=1;
     uf(n,m)=eps(q);
     f=Cp*(Vp(m)+uf(n,m))+Cg*(Vg(n)+uf(n,m))-(Cp+Cg)*u0+Q(q);
     if(f<0)
          while((f<0)&&(uf(n,m)<(1-.005)))
               uf(n,m)=eps(q);
               f=Cp*(Vp(m)+uf(n,m))+Cg*(Vg(n)+uf(n,m))-(Cp+Cg)*u0+Q(q);
               q=q+50;
          end
     elseif(f>0)
          while((f>0)&&(uf(n,m)<(1-.005)))
               uf(n,m)=eps(q);
               f=Cp*(Vp(m)+uf(n,m))+Cg*(Vg(n)+uf(n,m))-(Cp+Cg)*u0+Q(q);
               q=q+50;
          end
     end
     q=q-100;
     uf(n,m)=eps(q);
     f=Cp*(Vp(m)+uf(n,m))+Cg*(Vg(n)+uf(n,m))-(Cp+Cg)*u0+Q(q);
     if(f<0)
          while((f<0)&&(uf(n,m)<(1-ufstep)))
               uf(n,m)=eps(q);
               f=Cp*(Vp(m)+uf(n,m))+Cg*(Vg(n)+uf(n,m))-(Cp+Cg)*u0+Q(q);
               q=q+1;
          end
          m=m+1;
     elseif(f>0)
          while((f>0)&&(uf(n,m)<(1-ufstep)))
               uf(n,m)=eps(q);
               f=Cp*(Vp(m)+uf(n,m))+Cg*(Vg(n)+uf(n,m))-(Cp+Cg)*u0+Q(q);
               q=q+1;
          end
          m=m+1;
     else
          m=m+1;
     end
    end
    m=1;
    n=n+1;
end

%Now the values of uf are known for all gate and probe voltages, the
%derivative of the Fermi function vs probe voltage is calculated.  In order
%to obtain a smooth fit, a quadratic function is fit over 11 points.  The
%mathematics for the fit is taken from Bevington's 'Data reduction and
%analysis'
r=11;
n=1;
m=1+r;
a=zeros(1,3);
```

```
alpha=zeros(3,3);
beta=zeros(1,3);
while(n<=length(Vg))
    while(m<length(Vp)-r)
        q=round((uf(n,m)+Vp(m)+1)/ufstep+1);
        p=round((uf(n,m)+1)/ufstep+1);
        beta=[sum(uf(n,m-r:m+r)) sum(uf(n,m-r:m+r).*Vp(m-r:m+r))...
            sum(uf(n,m-r:m+r).*((Vp(m-r:m+r).^2)))...
            sum(uf(n,m-r:m+r).*(Vp(m-r:m+r).^3))];
        alpha=[1+2*r sum(Vp(m-r:m+r)) sum(Vp(m-r:m+r).^2)...
            sum(Vp(m-r:m+r).^3); sum(Vp(m-r:m+r)) sum(Vp(m-r:m+r).^2)...
            sum(Vp(m-r:m+r).^3) sum(Vp(m-r:m+r).^4); sum(Vp(m-r:m+r).^2)...
            sum(Vp(m-r:m+r).^3) sum(Vp(m-r:m+r).^4) sum(Vp(m-r:m+r).^5);...
            sum(Vp(m-r:m+r).^3) sum(Vp(m-r:m+r).^4) sum(Vp(m-r:m+r).^5)...
            sum(Vp(m-r:m+r).^6)];
        a=beta*(alpha^(-1));
        duf(n,m)=a(2)+2*a(3)*(Vp(m))+3*a(4)*Vp(m)^2;

        %G and G1 are generated as each duf is calculated
        G(n,m)=DOS(q);
        G1(n,m)=DOS(q)*(1+duf(n,m))-DOS(p)*duf(n,m);
        m=m+1;
    end
    m=1+r;
    n=n+1;
end
```

APPENDIX B

ALTERNATIVE DERIVATION OF THE LINES IN THE CONDUCTANCE MAP

A careful look at the derivation of equations to extract meaning from the conductance maps will point out that the relationship between the actual conductance fluctuations and the DOS fluctuations is missing. Here, I follow through calculation necessary to show that a fluctuation in the DOS will be represented twice in a conductance map; as an upward and a downward sloping resonance. In addition, some insight is given into the effect of the probe capacitance on broadening the lines.

As shown earlier in this thesis, the expression for the conductance is

$$G(\mu, eV_p) = g(\mu + eV_p)(1 + \frac{d\mu}{deV_p}) - g(\mu)\frac{d\mu}{deV_p}. \tag{52}$$

The directional derivative in V_p, V_g space is

$$\begin{aligned} d\hat{G} = & \left[\frac{\partial g(E)}{\partial E}\left(1 + \frac{\partial \mu}{\partial eV_p}\right)^2 - \frac{\partial g(\mu)}{\partial \mu}\left(\frac{\partial \mu}{\partial eV_p}\right)^2 + (g(E) - g(\mu))\frac{\partial^2 \mu}{\partial eV_p^2}\right] de\hat{V}_p \\ + & \left[\frac{\partial g(E)}{\partial E}\frac{\partial \mu}{\partial eV_g}\left(1 + \frac{\partial \mu}{\partial eV_p}\right) - \frac{\partial g(\mu)}{\partial \mu}\frac{\partial \mu}{\partial eV_g}\frac{\partial \mu}{\partial eV_p} + (g(E) - g(\mu))\frac{\partial^2 \mu}{\partial eV_p \partial eV_g}\right] de\hat{V}_g. \end{aligned} \tag{53}$$

Now, if there is a resonance at energy E in the DOS function $g(E)$, there should be a feature associated with this in the conductance map. The resonance in the DOS occurs when $\partial g(E)/\partial E = 0$. The feature in the conductance map will point along a vector $\alpha e\hat{V}_p + \beta e\hat{V}_g$ such that $d\hat{G} \cdot \langle \alpha, \beta \rangle = 0$. Using Eq. 30, I find the following useful derivatives:

$$\frac{\partial \mu}{\partial eV_p} = \frac{-C_p}{C_p + C_g + e^2 g(\mu)} \tag{54}$$

$$\frac{\partial \mu}{\partial eV_g} = \frac{-C_g}{C_p + C_g + e^2 g(\mu)} \tag{55}$$

$$\frac{\partial^2 \mu}{\partial eV_p^2} = \frac{-e^2 \partial g(\mu)/\partial \mu}{C_p + C_g + e^2 g(\mu)} \left(\frac{\partial \mu}{\partial eV_p} \right)^2 \tag{56}$$

$$\frac{\partial^2 \mu}{\partial eV_p \partial eV_g} = \frac{-e^2 \partial g(\mu)/\partial \mu}{C_p + C_g + e^2 g(\mu)} \frac{\partial \mu}{\partial eV_p} \frac{\partial \mu}{\partial eV_g}. \tag{57}$$

Combining these derivatives with Eq. 53, I find the

$$\begin{aligned} d\hat{G} \cdot < \alpha, \beta > &= \alpha \frac{\partial g(\mu)}{\partial \mu} \left(C_p^2 + \frac{e^2 C_p^2 (g(E) - g(\mu))}{C_p + C_g + e^2 g(\mu)} \right) \\ &+ \beta \frac{\partial g(\mu)}{\partial \mu} \left(C_p C_g + \frac{e^2 C_p C_g (g(E) - g(\mu))}{C_p + C_g + e^2 g(\mu)} \right) = 0. \end{aligned} \tag{58}$$

So I find that

$$\frac{\beta}{\alpha} = -\frac{C_p}{C_g}.$$

Similarly, if the DOS fluctuation is represented by $\partial g(\mu)/\partial \mu$

$$\begin{aligned} d\hat{G} \cdot < \alpha, \beta > = &\ \alpha \frac{\partial g(E)}{\partial E} \left(1 - \frac{C_p}{C_p + C_g + e^2 g(\mu)} \right)^2 \\ &+ \beta \frac{\partial g(E)}{\partial E} \left(\frac{C_g}{C_p + C_g + e^2 g(\mu)} \left(1 - \frac{C_p}{C_p + C_g + e^2 g(\mu)} \right) \right) = 0, \end{aligned} \tag{59}$$

and in this case I find that

$$\frac{\beta}{\alpha} = 1 + \frac{e^2 g(\mu)}{C_g}$$

Hence, on lines of constant energy, fluctuations are stretched out in the direction of the lines of constant Fermi level, and on the lines of constant Fermi level, the fluctuations are stretched on lines of constant energy. It is interesting to note that

the differential along the line of constant Fermi level, when following the vector $\langle C_p, -C_g \rangle / \sqrt{C_p^2 + C_g^2}$ is

$$dG|_\mu = \frac{\partial g(\mu + eV_p)}{\partial eV_p} \frac{C_g + e^2 g(\mu)}{C_p + C_g + e^2 g(\mu)} \frac{C_g}{\sqrt{C_p^2 + C_g^2}} deV_p. \tag{60}$$

Two limits of this equation become simple, though since the Fermi level is constant, this equation basically multiplies the slope of the conductance by a constant factor from the correct density of states. The first is when the density of states at the Fermi level is large so that

$$dG = \frac{\partial g(\mu + eV_p)}{\partial eV_p} \frac{1}{\sqrt{1 + (C_p/C_g)^2}} deV_p \tag{61}$$

The other limit is that when the DOS is zero, so that

$$dG = \frac{\partial g(\mu + eV_p)}{\partial eV_p} \frac{1}{(1 + C_p/C_g)\sqrt{1 + (C_p/C_g)^2}} deV_p \tag{62}$$

Both of these instances approach $dG = \partial g(\mu + eV_p)/\partial eV_p$ when the probe capacitance becomes significantly smaller than the gate capacitance. These corrective factors lead to a decrease in the measurement of D_0 from the expected value, or equivalently an increase in the Fermi velocity as measured from spectra.

APPENDIX C

SPIN INJECTION IN GRAPHITE

This is an experiment that produced decent results, but in too few samples. Overall, two samples, with six leads between them were fabricated and measured at 4K. The samples were thick exfoliated graphite flakes with Al_2O_3 tunnel junctions and Cobalt leads. Despite the bad yield, and relatively large noise levels, I did obtain spin transport data that compared favorably with results in single layer graphene. My failure to obtain reliable tunnel junctions in thick samples both prompted me to focus on single layer samples, and encouraged the attempt to make better tunneling junctions to graphene. So while there is not much data, I feel it worthwhile to present it here, as it does provide a starting point to what my thesis work actually ended up being.

Fig. C.1 shows SV1 and SV2. Many of the leads on these devices didn't work; however, SV1 had two working leads and SV2 had 4 working leads so that local and non-local measurements respectively could be done on these samples. Fig. C.2 shows the measurement for SV1, a strong and sharp switching behavior can be seen as the magnetic field is swept back and forth.

Fig. C.3 shows the non-local measurement in SV2. In this measurement, the current is sourced between two probes, while the voltage is read between two other probes that should normally read zero voltage. A rather large background signal is present in this sample, but the switching behavior is clearly observed even in the somewhat noisy raw data. In addition, it was possible to apply a perpendicular field using the double axis magnet described earlier. In this way, the spin dephasing time can be estimated from the full width half max of the minimum in the signal. This

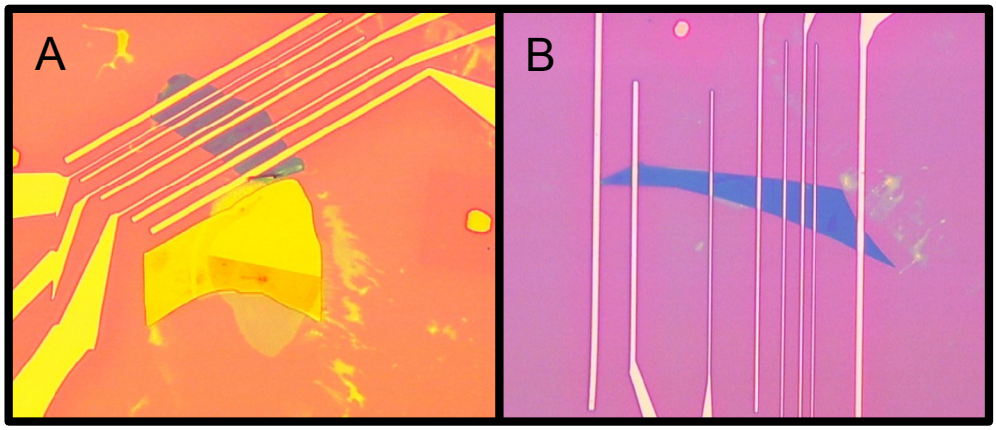

Figure C.1: A: Sample SV1, there were only two working leads on the device, spaced 8μm apart. B: Sample SV2 with 4 working leads, so that a non-local signal could be detected, also spaced 8μm apart.

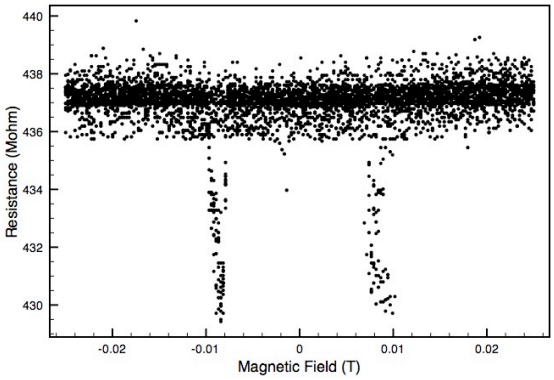

Figure C.2: Raw data for the spin valve signal observed on SV-1.

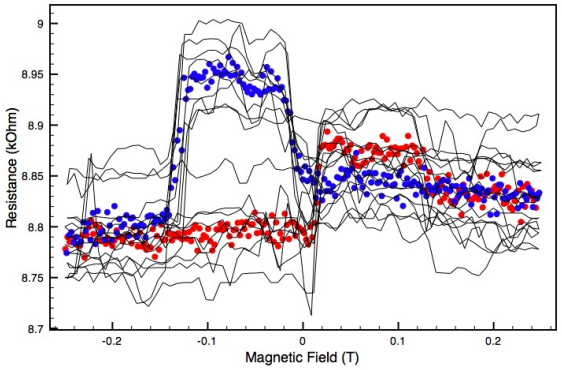

Figure C.3: Raw signal (black line), along with the averaged up signals (red dots) and averaged down signals (blue dots). Though noisy, the non-local signal is observed in device SV-2.

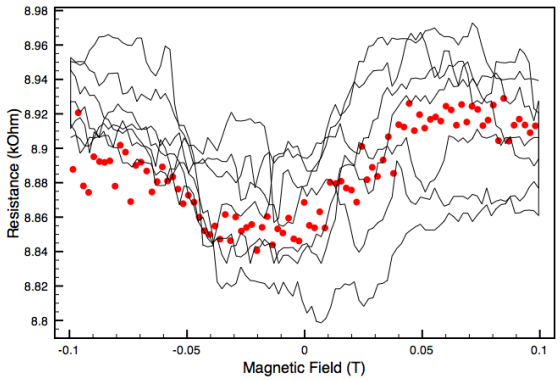

Figure C.4: Perpendicular field measurement in SV-2. The current passes underneath a floating lead, and may lead to a fringing field that causes the asymmetry in the measurement.

gives us a value of τ_d =190 ps, that compares favorably to the data presented in ref. [45]. The Hanle signal is presented in Fig. C.4

REFERENCES

[1] A. K. Geim and K. S. Novoselov. The rise of graphene. *Nature Materials*, 6: 183, 2007.

[2] Robert C. Richardson and Eric N. Smith. *Quasi-Free-Standing Epitaxial Graphene on SiC Obtained by Hydrogen Intercalation*. Westview Press, 1998.

[3] Charles Kittel and Herbert Kroemer. *Thermal Physics*. Wiley and sons, 2004.

[4] Neil W. Ashcroft and N. David Mermin. *Solid State Physics*. Harcourt College Publishers, 1976.

[5] Supriyo Datta. *Electronic Transport in Mesoscopic Systems*. Cambridge University Press, 1995.

[6] Ryogo Kubo. Statistical-mechanical theory of irreversible processes. i. general theory and simple applications to magnetic and conduction problems. *Journal of the Physical Society of Japan*, 12:570–586, 1957.

[7] P. R. Wallace. The band theory of graphite. *Physical Review*, 71:622–634, 1947.

[8] Ben Yu-Kuang Hu, E H Hwang, and S Das Sarma. Density of states of disordered graphene. *Physical Review B*, 78:165411, 2008.

[9] F. Libisch, S. Rotter, J. Guttinger, C. Stampfer, and J. Burgdorfer. Transition to landau levels in graphene quantum dots. *Physical Review B*, 81:245411, 2010.

[10] S. Das Sarma, Shaffique Adam, E. H. Hwang, and Enrico Rossi. Electronic transport in two-dimensional graphene. *Reviews of Modern Physics*, 83:407–470, 2011.

[11] Shaffique Adam, E. H. Hwang, V. M. Galitski, and S. Das Sarma. A self consistent theory for graphene transport. *Proceedings of the National Academy of Sciences*, 014(47):18392–18397, 2007.

[12] E. H. Hwang and S. Das Sarma. Single-particle relaxation time versus transport scattering time in a two-dimensional graphene layer. *Physical Review B*, 77: 195412, 2008.

[13] M. Monteverde, C. Ojeda-Aristizabal, R. Weil, K. Bennaceur, M. Ferrier, S. Gueron, C. Giattli, H. Bouchiat, J. N. Fuchs, and D. L. Maslov. Transport and elastic scattering times as probes of the nature of impurity scattering in single-layer and bilayer graphene. *Physical Review Letters*, 2010.

[14] Shudong Xiao, Jian-Hao Chen, Shaffique Adam, Ellen D Williams, and Michael S Fuhrer. Charged impurity scattering in bilayer graphene. *Physical Review B*, 82, 2010.

[15] Jian-Hao Chen, Chaun Jang, Shudong Xiao, Masa Ishigami, and Michael S. Fuhrer. Intrinsic and extrinsic performance limits of graphene devices on sio$_2$. *Nature Nanotechnology*, 3:206–209, 2008.

[16] G. Gamow. The quantum theory of nuclear disintegration. *Nature*, 122:805–806, 1928.

[17] J. C. Fisher and I. Giaever. Tunneling through thin insulating layers. *Journal of Applied Physics*, 32:018–9456, 2008.

[18] E Wolf. Electron tunneling spectroscopy. *Reports on Progress in Physics*, 41: 1439, 1978.

[19] Paul K. Hansma, editor. *Tunneling Spectroscopy: Capabilities, Applications, and New Techniques*. Plenum Press, 1982.

[20] K S Novoselov, A K Geim, S V Morozov, D Jiang, Y Zhang, S V Dubonos, I V Grigorieva, and A A Firsov. Electric field effect in atomically thin carbon films. *Science*, 306:666–669, 2004.

[21] J. L. McChesney, Aaron Bostwick, Taisuke Ohta, Thomas Seyller, Karsten Horn, J. Gonzalez, and Eli Rotenberg. Extended van hove singularity and superconducting instability in doped graphene. *Physical Review Letters*, 104: 136803, 2010.

[22] Dmitri K. Efetov and Philip Kim. Controlling electron-phonon interactions in graphene at ultrahigh carrier densities. *Physical Review Letters*, 105:256805, 2010.

[23] Serge Luryi. Quantum capacitance devices. *Applied Physics Letters*, 52(6):501, 1988.

[24] Damon B. Farmer, Yu-Ming Lin, and Phaedon Avouris. Graphene field-effect transistors with self-aligned gates. *Applied Physics Letters*, 97:013103, 2010.

[25] D V Averin, A N Korotkov, and K K Likharev. Theory of single-electron charging of quantum wells and dots. *Physical Review B*, 44:6199–6211, 1991.

[26] H. R. Zeller and I. Giaever. Tunneling, zero-bias anomalies, and small superconductors. *Physical Review*, 181:789–799, 1969.

[27] Andrea C. Ferrari. Raman spectroscopy of graphene and graphite: Disorder, electronphonon coupling, doping and nonadiabatic effects. *Solid State Communications*, 143:47–57, 2007.

[28] Libo Gao, Wencai Ren, Feng Li, and Hui-Ming Cheng. Total color difference for rapid and accurate identification of graphene. *Nano Letters*, 2(8):1625–1633, 2008.

[29] Akio Fukushima, Akira Sato, Akio Iwasa, Yasuhiro Nakamura, Takeshi Komatsuzaki, and Yasuhiko Sakamoto. Attenuation of microwave filters for single-electron tunneling experiments. *IEEE Transactions on Instrumentation and Measurement*, 46:289–293, 1997.

[30] G. Giovannetti, P. A. Khomyakov, G. Brocks, V. M. Karpan, J. vandenBrink, and P. J. Kelly. Doping graphene with metal contacts. *Physical Review Letters*, 101:026803, 2008.

[31] Q. S. Ran, M. Z. Gao, X. M. Guan, Y. Wang, and Z. P. Yu. First-principles investigation on bonding formation and electronic structure of metal-graphene contacts. *Applied Physics Letters*, 94:103511, 2009.

[32] S. Barraza-Lopez, M. Vanevicand M. Kindermann, and M. Y. Chou. Effects of metallic contacts on electron transport through graphene. *Physical Review Letters*, 104:076807, 2010.

[33] B. Huard B, N. Stander, J. A. Sulpizio, and D. Goldhaber-Gordon. Evidence of the role of contacts on the observed electron-hole asymmetry in graphene. *Physical Review B*, 78:121402, 2008.

[34] A. Venugopal, L. Colombo, and E. M. Vogel. Contact resistance in few and multilayer graphene devices. *Applied Physics Letters*, 96:013512, 2010.

[35] K. Pi, K. M. McCreary, W. Bao, W. Han, Y. F. Chiang, Y. Li, S. W. Tsai, C. N. Lau, and R. K. Kawakami. Electronic doping and scattering by transition metals on graphene. *Physical Review B*, 80:075406, 2009.

[36] A Deshpande, W Bao, F Miao, and C Lau. Spatially resolved spectroscopy of monolayer graphene on sio$_2$. *Physical Review B*, 79:205411, 2009.

[37] Yuanbo Zhang, Victor W Brar, Feng Wang, Caglar Girit, Yossi Yayon, Melissa Panlasigui, Alex Zettl, and Michael F Crommie. Giant phonon-induced conductance in scanning tunnelling spectroscopy of gate-tunable graphene. *Nature Physics*, 4(8):627, 2008.

[38] Yuanbo Zhang, Victor W Brar, Caglar Girit, Alex Zettl, and Michael F Crommie. Origin of spatial charge inhomogeneity in graphene. *Nature Physics*, 5 (10):722–726, 2009.

[39] J Martin, N Akerman, G Ulbricht, T Lohmann, J H Smet, K von Klitzing, and A Yacoby. Observation of electron—[ndash]—hole puddles in graphene using a scanning single-electron transistor. *Nature Physics*, 4(2):144, 2007.

[40] G Li, A Luican, and E Andrei. Scanning tunneling spectroscopy of graphene on graphite. *Physical Review Letters*, 102:176804, 2009.

[41] D Miller, K Kubista, G Rutter, and M Ruan. Observing the quantization of zero mass carriers in graphene. *Science*, 324:924–927, 2009.

[42] Adina Luican, Guohong Li, and Eva Y. Andrei. Quantized landau level spectrum and its density dependence in graphene. *Physical Review B*, 83:041405, 2011.

[43] Y Zhang, J Small, W Pontius, and P Kim. Fabrication and electric-field-dependent transport measurements of mesoscopic graphite devices. *Applied Physics Letters*, 86:073104, 2005.

[44] Wei Han, K Pi, M McCreary, Yan Li, Jared J I Wong, A.G Swartz, and R.K Kawakami. Tunneling spin injection into single layer graphene. *Physical Review Letters*, 105:167202, 2010.

[45] Nikolaos Tombros, Csaba Jozsa, Mihaita Popinciuc, Harry T. Jonkman, and Bart J. van Wees. Electronic spin transport and spin precession in single graphene layers at room temperature. *Nature*, 448:571–574, 2007.

[46] I. Giaever and H. R. Zeller. Tunneling into and through evaporated semiconducting films. *The Journal of Vacuum Science and Technology*, 6:502, 1969.

[47] Hisao Miyazaki, Shunsuke Odaka, Takashi Sato, Sho Tanaka, Hidenori Goto, Akinobu Kanda, Kazuhito Tsukagoshi, Youiti Ootuka, and Yoshinobu Aoyagi. Inter-layer screening length to electric field in thin graphite film. *Applied Physics Express*, 1:034007, 2008.

[48] A Bachtold, M De Jonge, K Grove-Rasmussen, P L McEuen, M Buitelaar, and C Schönenberger. Suppression of tunneling into multiwall carbon nanotubes. *Physical Review Letters*, 87:166801, 2001.

[49] Vitor M. Pereira, Johan Nilsson, and A. H. Castro Neto. Coulomb impurity problem in graphene. *Physical Review Lettres*, 2007.

[50] Suyong Jung, Gregory Rutter, Nikolai N. Klimov, David B. Newell, Irene Calizo, Angela R. Hight-Walker, Nikolai B. Zhitenev, and Joseph A. Stroscio. Evolution of microscopic localization in graphene in a magnetic field from scattering resonances to quantum dots. *Nature Physics*, 2011.

[51] B. Huard B, J. A. Sulpizio, , N. Stander, K. Todd, B. Yang, and D. Goldhaber-Gordon. Transport measurements across a tunable potential barrier in graphene. *Physical Review Letters*, 98:236803, 2007.

[52] S Kim, J Nah, I Jo, D Shahrjerdi, and L Colombo. Realization of a high mobility dual-gated graphene field-effect transistor with al_2o_3 dielectric. *Applied Physics Letters*, 94:062107, 2009.

[53] T Wehling, I Grigorenko, and A Lichtenstein. Phonon-mediated tunneling into graphene. *Physical Review Letters*, 101:216903, 2008.

[54] J Tersoff. Contact resistance of carbon nanotubes. *Applied Physics Letters*, 74: 2122–2124, 1999.

[55] C. E. Malec and D. Davidovič. Transport in graphene tunnel junctions. *Journal of Applied Physics*, 109:064507, 2011.

[56] Richard E. Prange and Steven M. Girvin, editors. *The Quantum Hall Effect*. Springer-Verlag, 1987.

[57] A Neto, F Guinea, and N Peres. The electronic properties of graphene. *Reviews of Modern Physics*, 2009.

[58] H. H. Berger. Models for contacts to planar devices. *Solid-State Electronics*, 15:145–158, 1972.

[59] Fengnian Xia, Vasili Perebeinos, Yu ming Lin, Yanqing Wu, and Phaedon Avouris. The origins and limits of metal-graphene junction resistance. *Nature Nanotechnology*, 6:179–184, 2011.

[60] Joshua A. Robinson, Michael LaBella, Mike Zhu, Matt Hollander, Richard Kasarda, Zachary Hughes, Kathleen Trumbull, Randal Cavalero, and David Snyder. Contacting graphene. *Applied Physics Letters*, 98:053103, 2011.

[61] K. Nagashio, T. Nishimura, K. Kita, and A. Toriumi. Metal/graphene contact as a performance killer of ultra-high mobility graphene analysis of intrinsic mobility and contact resistance. *2009 IEEE International Electron Device Meeting*, page 1, 2009.

[62] Andrew Zangwill. *Physics at Surfaces*. Cambridge University Press, 1988.

[63] K. E. Nagaev. Nonlinear conductivity of diffusive normal-metal contacts. *Physics Letters A*, 189:134, 1994.

[64] R. Danneau, F. Wu, M. F. Craciun, S. Russo, M. Y. Tomi, J. Salmilehto, A. F. Morpurgo, and P. J. Hakonen. Shot noise in ballistic graphene. *Physical Review Letters*, 100:196802, 208.

[65] S. Russo, M. F. Craciun, M. Yamamoto, A. F. Morpurgo, and S. Tarucha. Contact resistance in graphene-based devices. *Physica E*, 42:677–679, 2010.

[66] P. Golizadeh-Mojarad and S. Datta. Effect of contact induced states on minimum conductivity in graphene. *Physical Review B*, 79:085410, 2009.

[67] P. A. Khomyakov, A. A. Starikov, G. Brocks, and P. J. Kelly. Nonlinear screening of charges induced in graphene by metal contacts. *Physical Review B*, 82: 115437, 2010.

[68] P. A. Khomyakov, G. Giovannetti, P. C. Rusu, G. Brocks, J. van den Brink, and P. J. Kelly. First-principles study of the interaction and charge transport between graphene and metals. *Physical Review B*, 79:195425, 2009.

[69] Asmerom Y. Ogbazghi. Conductance through nanometer-scale metal-to-graphite contacts. *Ph.D. Dissertation*, 2005.

[70] K. M. McCreary, K. Pi, A. G. Swartz, W. Han, W. Bao, C. N. Lau, F. Guinea F, M. I. Katsnelson, and R. K. Kawakami. Effect of cluster formation on graphene mobility. *Physical Review B*, 81:115453, 2010.

[71] Eduardo J. H. Lee, Kannan Balasubramanian, Ralf Thomas Weitz, Marko Burghard, and Klaus Kern. Contact and edge effects in graphene devices. *Nature Nanotechnology*, 2008.

[72] A. Varykhalov, M. R. Scholz, T. K. Kim, and O. Rader. Effect of noble-metal contacts on doping and band gap of graphene. *Physical Review B*, 82:121101, 2010.

[73] B. L. Altshuler and A. G. Aronov. Electron-electron interactions in disordered conductors. In A. L. Efros and M. Pollak, editors, *Electron-Electron Interactions in Disordered Systems*. Elsevier and Amsterdam, 1985.

[74] M. H. Devoret, D. Esteve, H. Grabert, G. L. Ingold, H. Pothier, and C. Urbina. Effect of the electromagnetic environment on the coulomb blockade in ultrasmall tunnel junctions. *Physical Review Letters*, 64:1824, 1990.

[75] Y. B. Zhang YB, V. W. Brar, F. Wang, C. Girit, Y. Yayon, M. Panlasigui, A Zettl, and M. F. Crommie. Giant phonon-induced conductance in scanning tunnelling spectroscopy of gate-tunable graphene. *Nature Physics*, 4:627–630, 2008.

[76] M. Mohr, J. Maultzsch, E Dobardzic, S. Reich, I. Milosevic, M. Damnjanovic, A. Bosak, M. Krisch, and C. Thomsen. Phonon dispersion of graphite by inelastic x-ray scattering. *Physical Review B*, 76:035439, 2007.

[77] Victor W. Brar, Sebastian Wickenburg, Melissa Panlasigui, Cheol-Hwan Park, Tim O Wehling, Yuanbo Zhang, Régis Decker, Çağlar Girit, Alexander V Balatsky, Steven G Louie, Alex Zettl, and Michael F Crommie. Observation of carrier-density-dependent many-body effects in graphene via tunneling spectroscopy. *Physical Review Letters*, 104(3):036805, 2010.

[78] Aaron Bostwick, Florian Speck, Thomas Seyller, Karsten Horn, Marco Polini, Reza Asgari, Allan H. MacDonald, and Eli Rotenberg. Observation of plasmarons in quasi-freestanding doped graphene. *Science*, 328:999–1002, 2010.

[79] W Bao, G Liu, Z Zhao, H Zhang, D Yan, A Deshpande, B J LeRoy, and C N Lau. Lithography-free fabrication of high quality substrate-supported and freestanding graphene devices. *Nano Research*, 3:9–102, 2010.

[80] C. W. J. Beenakker. Andreev reflection and klein tunneling in graphene. *Review of Modern Physics*, 80:1337–1354, 2008.

[81] C. Berger, Z. M. Song, X. B. Li, X. S. Wu, N. Brown, C. Naud, D. Mayou, T. B. Li, J. Hass, A. N. Marchenkov, E. H. Conrad, P. N. First, and W. A. de Heer. Electronic confinement and coherence in patterned epitaxial graphene. *Science*, 312:1191, 2006.

[82] P Blake, R Yang, S Morozov, and F Schedin. Influence of metal contacts and charge inhomogeneity on transport properties of graphene near the neutrality point. *Solid State Communications*, 2009.

[83] K I Bolotin, K J Sikes, M Klima, G Fudenberg, J Hone, P Kim, and H L Stormer. Ultrahigh electron mobility in suspended graphene. *Solid State Communications*, 146:351–355, 2008.

[84] Edgar Bonet, Mandar M. Deshmukh, and D. C. Ralph. Solving rate equations for electron tunneling via discrete quantum states. *Physical Review B*, 65: 045317, 2002.

[85] K M Borysenko, J T Mullen, E A Barry, S Paul, Y G Semenov, J M Zavada, M Buongiorno Nardelli, and K W Kim. First-principles analysis of electron-phonon interactions in graphene. *Physical Review B*, 81:121412(R), 2010.

[86] Simon Branchaud, Alicia Kam, Piotr Zawadzki, Francois M Peeters, and Andrew S Sachrajda. Transport detection of quantum hall fluctuations in graphene. *Physical Review B*, 81:121406(R), 2010.

[87] V Brar, Y Zhang, Y Yayon, and T Ohta. Scanning tunneling spectroscopy of inhomogeneous electronic structure in monolayer and bilayer graphene on sic. *Applied Physics Letters*, Jan 2007.

[88] J Bunch, Y Yaish, M Brink, K Bolotin, and P McEuen. Coulomb oscillations and hall effect in quasi-2d graphite quantum dots. *Nano Letters*, 5:287–290, 2005.

[89] A H Castro Neto and F Guinea. Impurity-induced spin-orbit coupling in graphene. *Physical Review Letters*, 103:026804, 2009.

[90] A H Castro Neto, F Guinea, N M R Peres, K S Novoselov, and A K Geim. The electronic properties of graphene. *Review of Modern Physics*, 81:109–162, 2009.

[91] Sungjae Cho and Michael S Fuhrer. Massless and massive particle-in-a-box states in single-and bi-layer graphene. *Nano Research*, 4:385, 2011.

[92] A Deshpande, W Bao, Z Zhao, C. N Lau, and B. J Leroy. Mapping the dirac point in gated bilayer graphene. *Applied Physics Letters*, 95(24):243502, 2009.

[93] Xu Du, Ivan Skachko, Fabian Duerr, Adina Luican, and Eva Y. Andrei. Fractional quantum hall effect and insulating phase of dirac electrons in graphene. *Nature*, 462:192–195, 2009.

[94] Tian Fang, Aniruddha Konar, Huili Xing, and Debdeep Jena. Carrier statistics and quantum capacitance of graphene sheets and ribbons. *Applied Physics Letters*, 91:092109, 2007.

[95] A. F Garcia-Flores, H Terashita, E Granado, and Y Kopelevich. Unconventional landau levels in bulk graphite revealed by raman spectroscopy. *arXiv.org*, cond-mat.mes-hall, 2008.

[96] A Geim. Graphene: Status and prospects. *Science*, 324:1530–1534, 2009.

[97] M. I. Katsnelson, K. S. Novoselov, and A. K. Geim. Chiral tunnelling and the klein paradox in graphene. *Nature Physics*, 2:620–625, 2006.

[98] P Lauffer, K Emtsev, R Graupner, and T Seyller. Atomic and electronic structure of few-layer graphene on sic (0001) studied with scanning tunneling microscopy and spectroscopy. *Physical Review B*, 2008.

[99] Xialin Li, Xinran Wang, Li Zhang, Sangwon Lee, and Hongjie Dai. Chemically derived, ultrasmooth graphene nanoribbon semiconductors. *Science*, 319:1229, 2008.

[100] Xing Lan Liu, Dorothee Hug, and Lieven M.K Vandersypen. Gate-defined graphene double quantum dot and excited state spectroscopy. *arxiv.org*, pages 1–15, 2010.

[101] Mark B Lundeberg and Joshua A Folk. Spin-resolved quantum interference in graphene. *Nature Physics*, 5(12):894–897, 2009.

[102] S Marchini, S Günther, and J Wintterlin. Scanning tunneling microscopy of graphene on ru (0001). *Physical Review B*, 2007.

[103] E Mariani, L Glazman, A Kamenev, and F von Oppen. Zero-bias anomaly in the tunneling density of states of graphene. *Physical Review B*, 2007.

[104] David L Miller, Kevin D Kubista, Gregory M Rutter, Ming Ruan, and Walt A de Heer. Structural analysis of multilayer graphene via atomic moire interferometry. *Physical Review B*, 81:125427, 2010.

[105] S Morozov, K Novoselov, and M Katsnelson. Giant intrinsic carrier mobilities in graphene and its bilayer. *Physical Review Letters*, 2008.

[106] R Nair, P Blake, and A Grigorenko. Fine structure constant defines visual transparency of graphene. *Science*, 2008.

[107] K Novoselov, A Geim, S Morozov, and D Jiang. Two-dimensional gas of massless dirac fermions in graphene. *Nature*, 438:197–200, 2005.

[108] K. S Novoselov, Z Jiang, Y Zhang, S. V Morozov, H. L Stormer, U Zeitler, J. C Maan, G. S Boebinger, P Kim, and A. K Geim. Room-temperature quantum hall effect in graphene. *Science*, 315(5817):1379, 2007.

[109] J Pereira Jr, P Vasilopoulos, and F Peeters. Tunable quantum dots in bilayer graphene. *Nano Letters*, 7:946–949, 2007.

[110] L Ponomarenko, R Yang, and T Mohiuddin. Effect of a high- environment on charge carrier mobility in graphene. *Physical Review Letters*, 2009.

[111] L Ponomarenko, F Schedin, M I Katsnelson, R Yang, E W Hill, K S Novoselov, and A K Geim. Chaotic dirac billiard in graphene quantum dots. *Science*, 320: 356–358, 2008.

[112] C Riedl, C Coletti, T Iwasaki, A Zakharov, and U Starke. Experimental techniques in condensed matter physics at low temperatures. *Physical Review Letters*, 103:246804, 2009.

[113] E Rossi, J H Bardarson, P W Brouwer, and S Das Sarma. Signatures of klein tunneling in disordered graphene p-n-p junctions. *Physical Review B*, 81:121408(R), 2010.

[114] E Sasioglu, S Caliskan, and M Kumru. Critical behavior of density of states near fermi energy in low-dimensional disordered metals. *Physical Review B*, 79: 035123, 2009.

[115] N Stander, B Huard, and D Goldhaber-Gordon. Evidence for klein tunneling in graphene pn junctions. *Physical Review Letters*, 2009.

[116] L Tapaszto, G Dobrik, P Nemes-Incze, G Vertesy, Ph Lambin, and L Biro. Tuning the electronic structure of graphene by ion irradiation. *Physical Review B*, 78:233408, 2008.

[117] M Titov. Impurity-assisted tunneling in graphene. *European Physics Letters*, 79:17004, 2007.

[118] Frank Tseng and Avik W Ghosh. From low-bias to high-bias current saturation: fundamental trade-offs in graphene based transistors. *arxiv.org*, pages 1–12, 2010.

[119] L. Vitali, M. A. Schneider, K. Kern, L. Wirtz, and A. Rubio. Phonon and plasmon excitation in inelastic electron tunneling spectroscopy of graphite. *Physical Review B*, 69:121414, 2004.

[120] W Wang, W Han, K Pi, and K McCreary. Growth of atomically smooth mgo films on graphene by molecular beam epitaxy. *Applied Physics Letters*, 2008.

[121] T Wehling, K Novoselov, and S Morozov. Molecular doping of graphene. *Nano Letters*, 8:173–177, 2008.

[122] M Wimmer, A R Akhmerov, and F Guinea. Robustness of edge states in graphene quantum dots. *Physical Review B*, 82:045409, 2010.

[123] E. L. Wolf. *Principles of Electron Tunneling Spectroscopy*. Oxford University Press, 1985. ISBN 0-19-503417-1.

[124] A. F. Young and P. Kim. Quantum interference and klein tunnelling in graphene heterojunctions. *Nature Physics*, 5:222–226, 2009.

[125] Yuanbo Zhang, Yan-Wen Tan, Hort L Stormer, and Philip Kim. Experimental observation of the quantum hall effect and berry's phase in graphene. *Nature*, 438:201–204, 2005.

[126] Y Zhang, J Small, M Amori, and P Kim. Electric field modulation of galvanomagnetic properties of mesoscopic graphite. *Physical Review Letters*, 2005.

[127] Y Zhang, Y Tan, H Stormer, and P Kim. Experimental observation of the quantum hall effect and berry's phase in graphene. *Nature*, 2005.

[128] Y Zhang, Z. Jiang, J. P. Small, M. S. Purewal, Y. W. Tan, M. Fazlollahi, J. D. Chudow, J. A. Jaszczak, H. L. Stormer, and P. Kim. Landau-level splitting in graphene in high magnetic fields. *Physical Review Letters*, 96:136806, 2006.

[129] Y Zhao, P Cadden-Zimansky, Z Jiang, and P Kim. Symmetry breaking in the zero-energy landau level in bilayer graphene. *Physical Review Letters*, 104: 066801, 2010.

[130] Yisong Zheng and Tsuneya Ando. Hall conductivity of a two-dimensional graphite system. *Physical Review B*, 65(24):11, 2002.

[131] S.Y Zhou, G.H Gweon, and A Lanzara. Low energy excitations in graphite: The role of dimensionality and lattice defects. *Annals of Physics*, 321:1730–1746, 2006.

[132] J. M. Ziman. *Principles of the Theory of Solids*. Cambridge University Press, 1972.

VITA

Chris Malec was born in Madison, WI. A couple years later he was whisked away to Rochester, MN, where thus far he has spent the majority of his years on this earth. From Minnesota, he learned about being cold and polite. After failing to block the election of a pro-wrestler to the govenorship, he realized it was time for a change and took a whole bunch of classes at UW-Madison, receiving his B.S. in physics. He spent a year in Atlanta, working as a Mr. Wizard for hire at Mad Science of Atlanta, now defunct. Somewhere in there, he convinced Sara Childs to upgrade to Sara Malec, an event that dwarfs those presented in this document in importance. Georgia Tech took him in, he took a bunch more classes, and sequestered himself together with the comforting (maddening) drone of the cryopump for many years, at the end of which, five people came together to test his mettle. His story after this is unknown, though the existence of this document proves his victory against the five.